^{129}Xe NMR for Investigations of Complex and Dynamic Systems

Dissertation
zur Erlangung des Grades
Doktor der Naturwissenschaften
im Promotionsfach Chemie

am Fachbereich Chemie, Pharmazie und Geowissenschaften
der Johannes Gutenberg-Universität in Mainz

Mathis Düwel

geboren in Braunschweig

Mainz, 2012

Die vorliegende Arbeit wurde in der Zeit von Oktober 2008 bis April 2012 am Max-Planck-Institut für Polymerforschung in Mainz angefertigt.

Dekan:
1. Berichterstatter:
2. Berichterstatter:

Tag der mündlichen Prüfung: 15. Juni 2012

Contents

1 Introduction

Since the discovery of xenon by Ramsay and Travers in 1898 during their study of liquified air, the noble gas has found a wide range of applications, e.g. in illumination devices, as an anesthetic in medicine, as a propellant in space craft thrusters, and in many scientific studies. Starting in the second half of the 20$^{\text{th}}$, the application of xenon, namely its isotope ^{129}Xe, in the field of NMR, discovered 1946 by Bloch and Purcell [Blo46, Pur46], began. In the last 65 years, new NMR methods like magnetic resonance imaging (MRI) (developed by Lauterbur and Mansfield [Lau73, Gar74, Man77]) and the application of NMR spectroscopy to a multitude of questions arising in chemistry, physics, and medicine, e.g. molecular structure analysis, characterization of materials, diffusion measurements, qualification and quantification of inter- and intramolecular interactions, and more, lead to a large presence of NMR methods in science and technology.
The use of ^{129}Xe in NMR spectroscopy and MRI is mostly based on two advantageous properties: First, Xe atoms are very sensitive to their (physical) environment due to their large and polarizable electronic shell, which turns them together with their chemical inertness into an ideal 'NMR probe' which can be introduced into many systems. The sensitivity of ^{129}Xe is reflected in the wide range of the chemical shift and its changes according to changes in the observed systems. The second advantageous property of ^{129}Xe is the ability of being 'hyperpolarized', giving rise to large signal enhancements in NMR experiments [Aim08], which suffer in general from a very low signal-to-noise ratio (SNR) due to the low spin polarization or low abundance of the spin. The hyperpolarization method used here is the spin-exchange optical pumping (SEOP) process [Kas50, Bou60, Wal97]. Hyperpolarization of ^{129}Xe with its large signal enhancements then enables very fast NMR measurements.
The sensitivity of ^{129}Xe in NMR experiments coupled with very short measurement times due to the hyperpolarization gives access to the monitoring and characterization of a large range of systems. In the current work, applications of ^{129}Xe NMR spectroscopy to several systems differing in complexity are presented. Figure 1.1 gives an overview over the characteristics of the systems for which ^{129}Xe NMR is able to gather information. These include static and dynamic systems, aqueous phases, and (nano)porous materials. Using the large signal enhancement of hyperpolarization of ^{129}Xe, time-resolved measurements are possible.
In medicine, hyperpolarized gases, namely ^{3}He and ^{129}Xe, are used for MR imaging of the lung [Alb94]. The lung constitutes a gas-filled hollow space where the density of protons, i.e. the normally used nucleus for MRI, is very low. Using hyperpolarized gases can result in MR images with very high signal and good contrast [Mee08, Hor09, Riz11a].

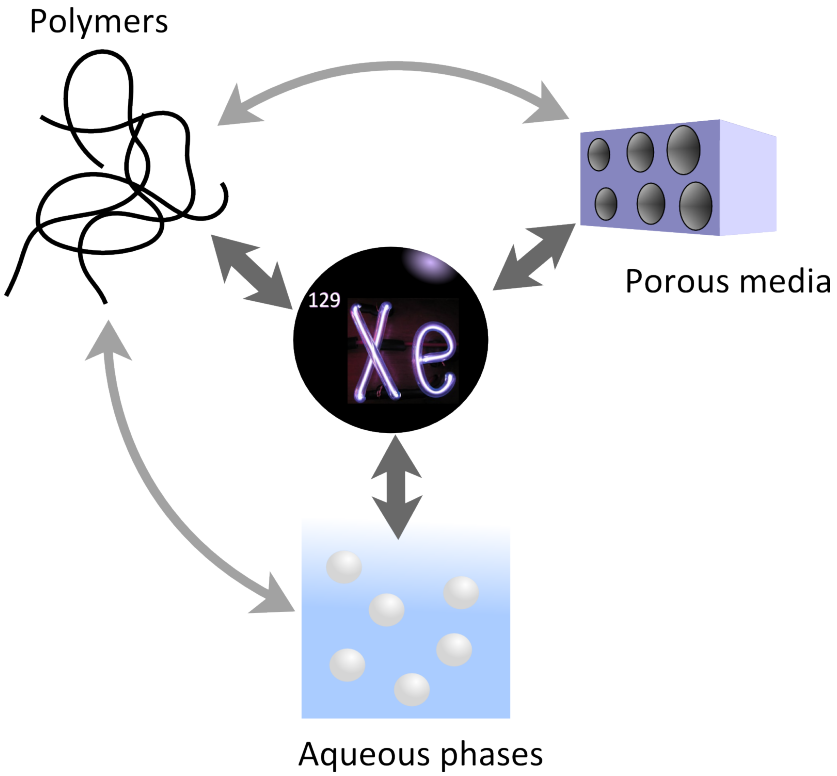

Figure 1.1: ^{129}Xe is a very versatile NMR probe, able to gather information from its enviroment in a multitude of different systems. Its application in this work includes static and dynamic systems, aqueous phases, nanoporous polymer systems, and more.

For a practical and reliable use of hyperpolarized ^{129}Xe in MRI, the hyperpolarized Xe gas from the polarizer is accumulated as ice, stored, and transported to the imaging facility. In Chapter 4 of this thesis, results which advance the use of hyperpolarized ^{129}Xe in medical applications are presented. Substantial improvements in the accumulation process and the storage of the hyperpolarized gas are accomplished in this work, allowing for a larger part of the polarization of ^{129}Xe to be used after accumulation and storage. The most important parameter for MR images is the contrast which allows for the recognition and distinction of areas of interest. When using hyperpolarized gases, the diffusion of the gas changes the image contrast, which has been shown for hyperpolarized ^{3}He [AP09]. While ^{129}Xe possesses a much slower diffusion than ^{3}He, it is shown here that the admixture of a faster diffusing buffer gas influences the contrast of ^{129}Xe MR images.
In Chapter 5 of this thesis, highly anisotropic, nanoporous polymer films were studied by ^{129}Xe NMR spectroscopy. The method proves to be a valuable tool to characterize the unique orientational features of the cavities inside the polymer films. Results concerning

the chemical shift dependence of ^{129}Xe on the macroscopic orientation of the polymer film and the sample temperature are presented.
Chapter 6 of this thesis introduces a new method for the online monitoring of (polymerization) reactions by ^{129}Xe NMR spectroscopy. Using a continuous flow of hyperpolarized ^{129}Xe gas into the reaction mixture, the chemical shift of the dissolved ^{129}Xe is used in order to give time-resolved information about the reaction conversion [Due12, Aco12]. Results for the online monitoring of two miniemulsion polymerization reactions are presented. The validity of the new method is checked by comparison with a known monitoring technique, i.e. calorimetry, and by an extensive charaterization of the polymerization products.

2 Theory

2.1 Nuclear Magnetic Resonance

Nuclear magnetic resonance (NMR) is based on a quantum mechanical property of some atomic nuclei, the so-called nuclear spin. The nuclear spin originates from the angular momentum of the elementary particles of the atomic nucleus, namely protons and neutrons. The angular momentum of these nucleons is not created by rotation of the particles, but is an intrinsic property of the particles like mass or electric charge. Depending on the number of protons and neutrons, the atomic nucleus can have a spin $I = 0$ (only even numbers of protons and neutrons) or a non-zero spin (half-integral or integral). The nuclei with non-zero spins can be used in NMR experiments. A spin $\neq 0$ entails a magnetic moment, too. A nucleus with the spin I has the following magnetic momentum μ

$$\mu = \gamma \hbar I \tag{2.1}$$

with $\hbar = h/2\pi$ the reduced Planck's constant and γ the magnetogyric ratio which is a characteristic property of each isotope. The component of the magnetic momentum parallel to an axis (normally chosen as the z-axis and parallel to an external magnetic field as used in NMR) is proportional to the component of the angular momentum parallel to this axis:

$$\mu_z = \gamma \hbar m_I \tag{2.2}$$

with $m_\mathrm{I} = I, I-1, ..., -I$ the magnetic quantum number. When placed in an external magnetic field (as done in an NMR experiment), the magnetic moment of the nuclei interact with the external field. The energy of the interaction depends on the angle between the nuclear magnetic moment and the external field and is lowest when the magnetic moment is aligned parallel and highest when aligned anti-parallel to the external field. Most nuclei used in NMR are nuclei with $I = \frac{1}{2}$, for example ^{1}H, ^{13}C, and also the nucleus used in this work, ^{129}Xe. The number of distinct orientations of the spin and therefore energy levels is $2I + 1$. The energy levels E for an external magnetic field parallel to the z-axis with the magnetic field strength B_0 are then given by

$$E_{m_I} = -\gamma \hbar B_0 m_0. \tag{2.3}$$

For a spin $I = \frac{1}{2}$, there exist two energy levels with an energy difference of

$$\Delta E = \gamma \hbar B_0. \tag{2.4}$$

2.1.1 Polarization

The energy difference is correlated to the stength of the external magnetic field B_0 and the magnetogyric ratio of the actual nucleus. In the classical view, the macroscopic sum of all magnetic moments, called (bulk or net) magnetization M, is used to describe simple NMR experiments. The thermal equilibrium net magnetization M_0 for a spin $I = \frac{1}{2}$ system can be calculated by considering the populations of the two energy levels. The energy levels are occupied according to a Boltzmann distribution. Thus, the populations N_+ and N_- can be calculated by the following equation:

$$\frac{N_+}{N_-} = e^{\frac{\Delta E}{k_B T}} = e^{\frac{-\gamma \hbar B_0}{k_B T}} \tag{2.5}$$

with N_+ and N_- the number of spins in the upper and lower state, respectively, ΔE the energy difference between the two spin states, k_B the Boltzmann constant, and T the temperature of the sample (see 2.1).

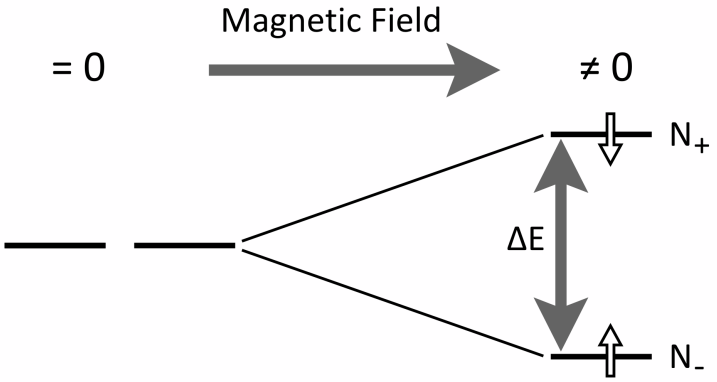

Figure 2.1: The different energy niveaus of a Spin $I = 1/2$ system like ^{1}H or ^{129}Xe. The energy difference ΔE depends on the strength of the magnetic field.

The population excess of one enery level, or polarization P, is proportional to the amplitude of the NMR signal. It can be expressed by the following equation:

$$[H]P = \frac{N_+ - N_-}{N_+ + N_-} = \frac{1 - e^{\frac{\Delta E}{k_B T}}}{1 + e^{\frac{\Delta E}{k_B T}}} = \frac{1 - e^{\frac{-\gamma \hbar B_0}{k_B T}}}{1 + e^{\frac{-\gamma \hbar B_0}{k_B T}}}. \tag{2.6}$$

Using $k_B T \gg \gamma\hbar B_0$ as a high temperature approximation, the polarization P can be calculated by

$$P = tanh\left(\frac{\gamma\hbar B_0}{2k_B T}\right) \approx \frac{\gamma\hbar B_0}{2k_B T}. \tag{2.7}$$

Because of the small energy difference between the two spin states, only a very small population difference is established. The most commonly used nucleus, ^{1}H, has the largest magnetogyric ratio and thus the largest thermal equilibration polarization at a given magnetic field strength.
However, the polarization of protons ^{1}H at 295 K in a magnetic field with the field strength of 7 T is only $1.6 \cdot 10^{-5}$. For other nuclei like ^{129}Xe ($P = 4.5 \cdot 10^{-6}$) or ^{13}C ($P = 4.1 \cdot 10^{-6}$), the polarization is even smaller due to the smaller magnetogyric ratios. Additionally, the natural abundance of the NMR active isotope is generally smaller than 100 % with the exception of the proton ^{1}H, which has a natural abundance of over 99.99 %.
The problem of the small polarization and thus the low sensitivity of NMR can be overcome by so-called hyperpolarization methods which will be presented in Section 2.3.

2.1.2 Chemical Shift

As denoted in Equation 2.4, there is an energy difference between the two (for a spin $I = \frac{1}{2}$ system) energetic states of a spin. This energy difference can of course be expressed as a frequency of a (electromagnetic) radiation:

$$\Delta E = \gamma\hbar B_0 = h \cdot \nu_L \tag{2.8}$$

with ν_L being the resonance frequeny of the the system, the so-called *Larmor frequency*. If the spin system is irridiated with electromagnetic radiation of the Larmor frequency, a strong interaction between the spins and the radiation is observable (=*resonance* condition). The Larmor frequencies are different for different nuclei at the same magnetic field strength due to the different magnetogyric ratios of the nuclei. The resonance frequencies depend also on the magnetic field strength. They correspond to the range of *radio frequency (RF)*, however, for the currently strongest NMR magnets, they go up to approximately 1 GHz for ^{1}H.
In a macroscopic sample, the spins do not solely feel the strength of the external magnetic field B_0, but are experiencing a local magnetic field strength B_{loc} (generally $B_{loc} \neq B_0$). Due to movements of the electrons surrounding the nucleus in the external magnetic field, an additional *induced* magnetic field is created, which influences the nuclear spins. This induced magnetic field, B_i, is generally much weaker than the external magnetic field. The actual, local field B_{loc} which is experienced by a nucleus is normally expressed

as:

$$B_{loc} = B_0 + B_i = B_0\,(1 - \sigma) \tag{2.9}$$

with the shielding constant σ which depends on the environment of the observed spin (electronic and molecular configuration and conformation, but sometimes also the physical environment).
The Larmor frequency of a localized spin can be expressed as following:

$$\nu_L = B_{loc} \cdot \frac{\gamma}{2\pi} = (1 - \sigma)\,\frac{\gamma B_0}{2\pi}. \tag{2.10}$$

The differences in the resonance frequency between different spins (e.g. in a molecule) is normally given using the so-called *chemical shift* δ in relation with a reference resonance frequency ν_0 expressed in [ppm]:

$$\delta = \frac{\nu - \nu_0}{\nu_0} \cdot 10^6. \tag{2.11}$$

In principal, the reference resonance frequency, ν_0, is chosen arbitrarily. For ^{1}H NMR in solution, tetramethylsilane (TMS) is often used, whereas for ^{129}Xe NMR, the chemical shift of the free gas (at zero density) is chosen as the reference.

Chemical Shift Anisotropy

Equation 2.11 gives an isotropic chemical shift value for the spin, which is independent of the spatial orientation. This holds true for many NMR experiments, mainly in gas and solution, where the molecule or atom containing the observed spin can move and rotate principally free in the time range of the NMR experiment (or no anisotropic surroundings to the spin are present). However, if the localenvironment of the spin is not isotropic and the nucleus is (partially) fixed, the magnitude of the chemical shift can vary with respect to the orientation of the molecule (or atom). The orientation dependence of the chemical shift is called chemical shift anisotropy (CSA). The chemical shift can be expressed formally as a second rank tensor. Choosing a suitable coordinate frame, the chemical shift tensor can be expressed by the three main components (the diagonal elements of the matrix of the chemical shift tensor) and the (eigen)vectors describing the used coordinate frame.

2.1.3 Relaxation

After pertubation of the magnetization of a sample, the system will return to the state of equilibration by two processes, one related to the alignment of the magnetization in the magnetic field, and one related to the coherence of the rotating spins in the (rotating) x-y-plane. Both processes are independent from each other and occur simultaneously.

Longitudinal or Spin-Lattice Relaxation

Assuming a simple excitation of the spins by a $\pi/2$ pulse, which moves the net magnetization M_0 into the x-y-plane (the longitudinal component M_z along the z-axis becomes zero), the spin ensemble will return back to its equilibrium state with time, causing the longitudinal component of the net magnetization to recover to its equilibrium value M_0 (and the NMR signal in the x-y-plane to diminish). This relaxation process is caused by the exchange of energy between the spin ensemble and its surrounding enviroment (often called 'lattice', hence the name of this relaxation process). The rate of relaxation can be described by the charateristic time T_1 as follows:

$$\frac{dM_z}{dt} = \frac{M_z - M_0}{T_1} \tag{2.12}$$

and the following solution:

$$M_0(t) = M_0 \cdot \left(1 - e^{\frac{-t}{T_1}}\right). \tag{2.13}$$

For thermally polarized samples, the longitudinal relaxation rate determines a minimal repetition time for an experiment, because the magnetization has to return to its equilibrium before the experiment can be faithfully repeated. A repetition time of approximately $5{\cdot}\mathrm{T}_1$ is generally chosen to ensure the magnetization recovery. Regarding hyperpolarized samples (see Section 2.3), the longitudinal magnetization exceeds the thermal one, sometimes by orders of magnitude. Nevertheless, the return to the thermal equilibrium is still characterized by the relaxation time T_1. However, the process can no longer be described as a recovery of the magnetization, but as a decay to the value of the magnetization to the thermal equilibrium:

$$M_z(t) = M(t=0) \cdot e^{\frac{-t}{T_1}} + M_0. \tag{2.14}$$

The T_1 times of hyperpolarized samples are not measured by the normally used method of 'inversion recovery' which includes a full 180 ° flip of the net magnetization, but by subsequent scans over time with a small flip angle (often between 1-5 °) (see Section 2.3 for such experiments). The main contributions of this relaxation mechanism for hyperpolarized gases are described and characterized in Section 2.5.

Transversal Relaxation

The tranversal relaxation describes a process which takes places after the net magnetizations has been moved into the x-y-plane: Initially, the excited spins possess phase coherence, but dephase with time due to internuclear interactions (dipole-dipole, chemical shift, or similar interactions) and inhomogeneities of the external magnetic field. The relaxation rate due to the pure spin-spin interactions is charaterized by the relaxation

time T_2 which can be described similar to the longitudinal relaxation:

$$\frac{dM_{xy}}{dt} = \frac{-M_{xy}}{T_2} \tag{2.15}$$

and

$$M_{xy}(t) = M_{xy}(t=0) \cdot e^{\frac{-t}{T_2}} \tag{2.16}$$

Inhomogeneities of the external magnetic field and local susceptibilty differences in the sample cause an increase in the T_2 relaxation rate, which lead to a shortened transversal time T_2^*. Often, the static contributions due to inhomogeneities can be compensated in NMR or MRI experiments by the use of certain RF pulse sequences (in a very simple case, an echo sequence with a 180 ° RF pulse). The relaxation rate characterized by T_2 can be very short (e.g. in solids) and cannot be influenced for a given sample at given conditions.

2.2 Properties of xenon and ^{129}Xe NMR

Xenon is a color- and odorless noble gas with the atomic number 54 with five filled electron shells (electronic configuration [Kr] $4d^{10}5s^25p^6$). It was discovered 1898 by Lord Ramsey together with Morris Travers. There are 9 stable isotopes and over 40 unstable radioactive isotopes. At a pressure of 1 bar, xenon boils at a temperature of 165.0 K and melts at 161.4 K. The relative high melting point is caused by van-der-Waals interactions between the xenon atoms. It allows for accumulation of Xe ice and storage of xenon at the temperature of liquid N_2 (77 K).
For the field of NMR, only the two isotopes ^{129}Xe and ^{131}Xe are of interest due to their spin $I \neq 0$. ^{129}Xe has nuclear spin $I = \frac{1}{2}$ and ^{131}Xe nuclear spin $I = \frac{3}{2}$. In this work, only the isotope ^{129}Xe has been used for NMR experiments. In Table 2.1, the NMR properties of ^{129}Xe are compared with those of ^{1}H.
Xenon is very rare on earth, it is 10,000 to 100,000-fold less abundant compared to the lighter noble gases.[1] In 2008, approximately $12 \cdot 10^6$ liters of xenon have been extracted from the earth atmosphere. The natural abundance of ^{129}Xe is only 26.44 %, that means, if natural xenon gas is used, only every fourth nucleus will be useful in ^{129}Xe NMR measurements. Isotopic enrichment up to >90 % is possible, but expensive. The isotopic enrichment can be necessary in the case of very low solulibility or adsorption of xenon in the sample material in order to reduce the measurement time in NMR experiments.
Although a number of chemical reaction products containing xenon are known (generally the products of the reaction of a strong oxidating agent with xenon, e.g. the first known compund of a noble gas, xenon hexafluoroplatinate [Bar62]), xenon as a noble gas is very unreactive and chemically inert, also non-toxic. Commercially, xenon gas is often used in gas discharge lamps (used in movie theatre projectors and, increasingly, in automotive applications). Xenon is soluble to a certain amount in many liquids, in non-polar like organic solvents as well as in aqueous solutions and emulsions.[2] Xenon atoms can be also adsorped into many porous materials like polymers or porous crystalline compounds like zeolites or metal-organic frameworks.
Due to its large electron cloud and therefore large polarizability (larger than that of chlorine and 20 times larger than that of helium), the chemical shift of xenon is very sensitive to its chemical and physical environment. The large polarizability leads to a large chemical shift range for ^{129}Xe which can extend to several thousands of ppm for xenon compounds like XeO_6^+ or XeF_6. In this work, no covalently bound xenon has

1 It is assumed that xenon can be a substitute for silicon in quartz minerals at very high pressures and temperatures and that a large amount of the xenon on earth is bound in the continental crust [Dmo09].

2 For example, xenon is used as an environmentally friendly, very compliant medical inhalant anaesthetic. It works, similar to nitrous oxide, by blocking the NMDA receptor [Ber09]. Due to its inertness and limited solulibilty in water or blood, it does not bind to any molecules in the human body and is very quickly eliminated after stopping the anaesthetic administration.

been used, but only dissolved or adsorped xenon. Thus the chemical shift range of ^{129}Xe observed here reaches from 0 ppm (for the free gas at pressure $p = 0$) to approximately 250 ppm (for xenon atoms adsorped in polystyrene films). The chemical shift of the free xenon gas is often used as a (internal) reference and is generally set to 0 ppm at the pressure $p = 0$.
Due to all described properties, xenon can be used as an excellent atomic NMR probe for many applications and materials. In material sciences, many applications can be found for ^{129}Xe NMR studying porous materials (see section 2.7 for examples in the literature). However, ^{129}Xe is also used in experiments in biology [Che03], for example to investigate proteins in solution [Loc01], protein-protein interactions [Pon08] or biosensors [Ber08], and in medicine, particularly for MRI of the lungs and the assessment of respiratorial diseases (see for example [Kau00, Pat07, Wak08, Dri11]). Many applications, especially in medicine, take advantage of the possibility of hyperpolarization of ^{129}Xe to drastically enhance the NMR signal. In the next section, the technique used to achieve this hyperpolarization is described.

	^{1}H	^{129}Xe
Spin I	1/2	1/2
Magnetogyric ratio γ		
[MHz/T]	42.58	11.84
[$s^{-1}T^{-1}$]	$2.675 \cdot 10^{-8}$	$-0.74 \cdot 10^{-8}$
Natural abundance [%]	>99.99	26.44
Relative receptivity	1.00	$5.72 \cdot 10^{-3}$

Table 2.1: NMR properties of ^{129}Xe in comparison with ^{1}H

2.3 Hyperpolarization

NMR is one of the most powerful tools to analyze the structure and dynamic behavior of molecules in solution or solid state. However, its major drawback is the inherent low sensitivity due to the low spin polarization at ambient temperatures (see section 2.1). Equation 2.6 suggests a number of different ways to increase the population difference in thermal equilibrium and hence the NMR sensitivity: First, a decrease in temperature, or second, an increase of the strength of the magnetic field. In practice, both methods are very limited: The decrease of temperature may probably be problematic due to the sample behavior (e.g. phase transitions like freezing of liquids) or the sample stability. Increasing of the strength of the magnetic field is limited due to technical and economic reasons: The development and construction of the always stronger superconducting magnets is relatively slow and very expensive (compare with Figure 2.2).

As a consequence, in recent years many efforts have been devoted to the development of the so-called hyperpolarization methods. These methods aim to create a large polarization of the spins far beyond the thermal equilibrium (Fig. 2.3) and thus, a large enhancement of the NMR signal. Enhancements of the NMR signal in the range of five orders of magnitude compared to the thermal signal are achievable [Rut99, Rus06, AL03, Aim08].

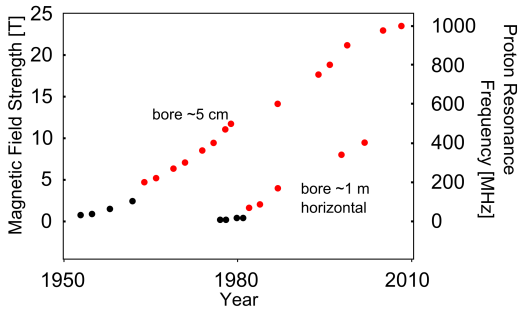

Figure 2.2: The increasing magnetic field strength of commercially available NMR magnets (left curve) with small bores and MRI (scanner) magnets with larger bores (black dots represent iron core, red dots the much stronger superconducting magnets). Adapted from [Roo07].

One of the main advantages of hyperpolarization methods is the independence from the strength of the magnetic field (and from the sample temperature). Hence, experiments with hyperpolarized samples can be performed at standard or ambient conditions, providing the possibility of experiments on sensitive materials or living tissue. However, the hyperpolarization of a sample cannot be kept up for an infinite time. Even without any measurement, the hyperpolarization irreversibly diminishes with time due to the spin-lattice relaxation (T_1 relaxation). The sample returns to the equilibrium state. Additionally, each measurement consumes hyperpolarization. In a normal NMR experiment, the thermal polarization of the sample is recovered with a rate governed by its T_1 relaxation rate. For hyperpolarization NMR experiments, if repeated measurements are necessary, a way to reconstitute the hyperpolarization in the sample must exist. The reconstitution of the hyperpolarization can be in-situ (e.g. for dynamic nuclear polarization (DNP), see below) or the hyperpolarization can be supplied from the outside (e.g. the continuous in-flow of a

hyperpolarized substance into the sample). Several so-called hyperpolarization methods can overcome the lack of sensitivity of NMR spectroscopy, e.g. allowing for an excellent time resolution in dynamic measurements.

Brute Force Approach

The most straightforward method is the so-called *brute force* approach which is very similar to the traditional methods of increasing the polarization, but is nevertheless counted as a hyperpolarization method [Aim08, Ros10]: Prior to any measurement, the sample is kept at very low temperatures and at very high magnetic field, allowing for the build-up of the corresponding thermal equilibrium. After removal of the sample from the high magnetic field, the priorly created polarization decays relatively fast (depending on the relaxation of the sample). After quick insertion into another, weaker magnetic field, the measurement can take place [Krj05]. A drawback of this method are the very long build-up times of the polarization due to the very long T_1 times at low temperatures.

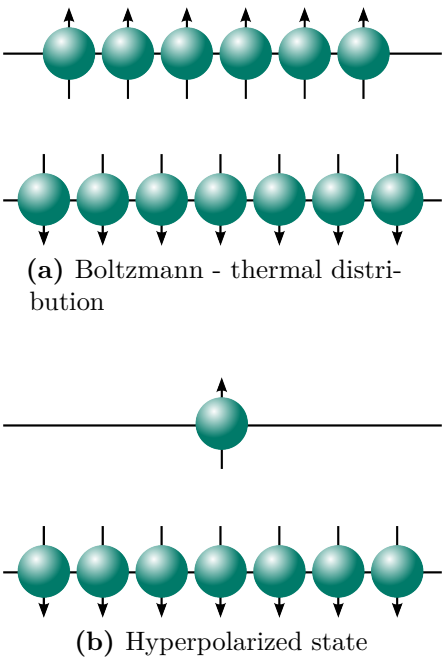

(a) Boltzmann - thermal distribution

(b) Hyperpolarized state

Figure 2.3: Thermal equilibrated (a) and hyperpolarized (b) state for a spin 1/2 system in an external magnetic field.

Dynamic Nuclear Polarization

Another hyperpolarization technique is DNP which consists of the transfer of polarization from highly polarized, unpaired electrons to nuclear spins, mostly to protons of solvent molecules in the vicinity of the electron [Car56]. Due to their high magnetogyric ratio, electrons are polarized to a much higher degree than nuclear spins at the same temperature and magnetic field strength. The polarization transfer takes place during irridiation with microwaves near ot at the electronic paramagnetic resonance (EPR) frequency of the electrons. Because most samples do not contain unpaired electrons, a doping of the sample with radicals is necessary (often nitroxide- or triaryl-radicals are used). The DNP process takes place either in solid state on a time scale of 30 to 60 min prior to the measurement, or in the liquid state, resulting in a much faster rise of the polarization at the cost of a lower attainable polarization. The hyperpolarization in solid state involves the heating of the frozen sample, and its dilution and shuttling into the NMR magnet

prior to the measurement, but has found many applications in material sciences and medicine [AL03, Row10, Bow11].
A disadvantage of DNP is the presence of radicals in the sample which are often toxic. The toxic radicals limit the applicabilty of the method to biological matter. Methods for the removal of the radicals prior to the measurement are subject of current research.

Para-hydrogen induced Polarization

A third hyperpolarization strategy is the use of para-hydrogen, a spin isomer of gaseous hydrogen, applying a technique called parahydrogen induced polarization (PHIP) [Bow87, Mün11]. Hydrogen gas at room temperature has three spin configurations which are degenerate and form the ortho-hydrogen isomer (75 % at room temperature), whereas the fourth spin configuration is the para-hydrogen (25 % at room temperature). Para-hydrogen can be enriched at low temperatures by means of a paramagnetic catalyst and can be subsequently stored for days in this spin configuration. In order to generate the hyperpolarized substance, the para-hydrogen is inserted into the molecule of interest via a chemical reaction, e.g. a hydrogenation of a double or triple bond. Thus, the proton spin polarization can be transferred to the molecule. The chemical insertion of the para-hydrogen requires a catalyst matching the desired reaction and the substrate, which can be hard or even impossible to synthesize. In general, PHIP is only suitable for unsaturated compounds which can be hydrogenated with parahydrogen and thus limits the general applicability of this method. Recently, there have been developments of a techique to transfer the proton polarization to the substrate without the need to covalently attach the protons to the substrate [Atk09] and to store the polarization of the substrate for times exceeding the actual T_1 time of the substrate, using so-called singlet states [War09, Pil09].

Optical Pumping of Noble Gases

Finally, noble gases (like ^{3}He, ^{129}Xe, and recently ^{83}Kr) can be hyperpolarized by methods involving the technique of optical pumping, either of alkali metal vapour (SEOP) or, in the case of ^{3}He, of a plasma of the noble gas (metastability exchange optical pumping (MEOP)). In this work, ^{129}Xe was hyperpolarized by the technique of SEOP, which will be explained in detail in the following section.

2.4 Spin-exchange optical pumping

During the process of SEOP, angular momentum is transferred from circular polarized laser light to the spins of valence electrons of alkali metals (here: rubidium) and subsequently to the spins of nuclei of noble gases (here: ^{129}Xe) by the hyperfine interaction between the Rb electrons and the gas nuclei (see Fig. 2.4).

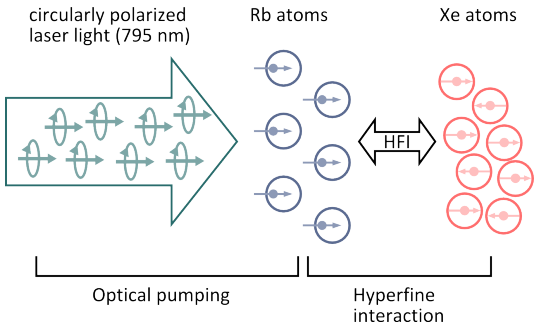

Figure 2.4: Schematic overview of SEOP. The polarization is transferred from the incident laser beam to the electrons of the Rb atoms and, subsequently, to the nuclei of the ^{129}Xe atoms.

The polarization process is comprised of two distinct steps, the optical pumping (OP) and the spin-exchange. The OP process was discovered by A. Kastler in 1950 [Kas50], which earned him the noble prize in 1966. The OP of alkali metal vapours has been described by W. B. Hawkins in 1953 ([Haw53], see also [Hap72]). The next step in the polarization process, the transfer of polarization via spin-exchange from electrons to the spins of nuclei, has been discovered by M. A. Bouchiat in 1960 [Bou60, Bou69] and further explored and theoretically explained by W. Happer et al. [Bha82, Hap84].
In the following sections, these two steps and their prerequisites will be explained briefly. More details on the SEOP process as a whole and its theory can be found in [Wal97, App98].

2.4.1 Optical pumping

The first step of the polarization process, the optical pumping, consists of the polarization of the valence electrons of vaporous alkali metals by the resonant absorption of polarized laser light. Figure 2.5 shows a very simple setup required for the optical pumping process. It consists of the optical pumping cell in an oven (to allow for the vaporous Rb atmosphere), an optical setup (laser, polarizing beam splitter cube, mirror, and lenses (not shown in Fig. 2.5)), and coils for the generation of a homogeneous magnetic field. In most ^{129}Xe polarizer setups, rubidum is used as the alkali metal due to its high vapour pressure (melting temperatue of Rb (pure metal) 39 °C at ambient pressure), its absorption of light by its D_1 transition line at a convenient wavelength of 794.7 nm and its relative simply handling. Other alkali metals, like potassium, and alkali metal mixtures have also been used [Che07].
The optical pumping cell contains the vaporous rubidium and a gas mixture containing a small fraction of ^{129}Xe (or another noble gas to be polarized) and buffer gases (normally

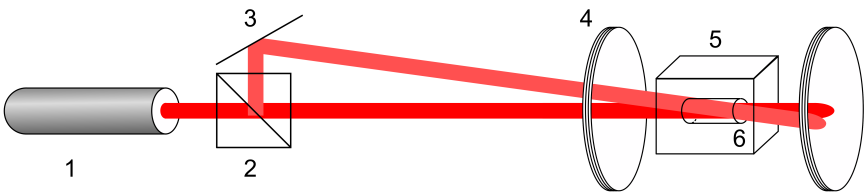

Figure 2.5: Overview of a simple setup for optical pumping consisting of laser (1), polarizing beam splitter cube (2), mirror (3), coils to create a homogeneous magnetic holding field (4), oven (5), pumping cell (6) containing the ^{129}Xe-N_2-He gas mixture and the Rb vapour. Both parts of the beam after the beam splitter cube are directed into the pumping cell.

N_2 and ^{4}He).

Rubidium has the atomic number $Z = 37$ and is found normally in two isotopes, ^{85}Rb (natural abundance 72.2 %) and ^{87}Rb (natural abundance 27.8 %). The electronic structure can be given as $1s\,2s\,2p\,3s\,3p\,3d\,4s\,4p\,5s$ with the energy level of the $5s$ orbital below these of the $4d$ and $4f$ orbitals. Thus, the Rb atom posesses a single electron in

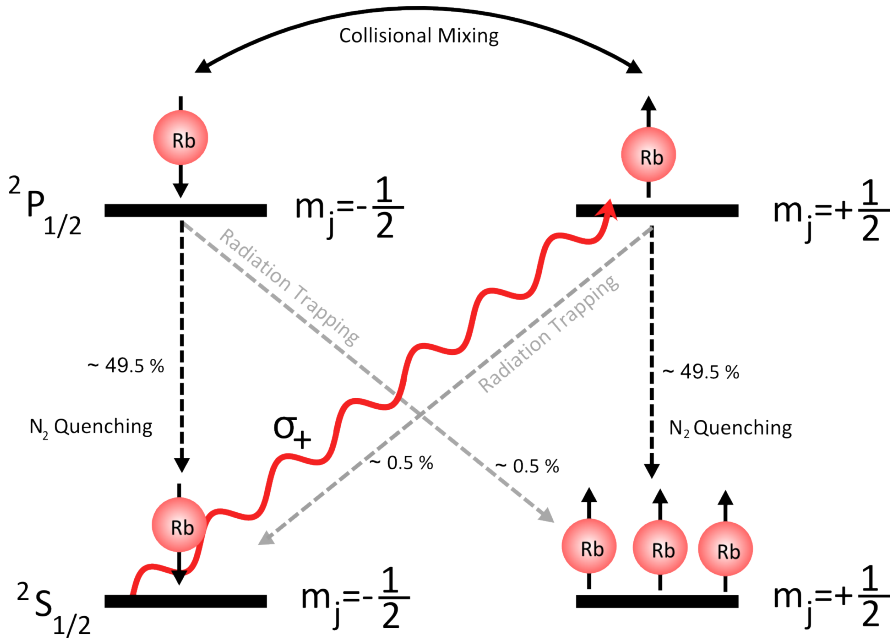

Figure 2.6: Simplified term scheme for the optical pumping process of rubidium

its valence orbital shell. The ground state is $5^2S_{1/2}$ and the first excited states are $5^2P_{1/2}$ and $5^2P_{3/2}$. The electronic energy levels of the Rb valence electron in the presence of a magnetic field field split into $(2J+1)$ Zeeman levels with their corresponding magnetic quantum numbers

$$m_J = -J,(-J+1)\ ,...,\ J. \tag{2.17}$$

The magnetic quantum number of the total angular momentum of the electron is calculated by

$$J = S + L \tag{2.18}$$

with $S = 1/2$ for the electron, and $L = 0$ for the ground s state and $L = 1$ for the excited p states. There are two possible transitions from the ground state, the first to the $5^2P_{1/2}$ state with the D_1 line at 794.7 nm and the second to the $5^2P_{3/2}$ with the D_2 line at 780.0 nm. For the wavelength of the D_1 line, intense and attainable light sources exist, e.g. dye lasers as used here.
Figure 2.6 shows a electronic energy term scheme of the valence electrons during the optical pumping process of rubidium. The polarized state to be reached is the $5^2S_{1/2}$ state with $m_J = -1/2$ (right lower corner of the term scheme).
The term scheme is simplified and does not take into account the spin of the nucleus of the Rb atom. This simplification is generally acceptable for an equilibrium pumping state of the Rb, at the elevated pressures used here, and without intense depolarization sources (like the cell walls) for the Rb. The additional spin of the Rb nucleus slows the pumping process down but does not change the principal process as described here.
The selection rule for the resonant excitation of the Rb electrons by the incident laser light is $\Delta m = \pm 1$. The incident laser light has a circular polarization σ^+ and a positive helicity, meaning $\Delta m = +1$. The pumped transition goes from the ground state $5^2S_{1/2}$ with $m_J = -1/2$ to the excited state $5^2P_{1/2}$ with $m_J = +1/2$ (shown as the red line in Fig. 2.6). The population numbers of the of the excited state are quickly equilibrated by collisions with other atoms (buffer gases, mostly ^{4}He). The time scale for this so-called *collisional mixing* is in the range of 10 ps. Without buffer gases, the excited states would decay by the undesirable spontaneous emission of circular ($\sigma^{\pm}, \Delta = \pm 1$) or linear ($\pi, \Delta = 0$) polarized photons after a lifetime of around 30 ps. These photons can be absorbed by other Rb atoms, leading to the depolarization of the Rb electrons. In the presence of N_2 as a buffer gas (pressure around 0.5 bar), a radiationless quenching process into the ground states occurs, the so-called *radiation trapping* (see gray and black lines in Fig. 2.6). The lifetime of the excited states is greatly reduced to around 1 ps.
The elevated pressure in the optical pump cell leads to pressure broadening of the Rb absorptions lines by interactions between the electron hull of Rb and other atoms. The hyperfine structure of the alkali metal (the substructure of the absorption line due to

the interaction between electrons and nucleus) is unresolved. As a consequence of the broadened spectral line, a laser with a relatively broad emission spectrum (in general in the range of 1 to 2 nm) can be used without 'wasting' too much of the incident light power. Optical setups, which narrow the emission spectrum of the beam considerately using an optical grating, have been used by Chann et al. [Cha03] to obtain very high polarization rates.

2.4.2 Spin-exchange

After the optical pumping process polarizing the electrons of the Rb, the collisonal transfer of the polarization to the nuclei of Xe (or other noble gases) takes place. Figure 2.7 shows two different possibilities for this polarization transfer. The first is the formation of weakly bound van-der-Waals molecules by a ternary collison between ^{129}Xe, Rb, and N_2, where the excessive kinetic energy is transferred to the N_2-molecule. The second possibility consists of binary collisions between Rb atoms and ^{129}Xe atoms. For the system Rb–^{129}Xe with the highly polarizable electron shell of the noble gas atom, the formation of van-der-Waals molecules is more important than binary collisions at lower pressures (in contrast to the case of ^{3}He, where nearly only binary collisions play a role). Only at a pressure of ^{129}Xe higher than 0.5 bar, the spin transfer due to the formation of van-der-Waals molecules becomes negligible [Wal97, Wal98]. Since for ^{129}Xe, the spin-exchange rates are high (several orders of magnitudes higher than for ^{3}He (see [Cat92, Kil01]), the partial pressure of Xe inside the SEOP cell must be rather small (here around 70 mbar), leading to a continuous or semi-continuous realization of the polarization process (see [Dri96]). As mentioned above, the pressure inside the cell is increased by buffer gases up to several bars (here 7 bar). At these pressures, the formation of van-der-Waals molecules become also negligible: the spin transfer is only accomplished by binary collisions. According to [Ang08], the time-dependent buildup of nuclear polarization of ^{129}Xe, $P_{N(Xe)}$, in the SEOP cell with the incident laser light can be described as follows:

$$P_{N(Xe)}(t) = \langle P_{Rb} \rangle \cdot \frac{\gamma_{SE}}{\gamma_{SE} + \Gamma} \cdot (1 - e^{-(\gamma_{SE} - \Gamma) \cdot t}) \tag{2.19}$$

with $\langle P_{Rb} \rangle$ the time- and volume-averaged Rb polarization, γ_{SE} the spin-exchange rate (between Rb and ^{129}Xe), and Γ the longitudinal relaxation rate of ^{129}Xe due to all possible mechanisms (see Section 2.5). The spin-exchange rate of Rb–^{129}Xe is determined by the laser power, the photon efficiency, and the laser/cell geometry [Bab03]. Assuming a Rb polarization $\langle P_{Rb} \rangle$ near unity, the limiting factor of the polarization process is the longitudinal relaxation Γ of ^{129}Xe. The longitudinal relaxation is composed of several different possible relaxation mechanisms. These do not only play a vital role in the polarizing process, but also in the overall storage of hyperpolarized gases and are therefore described in the next section.

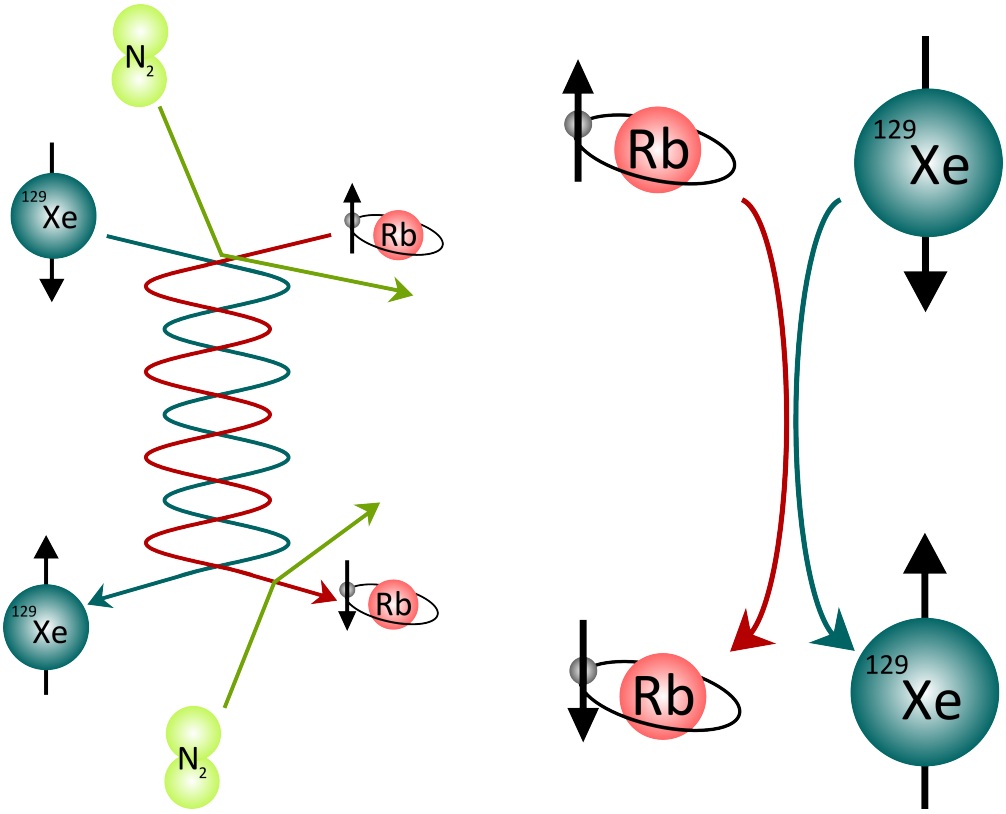

(a) Ternary collisions- van-der-Waals molecules - low pressure

(b) Binary collisions - high pressure

Figure 2.7: Two possibilities for the transfer of polarization from the Rb atom to the ^{129}Xenon nucleus

2.5 Relaxation of Hyperpolarized Gases

Once any hyperpolarization process has been stopped, the hyperpolarized state of a sample is destroyed by the return of the system and its spin population distribution to the thermal equilibrium. This longitudinal relaxation process is independent of any interactions with the system (e.g. measurements), and cannot be prevented. Because the storage of hyperpolarized gases is often necessary between polarization and use, a longitudinal relaxation rate as low as possible is important and very desirable for many applications.
The sources of relaxation of the system are numerous. In general, they can be divided into *intrinsic* relaxation, whose source is the presence of other noble gas atoms in the sample and whose dominant mechanism differs for different hyperpolarized gases and which cannot be avoided, and *extrinsic* relaxation, which in practice often dominates the total relaxation rate, but in principle can be reduced by technical or experimental means.

2.5.1 Intrinsic Relaxation Mechanisms

The intrinsic relaxation mechanisms of hyperpolarized gases include dipole-dipole interactions, which are dominant for ^{3}He, and spin rotation (SR) interactions and CSA, which together are dominant for ^{129}Xe. Both the SR relaxation and the CSA in the monoatomic noble gas are assumed to be caused by binary collisions (leading to *transient dimers*) and longer-lived van-der-Waals molecules (so-called *persistent dimers*) [BP06, Cha02]. The contribution of the persistent dimers is generally much larger than that of the binary collisions for ^{129}Xe. The mechanism of the SR relaxation can be suppressed by higher magnetic fields (decoupling of the interaction), where as the contribution due to the CSA is stronger for higher field (see Figure 2.8 and below). The possible relaxation due to dipolar interactions has been recognized very early as often negligible for ^{129}Xe compared to other intrinsic relaxation mechanisms [Tor63].

Dipolar (and quadrupolar) relaxation

The magnetic dipolar relaxation is caused by collisions between two noblegas atoms (i.e. ^{3}He–^{3}He), during which the two nuclear spins are coupled by the magnetic dipole interaction to their relative angular momentum [New93]. During this coupling, energy is transferred between the two atoms and the nuclear polarization is lost to the orbital angular momentum. The dipolar relaxation rates are rather long at low and intermediate pressures (especially for ^{129}Xe), but can be of importance for the 'long-time' storage of hyperpolarized noble gases. The following dipolar relaxation rates at 295 K and a pressure of 1 bar have been found for ^{3}He (spin $I = 1/2$):

$$\frac{1}{T_{1,dip}\,(^3\mathrm{He})} = \frac{1}{814.6} h^{-1} \qquad \text{from [New93].} \tag{2.20}$$

For the relaxation of ^{129}Xe, the relaxation due to dipolar interactions is often negligibly small compared to relaxation processes due to spin-rotation and chemical shift interactions (as explained below) [Ang08]. For noble gas nuclei with spin $I > 1/2$, the interactions during a binary collision of two atoms is not longer dipolar, but quadrupolar, which leads to higher relaxation rates. For ^{83}Kr with $I = 9/2$ and ^{21}Ne with $I = 3/2$, the following quadrupolar relaxation rates have been found:

$$\frac{1}{T_{1,dip}\,(^{83}\mathrm{Kr})} = \frac{1}{0.19} h^{-1} \qquad \text{from [Cle08].} \tag{2.21}$$

$$\frac{1}{T_{1,dip}\,(^{21}\mathrm{Ne})} = \frac{1}{66.0} h^{-1} \qquad \text{from [Gho10].} \tag{2.22}$$

Spin Rotation Relaxation

The SR relaxation is of special importance for the relaxation of ^{129}Xe in low magentic fields (somewhat below 5 T) at Xe densities below some amagats.[1] It occurs during short, binary collisions between two atoms which lead to transient dimers (collision duration

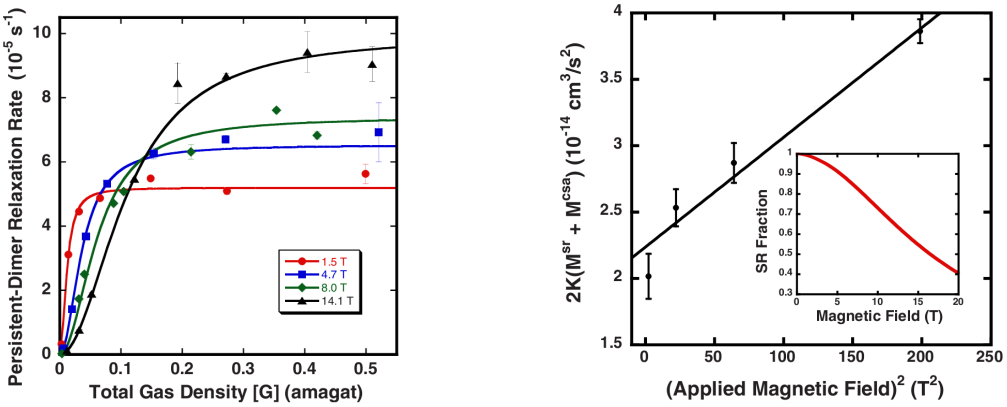

(a) (b)

Figure 2.8: The persistent dimer relaxation rates versus the total gas density at a fixed xenon concentration (a) and the relaxation due to persistent dimers versus the square of the magnetic field strength (b). The inset in (b) shows the the contribution of the Ş relaxation in dependence of the magnetic field strength. Both graphs are taken from [Ang08].

1 An amagat is the number of gas atoms or molecules for an ideal gas per unit volume at a pressure of 1.03125 bar (=1 atmosphere) and a temperature of 273.15 K.

around a few picoseconds), but also during the existence of longer-lived van-der-Waals dimers. The SR relaxation is caused by interactions between the nuclear magnetic moment and the magnetic moment created by the rotation of a dimer of noble gas atoms. The interaction can be decoupled by strong magnetic fields ($B > 1\,\mathrm{T}$) and the relaxation due to the spin-rotation can be suppressed effectively [BP06, Ang08].
For ^{129}Xe densities below 14 amagat, the relaxation due to persistent dimers exceeds that due to binary collisions [Cha02]. A low pressures and low magnetic fields, the SR relaxation limits the T_1 time of hyperpolarized ^{129}Xe rather drastically. The corresponding relaxation rate has been found experimentally to be:

$$\frac{1}{T_{1,SR}\,(^{129}\mathrm{Xe})} = \frac{1}{4.1}h^{-1} \qquad \text{from [Cha02].} \tag{2.23}$$

Berry-Pusey et al. calculated a slightly smaller minimal relaxtion rate due to SR relaxtion as:

$$\frac{1}{T_{1,SR}\,(^{129}\mathrm{Xe})} = \frac{1}{5.5}h^{-1} \qquad \text{from [BP06].} \tag{2.24}$$

Relaxation due to Chemical Shift Anisotropy

A significant amount of relaxation processes due to CSA has been found for hyperpolarized ^{129}Xe samples at higher and very high magnetic fields [BP06, Ang08]. Recently, Hanni et al. used experimental and simulation results to model the ^{129}Xe relaxation rates due to CSA. For a pressure of 1 bar at a temperature of 295 K, following (calculated) relaxation rates were given:

$$\frac{1}{T_{1,CSA}\,(^{129}\mathrm{Xe})} = \frac{1}{21.0}h^{-1} \quad \text{for } 8\,\mathrm{T} \text{ from [BP06].} \tag{2.25}$$

$$\frac{1}{T_{1,CSA}\,(^{129}\mathrm{Xe})} = \frac{1}{6.8}h^{-1} \text{ for } 14\,\mathrm{T} \text{ from [BP06].} \tag{2.26}$$

These values obtained from simulations are in relatively good agreement with experimental data given in [BP06, Ang08].

2.5.2 Extrinsic Relaxation Mechanisms

The extrinsic relaxation includes mechanisms like gradient-induced relaxation, surface (or wall) relaxation, and oxygen-induced relaxation. Extrinsic relaxation mechanisms are likely to be minimized by engineering efforts during the storage and the application of hyperpolarized gases.

Gradient-induced Relaxation

Since hyperpolarized gases are mostly polarized outside the superconducting magnet used in NMR or MRI applications [1], relaxation processes due to the transport of the hyperpolarized gas through magnetic field gradients are of great importance. Each superconducting magnet features an outer stray field, which is eventually crossed during the gas transport to the magnet, as well as a very strong *on-axis* magnetic field gradient, which the gas atoms perceive going from the low magnetic field outside the magnet to its homogeneous isocenter. In literature, studies of the relaxation in gases can be found in [Sch65, Cat88a, Cat88b]. The relaxation rate $\frac{1}{T_{1,grad}(^{\mathrm{HP}}\mathrm{Gas})}$ caused by diffusion of the hyperpolarized gas in transverse magnetic field gradients can be expressed as [Cat88a, Zhe11]:

$$\frac{1}{T_{1,grad}\,(^{\mathrm{HP}}\mathrm{Gas})} = D_{^{\mathrm{HP}}\mathrm{Gas}} \cdot \frac{|\vec{\nabla}B_x|^2 + |\vec{\nabla}B_y|^2}{B_0^2} \cdot \frac{1}{1 + (\omega_0\tau_2)^2} \tag{2.27}$$

where $D_{^{\mathrm{HP}}\mathrm{Gas}}$ is the diffusion coefficent of the hyperpolarized gas, $|\vec{\nabla}B_x|^2 = (^{\delta B_x}/_{\delta x}) + (^{\delta B_x}/_{\delta y}) + (^{\delta B_x}/_{\delta z})$, ω_0 is the Larmor frequency at the magnetic field strength B_0, and the corresponding correlation time τ_c is an approximation of the mean time between collisions of the atoms of the hyperpolarized gas. The last term is often neglected because it approaches unity under low field conditions. The relaxation due to magnetic field gradients is much less important for ^{129}Xe, which has a much lower diffusion coefficient (see also Section 2.3). According to the diffusion coefficent ratio between ^{3}He and ^{129}Xe, the relaxation rate should be approximately 35-times lower for Xe. Recently, Zheng et al. presented experiments on the relaxation of a hyperpolarized gas in the presence of the magnetic fringe field of superconducting magnets [Zhe11].[2] For ^{129}Xe, the shortest, gradient-induced T_1 time found in this study inside the gradient of the NMR magnet was around 140 min.

Surface Relaxation

Surface relaxation (also called wall relaxation) is caused by interactions between the hyperpolarized gas atoms and the wall of the container. It is in general influenced by the surface-to-volume ratio $^S/_V$ of the container and the material of the container as well as the temperature and the magnetic field strength [Dri95].

For ^{3}He, the wall relaxation can be decreased greatly by using special glasses without paramagnetic impurities in combination with a de-magnetization of the glass cell

1 It is possible to use a high magnetic field in the polarization process, as shown for example for ^{3}He at elevated pressures by Dohnalik et al. [Doh11].

2 They found a minimal T_1 time of 4.4 min for ^{3}He at around 0.5 m from the isocenter of a superconducting NMR magnet, which would have been even considerately shorter in a self-shielded superconducting magnet. In a superconducting MRI scanner, longer relaxation times around 10 to 15 min for ^{3}He have been found.

before use [Jac01, Sch06b, Sch06a] or by coating of the glass cell with alkali metal [Hei95, Den06].
For ^{129}Xe, Chann et al. state that the wall relaxation rates have probably been overestimated in the past because the strong source of relaxation of spin-rotation interactions of persistent ^{129}Xe-Xe dimers had not been taken into account. A recent study following these observations obtained relaxation rates $1/T_{1,wall}(^{129}\mathrm{Xe})$ for different glass cells between $1/2\,\mathrm{h}^{-1}$ and $1/16\,\mathrm{h}^{-1}$ in the low-field (around 3 mT) at gas densities of 1 amagat, and values as low as $1/174\,\mathrm{h}^{-1}$ in the high-field at 14.1 T [Ang08].

Oxygen-induced Relaxation

Relaxation due to the presence of paramagnetic susbtances is another contribution to the net relaxation of hyperpolarized gases. For ^{3}He and ^{129}Xe, oxygen is the most important paramagnetic gas, e.g. oxygen is always present during the imaging of lungs in vivo. The relaxation rates in dependence of the oxygen pressure p_{O_2} at a temperature of 295 K have been determined by Jameson et al. for ^{129}Xe and by Saam et al. for ^{3}He:

$$\frac{1}{T_{1,o_2}\,(^3\mathrm{He})} = \frac{p_{O_2}}{2.4}\,\mathrm{s}^{-1}\mathrm{bar}^{-1} \qquad \text{from [Saa95]} \tag{2.28}$$

and

$$\frac{1}{T_{1,o_2}\,(^{129}\mathrm{Xe})} = \frac{p_{O_2}}{2.8}\,\mathrm{s}^{-1}\mathrm{bar}^{-1} \qquad \text{from [Jam88].} \tag{2.29}$$

Apart from lung imaging applications, the oxygen-induced relaxation may be controlled and reduced by careful evacuation and flushing of the used storage containers for hyperpolarized gases. For long-time storage or measurements, small leakages from the atmosphere into the container should be considered (compare with [Ang08]).

2.5.3 Net Relaxation of ^{129}Xe

Anger et al. present a semi-empirical formula for the relaxation rate $\Gamma_{^{129}Xe}$ of ^{129}Xe in dependence of the gas density $[Xe]$ in amagat, the magnetic field strength B_0, and composition of a gas mixture [Ang08]:

$$\Gamma_{^{129}\mathrm{Xe}} = \frac{[\mathrm{Xe}]}{56\,\mathrm{h}} + \frac{1}{4.59\,\mathrm{h}}\left[1 + \left(3.65\cdot 10^{-3}\right) B_0^2\right]\left(1 + r\frac{[B]}{[\mathrm{Xe}]}\right)^{-1} \tag{2.30}$$

where $[B]$ is the density of another gas in the gas mixture in amagat, and r is the persistent dimer breakup coefficient of the second gas divided by that of Xe. Equation 2.30 is valid at room temperatures for $[Xe] > 0.3$ amagat at all reasonable values of B_0 and for lower Xe densities for $B_0 < 1$ T.

2.6 Polymerization reactions

The reaction of small monomer molecules forming polymer chains or networks is called *polymerization*. These polymer chains or networks (called macromolecules) have a high molecular weight (above 1000 g/mol and up to several 10^6 g/mol). The simplest type of polymer molecules, as used in this work, are so-called *homopolymers*. They consists of hundreds or thousands of covalently-linked, identical monomer units.

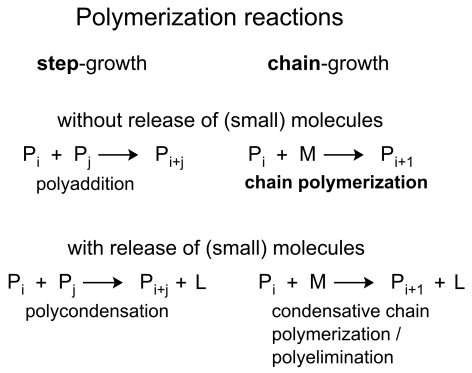

Figure 2.9: Different types of polymerization reactions. Adapted from [Eli09].

In general, any polymerization process can be classified by its chain-forming mechanism. Figure 2.9 gives an overview over different chain-forming mechanisms. The first distinction is made between *step-growth* and *chain-growth* mechanisms. Examples for the first mechanism are the polycondensation (release of small molecules (as H_2O during the polymerization reaction) and the polyaddition (reaction without release of small molecules): The macromolecule is synthesized in numerous distinct steps by the linkage of the monomer molecules, normally via ester-, ether-, amide- or urethrane formation.

The (industrially much more important) **chain-growth mechanism** consists of several different reaction phases: The formation of an active species or an active center (*initiation* reaction), the cascade-like reaction of the activated species with monomer molecules (*propagation* reaction), and the final reaction with either another active species under loss of the activity (*termination* reaction) or with a chain-transfer agent (e.g. initiator molecules, other polymer chains, monomer molecules) (*chain-transfer* reaction). The active centers are formed as radicals from certain initiators by homolytic bond breakage, as metal centers in metal complexes, or as ionic molecules (*initiation* reaction). For an overview over the wide field of polymerization reactions, see for example [Eli09].

Polymerization is currently one of the most important type of reactions of the chemical industry. In 2010, approximately $15.4 \cdot 10^9$ kg of polystyrene have been produced and used throughout the world with applications ranging from packaging to thermal insulation and many others.[1] The understanding and the control of the polymerization reaction and the product are of great importance in applications in research and industry, and many works can be found in literature [Beu02, Got04, Mue11]. One of the requisites

1 Numbers taken from http://www.sriconsulting.com/WP/Public/Reports/polystyrene/

towards this understanding is the monitoring of polymerization kinetics [Pen94, Bau10]. In this work, the free radical intiated polymerization of styrene to polystyrene in a miniemulsion is monitored by ^{129}Xe NMR spectroscopy.

2.6.1 Free radical polymerization

Free radical polymerization reactions are initiated by radicals and propagate by the growth of activated polymer chains [Mei90, Ish95]. Mostly, the radical initiators do not stem from the monomer molecules, but are formed from special initiator molecules. The radicals can be formed thermally, electrochemically, or photochemically from suitable initiators.[1] Figure 2.10 shows schematically the different reactions taking place during the free radical polymerization of styrene (phenylethene) to polystyrene (poly(1-phenylethan-1,2-diyl). Here, the radicals were formed thermally, at a reaction temperature of 343 K. From one initiator molecule, two radicals are formed:

$$\mathrm{I} \longrightarrow 2 \cdot \mathrm{I}^* \tag{2.31}$$

After the reaction with a monomer molecule, an active monomer radical is formed:

$$\mathrm{I}^* + \mathrm{M} \longrightarrow \mathrm{I—M}^* \tag{2.32}$$

By addition of monomer molecules, the polymer chain starts to grow and the *propagation* reaction reaction takes place:

$$\mathrm{I—M}^* + n\ \mathrm{M} \longrightarrow \mathrm{I—M}_n\mathrm{—M}^* \tag{2.33}$$

The initially radical-bearing molecule rest (I) stays at the end of the polymer chain, opposite to the radical-bearing end of the active polymer chain. For long polymer chains like the ones obtained by the free radical polymerization of styrene, the influence of these initiator rests can be normally neglected. The growth of the polymer chain is finished after a termination reaction takes place, which leads to the loss of the active entity.[2] In a free radical polymerization reaction, the growth of the polymer chain is very fast due to the short-lived nature of the radicals. Only at very high conversion, termination reactions by combination of two active polymer chains are hindered by the hindererd diffusion of the polymer chains, and the lifetime of the radical is increased, which leads to an increase in the reactions rate (*gel effect*).
Radical polymerization reactions can take place under a large variety of conditions and in different phases: in the gaseous phase, in solution, in bulk, or in emulsion or suspension.

1 Other radical forming mechanisms like plasma-, radiation-, or ultrasonic-induced polymerizations are mostly used in research applications or for modifications of an existing polymer (e.g. grafting).
2 Another possibility is the transfer of the activity to another (chain) molecule, which is called *chain-transfer* reaction.

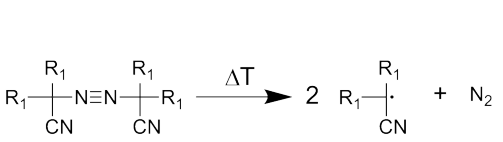

(a) Formation of radical

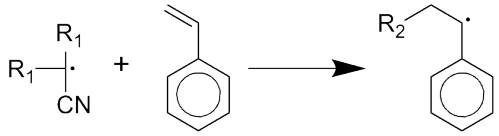

(b) Formation of active chain

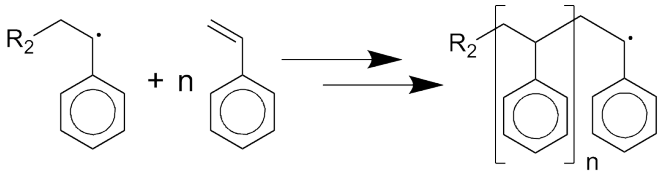

(c) Propagation reactions

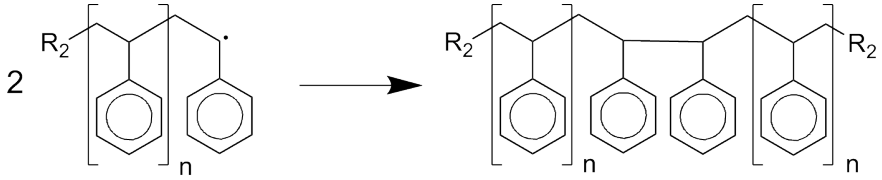

(d) Termination reaction 1

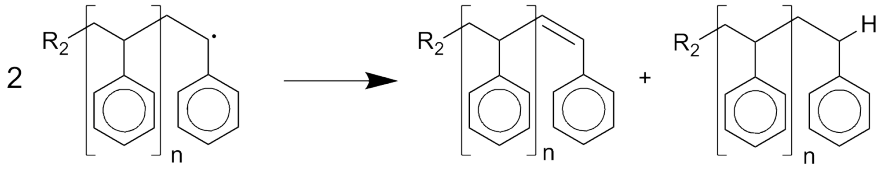

(e) Termination reaction 2

Figure 2.10: Schematic overview of different reactions during the free radical polymerization of styrene, showing the initiation reactions (a+b), the propagation reaction (c), adn two possible termination reactions (d+e).

The product of the polymerization can precipitate or dissolve in a solvent or the still present monomer. *Bulk polymerization* is the simplest type of polymerization, but during the ongoing reaction the product becomes solid (or very viscous). Since the wide majority of free radical polymerizations are exothermic (often with a very large reaction enthalpy), the heat of the reaction and its transport become very important, especially due to the increasing viscosity in bulk with ongoing reaction. At high temperatures, a decay of the already existing polymer chains back to the monomer units can take place.[1]

1 For polystyrene in bulk, the so-called *ceiling temperature* is very high at around 600 K.

Using *solution polymerization* reactions reduces the heat and viscosity issues to some extent, but at the cost of using organic solvents which are often toxic and harmful to the enviroment. Due to the dilution of the monomer molecules in solution, the polymerization rates are lower than in bulk. Moreover, the separation of product and solvent is often time-consuming and costly.
Another polymerization technique lies in the wide field of *dispersed phase polymerization* reactions, especially the *emulsion polymerization* reactions. In dispersed phase polymerization, two immiscible phases are present. Emulsions polymerization reactions are described in the literature since the forties of the last millenium [Fry44, Har47, Smi48], but are still an important topic in recent research, e.g. determining the influence of surfactants [Guo11, Fei12], or for the preparation of functional or functionalized nanoparticles [Hua01, Sha12]. Reviews of emulsion polymerization reactions can be found in [Nom04, Thi07].
In a conventional emulsion polymerization (or *macroemulsion polymerization*), the oil-soluble, organic monomer is dispersed in an aqueous phase by (mechanical) agitation and the help of a surfactant (surfactant-free emulsion polymerization reactions exist, but are less common). During the polymerization, the viscosity of the emulsion remains low, allowing for easy reaction control. The continuous aqueous phase allows for easy and effective heat dissipation. The product consists of a polymer latex with a size in the range of 50 to 500 nm. The polymer particles can be easily separated from the aqueous phase by precipitaion, centrifugation, or filtering.
Normally, a water-soluble initiator is used in emulsion polymerization reactions. After formation of active radicals from the initiator molecules, the polymerization reaction is started in very small monomer micelles (they outnumber the larger monomer droplets by far and thus, statistically, a active radical will enter such a small micelle). During the reaction, monomer molecules migrate through the aqueous phase into the monomer/polymer droplets where the reaction takes place. The kinetics of a conventional emulsion polymerization are not the same as for a polymerization in solution because the termination reaction between two active chains is largely reduced: It is statistically unlikely to have more than one active chain in a monomer/polymer particle. Therefore, the emulsion polymerization leads to higher molecular weights at constant polymerization rates.
The polymerization technique of emulsion and miniemulsion polymerization reactions are widely used in industry and science because of their good reaction heat dissipation, the constant, low viscosity of the reaction mixture, and high achievable conversion rates. In this work, a special emulsion polymerization technique, the so-called *miniemulsion poymerization* reaction, has been used. It will be discussed in detail in the next section.

2.6.2 Miniemulsion polymerization

Miniemulsion polymerization reactions are based on the polymerization of a **miniemulsion**, a special type of emulsion which is stabilized in a twofold manner: against coalescence by an effective surfactant and against Ostwald ripening by an osmotic

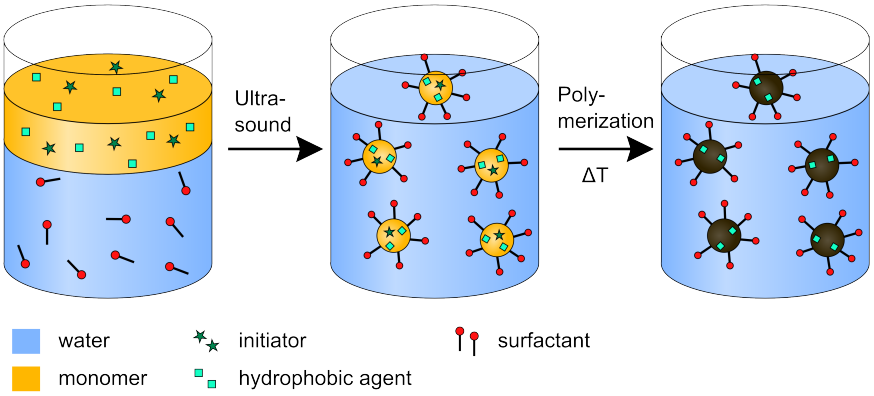

Figure 2.11: Schematic overview of a polymerization reaction in a miniemulsion: The two-phase system is homogenized by ultrasound, forming the miniemulsion. Upon initiation (here with thermal energy), the polymerization takes place and the product, a polymer latex, is obtained.

pressure agent [Sch05, Lan06, Lan10a].
Figure 2.11 shows a schematic overview of a miniemulsion polymerization reaction. Miniemulsions are formed by high-energy homogenization of a two-phase system (often by the application of ultrasound), yielding a stable emulsion (stable for hours up to weeks) with small droplets in a size between 50 and 500 nm with a narrow size distribution.[1] Contrary to the conventional emulsion polymerization, a single particle size is dominant. Most of the surfactant molecules are adsorbed at the droplet surfaces. Oil-soluble initiators are often used but the use of water-soluble initiators is also possible. The reaction is initiated and takes place inside the monomer droplets; due to the stabilization of the emulsion basically no transport of monomer can be observed between the droplets. The droplets of a miniemulsion serve as a kind of nanoreactor for the reaction which equals to a bulk polymerization inside the droplets. Statistically, half of the droplets contain an active polymer chain during the polymerization reaction (the volume of the droplets is too small to host more than one active radical) [Bec00]. The polymerization of styrene, an apolar liquid, in water as the polar, continuous phase is called *direct miniemulsion polymerization* (in contrast to the *inverse miniemulsion*). The product of a miniemulsion polymerization is a latex, a dispersion of the polymer particles in the continuous phase. The polymer particles obtained are approximately a 'copy' of the initial monomer droplets.
In addition to the preparation of "simple" polymeric nanoparticles by radical polymerization, miniemulsion polymerization allows using a broad range of monomers, conducting

1 Sometimes, smaller possible droplet diameters are denoted in the literature, e.g. 20-200 nm in [Sol05].

polyreactions as e.g. polycondensation or polyaddition reactions which are not accessible with conventional emulsion polymerization [Sch05, Ron05, Lan06, Lan10a, Lan09]. It further offers the possibility to encapsulate a variety of materials to generate functional nanoparticles [Lan10b, Wei11]. Studies related to the kinetic behavior of radical polymerization reactions in miniemulsions can be found in [Lan99, Bec00, Cun02], but as described above, the polymerization reaction inside the single droplets behaves similarly to a polymerization reaction in bulk.

2.7 NMR Spectroscopy of ^{129}Xenon in Porous Media

Porous materials consisting of nanocavities or nanochannels are capable to act as a host system for many different molecules and atoms. There are numerous technical and scientific applications of porous materials, for example the use of zeolites as adsorbents or ion exchangers or the use of metal-organic frameworks as catalysts or hydrogen storage materials [Bec92, Li99, Dav02, Ros03]. These materials generally consist of cavities smaller than 1-2 nm in different crystalline phases. Due to the size of the pores, they are often called nanoporous materials.
A promising class of nanoporous materials emerging in the last years are polymers with porous crystalline phases. In this work, syndiotactic polystyrene films were used, which are one example of these porous polymer materials [Dan09, Alb09b, Mil09]. A detailed description of the structure of the corresponding porous crystalline phases and their special properties can be found in this work in section 5.1.
One of the many possible molecular and atomic guests in nanoporous materials are Xe atoms. The diffusion of Xe atoms into and the (ad)sorption in the cavities of the material allows for the use of ^{129}Xe NMR to investigate the structural properties of these materials, an idea proposed by Fraissard and Ito et al. for ^{129}Xe in zeolites as early as 1982 [Dem82]. Until today, numerous experimental studies [Dem87, Lar93, Zha08] and theoretical calculations [Jam93, Jam94, Gup97] of NMR of xenon in zeolites and similar materials have been presented. However, many other porous media have also been used for Xe NMR experiments, like peptide crystals [Mou04, Bow07], metal-organic frameworks [Paw07, Hof11], mesoporous metal oxides [Paw10], and even soil components [Fil11] and wood cell structures [Kek10].
^{129}Xe is an excellent NMR probe for porous samples: Despite being a noble gas and therefore nearly inert to chemical reactions, the Xe atom is nevertheless very sensitive to its enviroment because of its large and very polarizable electron hull. No chemical bond is necessary between the Xe atom and the studied material, even small physical interactions are sufficient to cause (temporal) changes in the electron hull of the xenon atom. The confinement of adsorbed Xe atoms in porous materials lead often to drastic changes in the chemical shift and the line shape of the Xe NMR signal.
Several properties of the host system are responsible for these changes. Again, Fraissard and Ito proposed a simple model for the chemical shift δ of adsorbed ^{129}Xe in zeolites ([Dem87], see also [SH99]):

$$delta = \delta_{ref} + \delta_S + \delta_{Xe} + \delta_{SAS} + \delta_E + \delta_M \tag{2.34}$$

where δ_{ref} is the reference chemical shift (mostly the free Xe gas), δ_S is caused by interactions between Xe atoms and the walls of the cavities, δ_{Xe} is due to interactions between Xe atoms themselves inside the cavities, δ_{SAS} takes into account the possible presence of strong adsorption sites, and δ_E and δ_M are contributions of the electric and magnetic field of paramagentic centers (for examples cationic counterions in zeolites) if

present.
If no charged centers and strong adsorption sites are present in the porous material, the equation can be largely simplified (assuming $\delta_{ref} = 0$):

$$\delta = \delta_S + \delta_{Xe}. \tag{2.35}$$

The absence of charged centers can already be assumed for de-cationized zeolites and holds true for most porous polymer materials. The chemical shift δ in Equation 2.35 is only dependent on the shape and size of the cavities, the interactions between xenon atoms and the walls of the cavities, and the ease of diffusion of the xenon atoms in the cavities (combined in δ_S), and the Xe-Xe interactions (δ_{Xe}). The Xe-Xe interactions increase with the spatial density of xenon atoms inside the cavities. This dependency can be expressed by following equation:

$$\delta_{Xe} = \delta_{Xe-Xe} \cdot \rho_{Xe} \tag{2.36}$$

where δ_{Xe-Xe} denotes the increase in chemical shift due to collisions between xenon atoms and ρ_{Xe} is the density of xenon atoms adsorbed in the cavities. The chemical shift contribution can become dominant for large Xe densities.
On the other hand, by varying the Xe density inside the cavities and extrapolating to zero Xe density, the chemical shift contribution of the interactions between xenon atoms and the walls of the cavities, the term δ_S, becomes accessible. The term δ_S has been interpreted in context with the mean free path of the Xe atoms inside the cavities, which is determined by the size and the shape of the cavities. Porous polymer systems are another recent field for characterization experiments with Xe NMR spectroscopy. The technique allows for the characterization of free volume [Gol03, Emm10, Uti11], spherical pore sizes [Siv04], and gas diffusion [Soz06] in porous polymer systems.
A special case is the introduction of anisotropy by porous crystalline materials. Generally, crystalline materials give the possibility to deposit molecules or atoms in an anisotropic manner by deposition on their different crystal surfaces. Examples are the anisotropic deposition of L-cystine on gold nanoparticles [Fuj06] or numerous applications of chemical vapour deposition on different crystal surfaces (for example [Pri11]).
Using porous crystalline materials gives another possibility to cause anisotropy in respect to guest molecules or atoms: Inside the porous crystalline material, the shape of the cavities as well as the alignment of the cavities can cause a long range order of the guests molecules or atoms. By confining the guest molecules or atoms in the small cavities in the porous material, the complete averaging of the NMR signal over all possible orientations which takes place in fluid phases like liquids or gases is excluded. The orientation which can be found in the host material is transferred onto the guest molecules or atoms. After adsorption, the guest entities often align spontaneously inside the cavities without loosing all degrees of freedom.
^{129}Xe NMR results showing large influences of anisotropy have been presented for

a porous crystalline molecular solid [Soz00] and also for a single-crystal, where the macroscopic orientation of the single-crystal in respect to the B_0 magnetic field could be imprinted onto the adsorbed Xe atoms [Soz07].
In this work, ^{129}Xe NMR experiments on nanoporous syndiotactic polystyrene featuring oriented nanocavities and nanochannels were performed. The understanding of the nanoporous polymer system and its anisotropic influence on the ^{129}Xe NMR spectra is of great importance for the presented results. A detailed description of the polymer system can be found in Section 5.1, an tabular overview of the different samples can be found in Table 3.1.

3 Materials and Methods

3.1 Polarizer

The hyperpolarized ^{129}Xe used in this work is generated in a home-built SEOP polarizer which has been developed and constructed at the Research Center Jülich, Germany [App98, Mue07, Zae07, Amo07]. The main components of the polarizer setup are the diode laser system with the optical polarizer and the optical spectrometer, the Helmholtz coils generating the magnetic field, the actual pumping cell, and the gas handling system allowing for a constant gas flow. A schematic drawing of the setup is shown in 3.1. In order to protect the user from the laser beam and any accidental damage, the beam and the pumping cell are located inside aluminium housings (the Al housings can be seen on the right side in Fig. 3.6).

Laser and Optical Setup

The laser beam is produced by a fiber-optically coupled laser diode array (Duo FAP LX Scientific, Cohererent GmbH, Dieburg, Germany) with a nominal output power

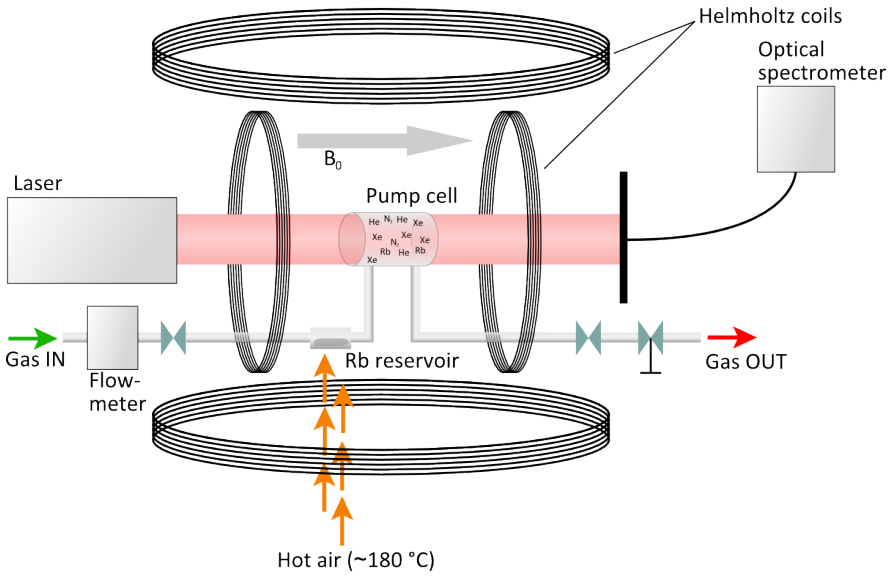

Figure 3.1: Schematics of a SEOP polarizer.

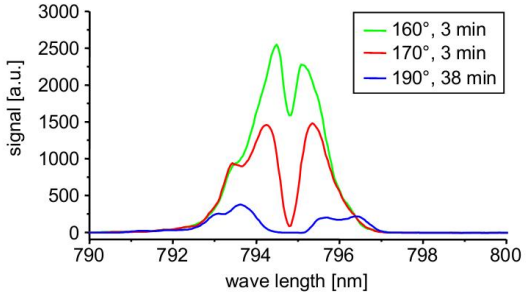

Figure 3.2: Absorption spectra measured with the optical spectrometer after the Rb vapour filled pumping cell for different temperatures at different times. The Rb absorption line is visible at 794.8 nm, the different amplitudes of absorption correspond to different Rb vapour densities in the pumping cell. Taken from [Zae07].

of 60 W. By using a high-power laser power meter, the actual power arriving at the pumping cell was determined to be approx. 40 W. The wavelength of the laser beam can be adjusted by changing the temperature of the laser diodes, and is set to a resonance frequency of the Rb atoms at 794.8 nm. The laser light has a spectral linewidth of approx. 2 nm. From the laser, the beam is guided into a circular polarizing unit, which splits the beam into two, right-circularly polarized parts, using a Glan-Thompson polarizer and two $\lambda/4$ plates. The beam leaving the polarizing unit perpendicularly is directed into the pumping cell by use of a mirror. Because not all laser light is absorped in the pumping cell, the optical spectrometer (HR2000, Ocean Optics Inc., Ostfildern, Germany) installed after the pumping cell allows for recording of absorption spectra (see Figure 3.2). Thus, the amount of Rb vapour inside the pumping cell can be controlled and adjusted by small changes of the temperature or the gas flow.
The high power laser was originally situated right above the polarizer box. Due to the high heat production of the polarizer setup, the cooling of the high-power laser was prone to fail in very long measurements (60 minutes or above). Because of that and because of considerations on the homogenity of the magnetic field (see below), the polarizer setup was taken apart and reconstructed at an angle of 90 ° with the laser device outside the small polarizer room.

Gas supply and flow control

The polarizer setup works at a 'high' total gas pressure of approx. 7 bar and allows for the production of approx. 0.1 $^{\mathrm{barliter}}/_{\mathrm{hour}}$ of hyperpolarized ^{129}Xe with a polarization of up to 15 %. It is continuously supplied with a flow of a gas mixture consisting of xenon (natural abundance or isotopically enriched), nitrogen and helium. The gas mixture is generated by a computer-controlled gas mixing unit which allows for individual ratios of mixed gases. The gas mixing unit consists of three digital mass flow controllers

(Bronkhorst EL-FLOW, Wagner M+R, Offenbach, Germany). Different mixing ratios are obtained by controlling the flow rates of the individual gases into a mixing cylinder (volume 500 mL). The total pressure of the gas mixture is limited by a digital pressure controller (Bronkhorst EL-PRESS, Wagner M+R, Offenbach, Germany) to a chosen output pressure. All flow rates and pressures are controlled and displayed by a computer. The normal operating pressure for the polarizer is 7 bar; the most often used gas mixture contains 1 % Xe, 8 % N_2 and 91 % He. The gas flow through the polarizer setup is measured by a digital flowmeter and is controlled by a manual needle valve at the exhaust. A normally used flow rate is approx. 50-60 $^{mL}/_{min}$. The flowmeter works by measuring the heat capacity of the flow through the polarizer. Therefore, the value shown at the flowmeter must be corrected for the high pressure and the used gas mixture. The actual flow rate at 7 bar in $^{mL}/_{min}$ is around 4.2 times smaller than the value displayed on the flowmeter at the polarizer.[1]

Heating and rubidium supply

The gas mixture flows into the optical pumping cell through the rubidium reservoir, a small enlargement of the flow tube containing between 200 and 750 mg of metal Rb on copper litz wire (see Figure 3.3). Both the Rb and the optical pumping cell are inside a glass compartment which is heated by hot air from a heat gun to temperatures between 150 and 230 °C. The heat gun is temperature controlled by a sensor inside the glass box. The thermal stability provided by the glass box is quite good but due to the flow and convection of the hot air, the thermal gradient between the inflow and outflow of the hot air can be up to 20 K. The different temperatures can cause the deposition of Rb inside the pumping cell which can lead to the reduction of the light intensity inside the cell.

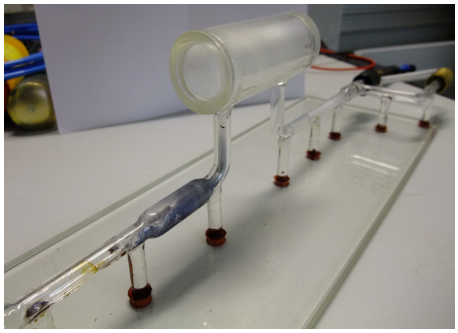

Figure 3.3: Rubidium reservoir seen from the entrance of the gas mixture. Also visible: The spread of the Rb due to transport by the hot gas mixture and the deposition of solid Rb inside the cell (white film).

The optimal temperature for the pumping process is around 180 °C. The temperature needed for a suffieciently thick Rb vapour atmosphere inside the optical pumping cell can vary for a number of technical reasons, it depends especially on the amount of Rb in and near the cell and on a possible oxidation of the Rb [Kil01, Mue07].
To create the rubidium vapour in an optically sufficient thick atmosphere, the Rb reservoir and the optical pumping cell are placed in a glass oven and heated to temperatures between 373 and 473 K (100 and 200 °C). The vapour density of the alkali metal, $[Rb]$

1 This difference between the displayed and the real value has not been taken into account in the past.

in units of [m^{-3}], can be calculated by the following empiric equation

$$[Rb] = \frac{10^{10.55-\frac{4132}{T}}}{1.38 \cdot 10^{-23}} \cdot \frac{1}{T} \tag{3.1}$$

Equation 3.1 uses values for the vapour pressure of Rb given in [Kil26] (also used in [Kil01, Rus05]), Figure 3.4 shows a plot of the vapour density versus the temperature. At an operating temperature of aapprox. 450 K (180 °C), the vapour pressure can be calculated to $4 \cdot 10^{15}$ [m^{-3}]. The actual Rb vapour density at a given temperature in the cell can vary greatly as the melting point of Rb (and accordingly the vapour pressure) even at low levels of oxdiation can vary over many centigrades [Kil01]. A phase diagram of the system Rb-O, showing the complicated phase behavior of Rb in dependence of the oxide content, can be found in [Suz86]. Given the long operation times of the Xe polarizer used in this work, the inevitable contamination of the metal Rb by small traces of oxygen in the gas flow required the repeated replacement of the metal Rb.

Coils and magnetic field

A magnetic field is necessary for the Zeeman splitting of the energy levels of the rubidium valence electrons as well as for minimizing the relaxation of the polarized ^{129}Xe atoms. It is produced by two Helmholtz coils with the magnetic axis parallel to the pumping cell. At a current of 3 A, these coils produce a magnetic field with a strength of 32 G (see Figure 3.5). Since the xenon polarizer setup is located in the stray field of a (poorly shielded) 4.7 T superconducting magnet, the homogenity of the holding field inside the polarizer was only on the order of $5 \cdot 10^{-3}$ with the largest gradient perpendicular to the orientation of the pumping cell. In order to increase the homogenity of the magnetic

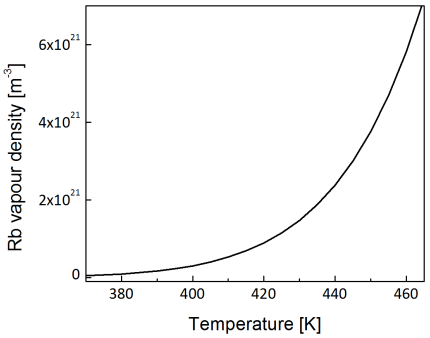

Figure 3.4: Estimation of vapour density of Rb as a function of temperature according to Equation 3.1 (see [Kil26]).

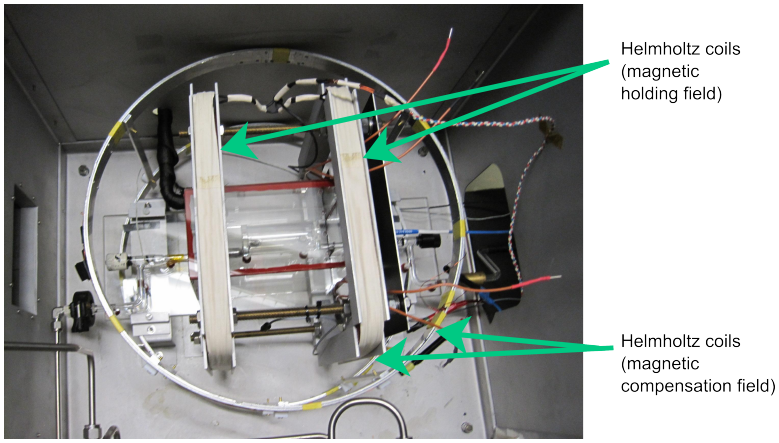

Figure 3.5: Picture of the pumping cell inside the Al box, showing the two sets of Helmholtz coils. The gas flow enters on the left side of the pumping cell and leaves on the right side. The laser beam enters the box from the sqaure openening on the left side, the beam stop and the optic fibre leading to the optical spectrometer are visible on the right side of the pumping cell.

field, an additional pair of Helmholtz coils has been installed (see Fig. 3.5). Additionally, the polarizer setup was rebuild at a new position at an angle of approx. 110 ° to its original position to take into account the stray field of the superconducting magnet. In Figure 3.6, the new position of the polarizer angled inside the room as well as the new position of the laser outside the actual polarizer room is visible.

(a) Laser **(b)** Polarizer

Figure 3.6: Pictures of polarizer setup after move, taking into account the stray field of a superconducting NMR magnet.

3.1.1 Different Operating Modes of the Xe Polarizer

Batch mode of the polarizer

The polarizer can be operated in a batch and in a continuous mode. The batch mode allows for the accumulation of hyperpolarized ^{129}Xe and the separation from the buffer gases by freezing the xenon gas out from the gas flow. Using the batch mode allows for the accumulation of sufficiently large quantities of Xe needed for many applications like lung imaging despite the low partial pressure used in the polarization process. The accumulation process and the corresponding setup are described in the next section 3.2.

Continuous mode of the polarizer

The continuous mode of the polarizer allows for experiments where a constant supply of hyperpolarized ^{129}Xe is needed over an extended time. In this work, the continuous mode of the polarizer was used for the online-monitoring of polymerization reactions with reaction times between 120 and 180 min.

Using the continuous mode, the gas flow from the polarizer is brought directly into the sample inside the NMR spectrometer. The hyperpolarized xenon portion of the gas mixture can be used in measurements either directly in the gas phase or it can be dissolved using different methods like the direct dissolution ('bubbling') or use of hollow-fibre membranes (so-called 'xenonizer', see section 3.6.1).

Figure 3.7 shows a schematic diagram of the fluidic system, including the polarizer and the sample inside the NMR spectrometer. For most of the tubing, polyurethane (PUR) tubes were used (Festo KG, Esslingen, Germany), mostly with an inner diameter of 3 mm. The length of the flow path between the polarizer and the NMR spectrometer was relatively long at approx. 5 m. With a typical gas flow rate of 50 $^{\mathrm{mL}}/_{\mathrm{min}}$ at 7 bar, the transport time for a gas volume leaving the pumping cell was 60 s. However, this long transport through the NMR laboratory does not destroy the Xe polarization as can be seen by the successful experiments in this work. Because of the long T_1 time of the gaseous ^{129}Xe, enough polarization is conserved until reaching the sample inside the NMR magnet (see Section 2.5).

The setup consists of several valves, actuated manually or remotely-controlled by pressurized air. The fluidic circuit allows for different flow passways of the gas mixtures: the bypass on the sample-near side allows for a continuous flow through the polarizer by giving simultaneously the possibility to change the sample or to remove the gas flow from the sample for a given time. The constant flow of dry gas through the sample can cause an evaporation of hydrophobic susbstances through the also hydrophobic membranes of the 'xenonizer'. Therefore, the flow can be diverted around the sample and through the bypass between subsequent measurements.

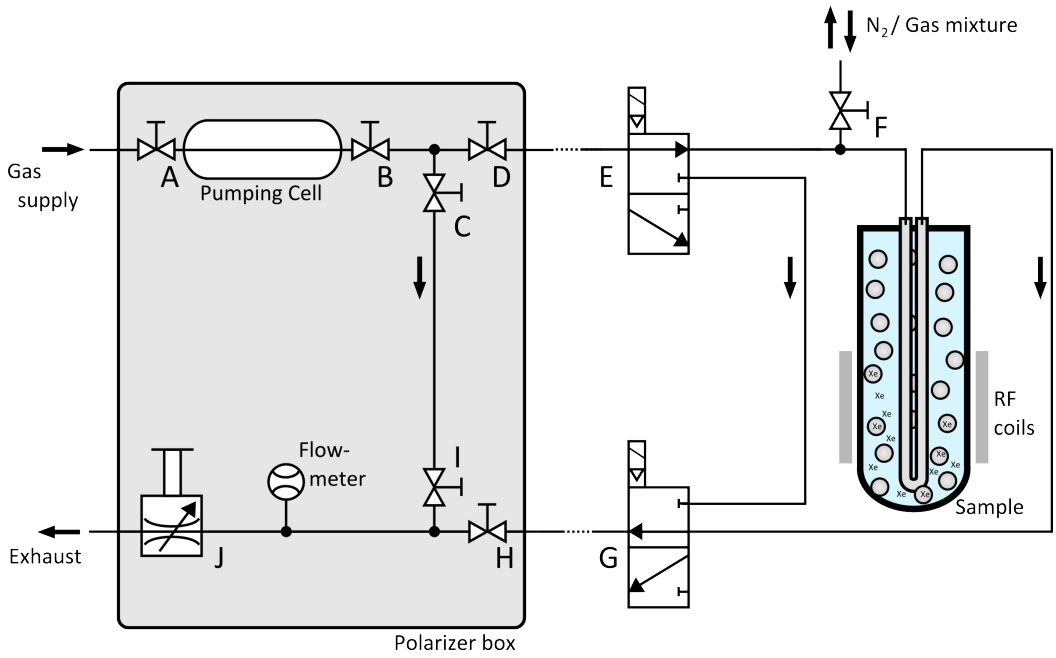

Figure 3.7: Schematic setup for the continuous mode of the polarizer. Valves E and G are switched simultaneously and allow for the switch between the routing of the gas mixture through the sample and the bypass near the NMR spectrometer. The shortcut in the polarizer box (provided by valves C, D, H, and I) allows for an initial adjustment phase.

3.2 Separation of HP ^{129}Xe – Accumulation as ice

The hyperpolarized xenon can be separated from the gas flow from the polarizer by using a cooling trap submerged in liquid N_2 (compare Section 2.2). At the operation pressure of 7 bar, xenon has a boiling temperature of 165 K and a melting temperature of 161 K. From the gas mixture of xenon, helium, and nitrogen used for the SEOP process, xenon is the only gas which can be frozen out from the gas mixture at the temperature of liquid N_2. The hyperpolarized Xe is accumulated as Xe ice on the inner surface of the cooling trap. The cooling trap and the N_2 are both positioned inside a transportable Halbach magnet, a permanent magnet array with a transverse magnetic field with a field strength of 0.3 T constructed from small permanent block-shaped magnets [Rai04]. The homogeneous magnetic field is necessary to conserve the hyperpolarization and reduce the relaxation of the polarized xenon ice. The accumulated amount is determined by the flow and the duration of the freezing out process.
After accumulation, the cooling trap is evacuated while still immersed in the liquid N_2 to remove the buffer gases. Figure 3.8 shows two different designs of cooling traps (or cells) which were used in this studies. The 'old' cooling cell design is a simple cold finger with a volume of approximately 24 mL. The frozen Xe is accumulated between the tip of the inner capillary and the constricted tip of the cooling trap. After long freezing times, the gas flow is blocked due to the accumulation of Xe in the capillary. The new designed cooling trap offers several advantages. It consists of a glass spiral with a diameter of 50 mm. The spiral is formed from 15 windings of glass tube with an inner diameter of 6 mm. The total volume of the freezing trap is with 36 mL larger than the 'old' freezing trap and allows for the accumulation of larger quantities of Xe at the same final pressure when thawed. Another advantage is the large inner surface of the glass spiral which allows for the accumulation of the Xe ice as a very thin layer. This thin layer should allow for a much faster thawing process after accumulation and thus, the reduction of relaxation of Xe in the liquid phase (see [Rus05]).

3.2.1 Automated freeze-and-thaw apparatus

In order to facilitate and automize the freezing and thawing process during the separation of hyperpolarized ^{129}Xe, a newly designed motor-operated and computer-controlled 'freeze-and-thaw' setup was built[1]. Figure 3.9 shows a schematic drawing and a picture of the apparatus. It consists of two glass dewars on a slidable stage below a holder for the Halbach magnet and the freezing trap. The two dewars are filled with liquid N_2 and water. The dewars fit into the inner diameter of the Halbach magnet and can be lifted from below into the magnet, suspending the cooling trap therein in N_2 or water. The lifting and lowering of the two dewars as well as the change between them can be carried

1 The automated freeze-and-thaw apparatus was constructed by XXX in-house at the MPIP, Mainz.

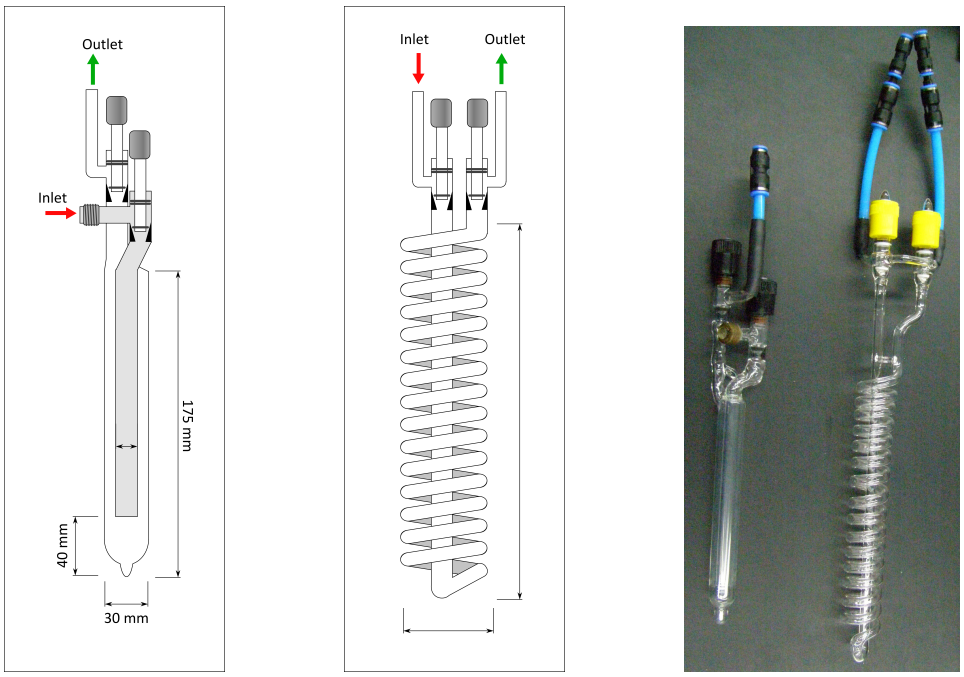

(a) 'Old' freezing cell

(b) 'New' freezing cell

(c) Picture of both freezing cells

Figure 3.8: Schematic drawings of the 'old', simpler (a) and 'new', helical (b) freezing cell and a picture of both freezing cells (c). In (c), the direct attachment of the polymer-tubes to the in- and outlets of the freezing cells is visible.

out by large linear actuators which can be controlled by a computer. Thus, the slow and steady immersion of the freezing trap into the cold medium causes the freezing out of a thin Xe ice film inside the glass spiral. The dewar containing the water at room or elevated temperature can be lifted very quickly by hand. The very fast immersion into the the warm medium leads in an optimal case to the quasi-instantaneous sublimation of the thin film of frozen Xe.

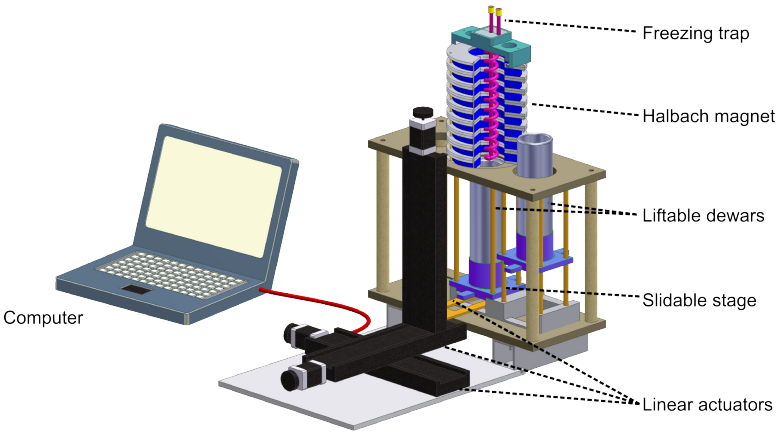

(a)

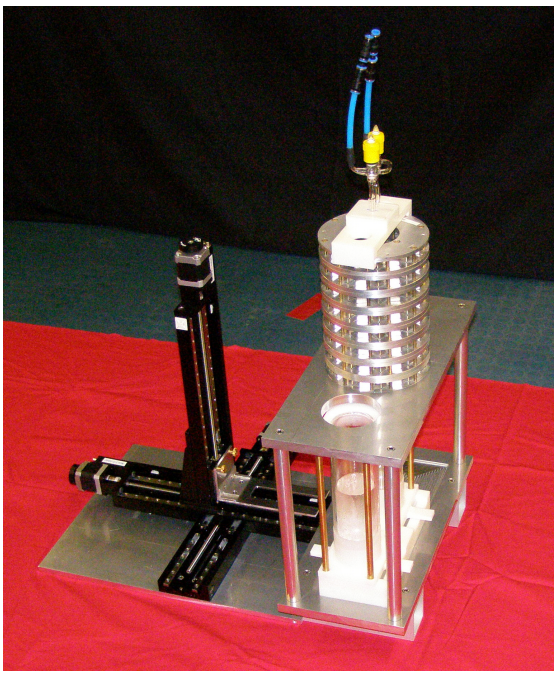

(b)

Figure 3.9: Schematic drawing (a) and picture (b) of the freeze-and-thaw setup, showing the two dewars, the Halbach magnet, and the two linear actuators which can lift the dewars automatically into the magnet.

3.3 Temperature control during NMR measurements

During the miniemulsion polymeriaztion experiments and the temperature-dependent measurements on the porous polystyrene films, the temperature inside the NMR magnet (including the NMR tube and the sample) had to be controlled. The sample and the RF coil inside were temperated by a flow of air or dry nitrogen at a choosable temperature. The preset temperature near the sample tube was measured by a temperature sensor in the air flow and controlled by a flow-through thermostat. For temperatures below room temperature, the gas flow was cooled by immersion into liquid N_2 inside a dewar.
Additionally, in order to measure and control the temperature inside the NMR tube, a so called 'NMR thermometer' was used (see [Amm82]): Using the same NMR tube as in the actual experiment, but filled with pure ethylene glycol, the temperature T_{sample} in [K] inside the tube can be calculated from the difference in the chemical shift $\Delta\delta$ of the $-CH_2$ and the –OH groups of ethylene glycole by the following equation:

$$T_{sample} = 466.50 - 102.00 \cdot \Delta\delta. \tag{3.2}$$

Equation 3.2 is valid in a temperature range between 273 and 416 K and was used during the miniemulsion polymerization experiments.
For temperatures below 273 K, methanol instead of ethylene glycol is used as the liquid inside the NMR tube. It allows for measurements in a temperature range between 178 and 330 K. The difference in the chemical shift $\Delta\delta$ of the $-CH_3$ and the –OH groups of methanol is used here. The NMR thermometer equation is changed accordingly:

$$T_{sample} = 409.00 - 36.54\Delta\delta - 21.85 \cdot (\Delta\delta)^2. \tag{3.3}$$

Equation 3.3 was used in the temperature-dependent measurements of the porous polystyrene films.

3.4 Gas mixtures for Determination of T_1 Times

In order to obtain gas mixtures with defined amounts of Xe and N_2, a similar procedure as described in [Zae07] and [AP07] has been used: After polarizing and freezing out for 35 min, the hyperpolarized Xe was thawed in the NMR magnet under the presence of an air flow at ambient temperature for 20 min (compare Figure 4.3). Subsequently, the pressure was reduced to 2 bar by a needle valve without moving the freezing cell. The pressure was measured by a non-magnetic pressure sensor (Sensortechnics GmbH, Puchheim, Germany) directly at the outlet of the freezing cell. Different Xe/N_2 mixtures were produced by pressing N_2 into the cell at a pressure of 6 bar (three time the pressure in the cell). After a mixing time for 30 s, the pressure was again reduced to 2 bar as described above. For mixtures containing larger amounts of N_2, this procedure was repeated.

In order to calculate the ratio of Xe/N_2 in a simple manner, a reference measurement was always performed on the pure Xe at 2 bar (before admixing any buffer gas). From the ratio of the signal amplitude of the reference measurement and the amplitude of the first scan of the gas mixture, the ratio Xe/N_2 was calculated, while neglecting any relaxation processes which take place during the buffer gas admixture.

3.5 ^{129}Xenon NMR in Porous Polystyrene Films

3.5.1 Polystyrene Film Samples

In this work, ^{129}Xe NMR experiments are performed on syndiotactic polystyrene films (see Chapter 5 for the results). All polymer films were prepared and provided by the group of XXX (University of Salerno, Italy). Because a good understanding of the polymer system is necessary for the interpretation of the ^{129}Xe NMR spectra obtained in this work, a detailed description can be found in Chapter 5 of this work (see also [Alb09b]).
The polystyrene films consists of different nanoporous phases forming cavities (δ phase) or channels (ε phase) inside the films. Here, a short overview of the film preparation is given: The oriented δ phase of the polystyrene films were prepared by casting commercially available syndiotactic polystyrene from solutions in chloroform. According to the desired orientation of the crystalline phases, the films were immersed in suitable solvents and subsequent guest removal with carbon dioxide at supercritical conditions. Thermal annealing of the δ phase films lead to the γ phase. From this dense phase, the porous ε phase can be obtained by recrystallization in chloroform vapour and chloroform desorption acetonitrile. More details on the film preparation can be found in [Mil01, Alb09b, Mil09].
The polystyrene films had macroscopic dimensions of approximately 10·25 mm and a

Sample number	Phase and orientation	Porosity	Degree of orientation	Crystalline phase [%]
01	amorphous	-	-	-
02	δ phase $a\parallel$ $c\perp$	cavities	0.75	30
03	δ phase $a\perp$ $c\parallel$	cavities	0.80	30
04	ε phase $c\perp$	channels	0.75	30
05	ε phase $b\perp$	channels	0.65	30
06	amorphous	-	-	-
07	γ phase	no	-	30
08	δ phase $a\parallel$ $c\perp$	cavities	0.85	30-35
09	δ phase $a\perp$ $c\parallel$	cavities	0.85	30-35
10	ε phase	channels	0.00	35-40
11	ε phase $c\perp$	channels	0.85	30-35
12	ε phase $b\perp$	channels	0.80	30-35

Table 3.1: Samples of the syndiotactic polystyrene films. The horinzontal line between sample 05 and 06 depicts the distinction between samples from the 'old' and the 'new' batch of films.

thickness of 100-300 µm. Besides the mechanical cutting of the films in suitable sizes (to fit in the NMR tubes), the films have been used as obtained. In Table 3.1, all used polystyrene film samples with their according porosity and orientation are listed. Two different batches of film samples have been used in this work, named 'old' and 'new' batch. Sample 01 to 05 are from the 'old', sample 06 to 12 from the 'new' batch.

3.5.2 Film Preparation - Positioning and Sampleholder

In order to measure the thermal signal of ^{129}Xe inside the porous polystyrene films, the films were cut into oblong slides (size 3·10 mm) or small squares (size 3·3 mm).
For measurements with the B_0 field parallel to the (macroscopic) film surface, the oblong slides were packed straight into the pressure-tight NMR tube (see Fig. 3.11, left side). The alignement of the film surfaces in this way is not perfect resulting in a small error of ca. ±3 °.
For the measurements with the B_0 field perpendicular to the film surface, a teflon sample holder was used,[1] allowing for the manual stacking of the small polystyrene squares inside the NMR tube (see Fig. 3.11, right side and picture in Fig. 3.10). A small teflon screw fixes the stacked film squares on top of each other. The angular deviation is smaller for this orientation, almost all film surfaces are perpendicular aligned to the axis of the B_0 magnetic field.
The teflon material of the sampleholder is not totally inert to the adsorption of xenon and thus, a signal occurs stemming from ^{129}Xe inside the teflon material. The NMR spectrum of xenon adsorbed in the sampleholder can be found in section 5.3.

Figure 3.10: Picture of the polystyrene films inside the NMR tube with teflon sampleholder.

1 Teflon sampleholder built by XXX, MPIP Mainz.

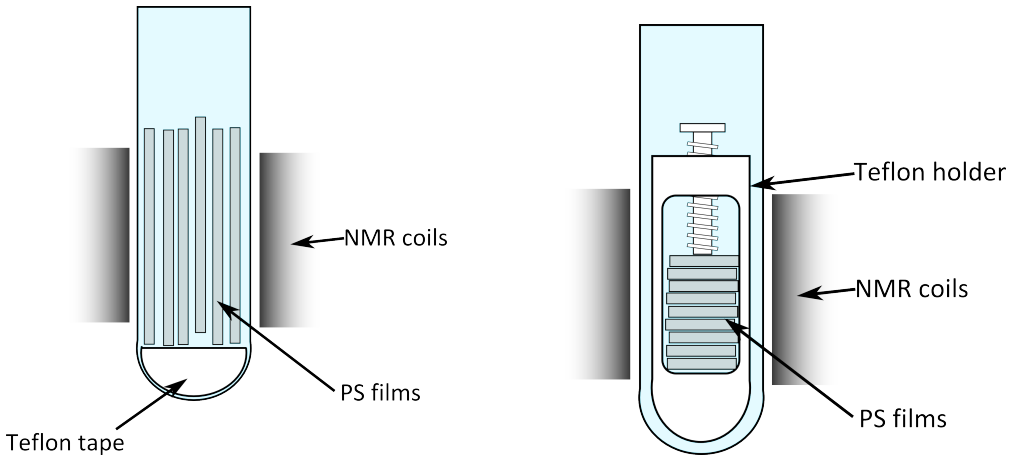

(a) Film surfaces parallel to B_0

(b) Films surfaces pependicular to B_0

Figure 3.11: Schematic drawing of the polystyrene films inside the pressurized NMR tube, with and without sampleholder. By using this setup, two different orientations of the film surfaces in respect to the B_0 magnetic field are easily achievable.

3.5.3 ^{129}Xe NMR measurements on Polymer films - Experimental details

Prior to the NMR measurements, the thick-walled NMR tube containing the polymer films was evacuated to a pressure of 10^{-3} mbar for 60 min. After the evacuation, the NMR tube was filled with isotopically enriched ^{129}Xe gas (isotopic purity >99 %) up to a pressure of 3.5 bar. The maximum pressure was put to the tube for a loading time of 30 s. To allow for diffusion of the xenon gas into the films and to guarantee a comparable equilibriated loading of the polymer films, a waiting time of 3 hours was introduced, after which the NMR tube was pressurized again up to a pressure of 3.5 bar for 30 s.
NMR spectra at room temperature (295 K) were recorded at 7 T at a resonance frequency of 82.82 MHz. Each scan consists of 2048 points recorded with a dwell time of 20 μs. Due to the low amount of polymer material and the long longitudinal relaxation time of Xe in the polymer, a large number of scans had to be used. For each spectrum, 12060 scans with a repetition time of 20 s were recorded. The total measurment time was 67 hours for each sample.
During the temperature-dependent measurements, the sample and the inside of the NMR magnet were temperated using a flow of cold nitrogen gas as described in section 3.3. The temperature and its constancy were controlled prior to the measurements with the 'methanol NMR thermometer' (see also 3.3). The ^{129}Xe NMR spectra were analyzed by using Matlab for fitting the Xe NMR spectra and determining the isotropic chemical shifts as the center of gravity of the adsorbed or dissolved xenon gas peaks.

3.6 Polymerization Reaction Monitoring in Miniemulsions

3.6.1 Dissolution of hyperpolarized ^{129}Xe — 'Xenonizer'

For the application of NMR of a hyperpolarized gas in liquid systems, it is crucial to provide a way of dissolving the hyperpolarized gas without loss of polarization. Sometimes it is possible to add the hyperpolarized ^{129}Xe directly into the sample (bubbling), but under gas flow conditions, the formation of bubbles and foam in the sample can be observed, which introduce large susceptibilty artifacts and render an accurate measurement impossible. To avoid these unfavorable situations, hollow-fibre membranes (hydrophobic surface, made from polypropylene (PE), pore sizes approximately 30 nm) from Membrana GmbH (Germany) were used in this work for the dissolution of the hyperpolarized ^{129}Xe (see [Bau06, Amo09, Cle09, Amo11]). In Figure 3.13, microscopic pictures and scanning electron micrographs of the membranes are shown. Bundles of single membrane fibres are sewn together, providing a dense packaging and a large effective membrane surface.

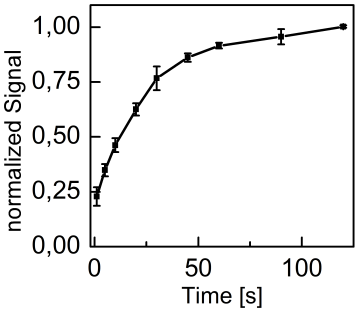

Figure 3.12: Normalized signal vs. time for the dissolution of hyperpolarized ^{129}Xe

The membranes allow for the fast and reliable molecular dissolvation of ^{129}Xe gas into the sample without the loss of hyperpolarization. After an equilibrium concentration of ^{129}Xe in the sample is reached, the gas also diffuses back through the membrane, thus providing a supply of polarized ^{129}Xe atoms in the sample. The surface of the membrane is hydrophobic which allows for the use of the membranes in aqueous environments but does not avert completely the diffusion of organic, more hydrophobic sustances across

(a) Bundle of membrane fibers

(b) Single membrane fiber

(c) Membrane pores

Figure 3.13: Hollow-fiber membranes[b]

[b] Images taken from http://www.membrana.com/oxygenation/products/celgard.htm

the membrane. Figure 3.12 shows the evolution of the normalized NMR signal amplitude after the gas flow has been switched from the bypass to the previously depolarized sample at $t = 0$. The signal amplitude increases exponentially as new polarized xenon dissolves into the sample and replaces the depolarized xenon. After 30 s, enough polarized xenon has been dissolved into the sample to give rise to 75 % of the maximal NMR signal amplitude.
Figure 3.14 shows a schematic drawing of the used setup. The membranes are glued into the PUR tubes which themselves are glued into home-made tube caps[1] made from polyether ether ketone (PEEK) providing in- and outlets for the gas mixture containing the hyperpolarized ^{129}Xenon as well as a tight seal applicable for pressures of up to 8 bar and temperatures of up to at least 350 K.

3.6.2 Free radical miniemulsion polymerizations of styrene

All NMR experiments related to the miniemulsion polymerization reactions were carried out in a 7 T NMR magnet equipped with a Tecmag console. Pressure-resistant NMR tubes (outer diameter 10 mm, inner diameter 5 mm) were used for all experiments.

Miniemulsion Polymerization Reactions

For the miniemulsions, styrene, sodium dodecyl sulfate (SDS), hexadecane (all purchased from Sigma-Aldrich, Germany), the initiators 2,2'-azobis(2-methylbutyronitrile) (V59, 10 h half-life decomposition temperature 340 K) and 2,2'-azobis(4-methoxy-2,4-dimethyl valeronitrile) (V70, 10 h half-life decomposition temperature 303 K, both initiators purchased from Wako, Japan) were used (the chemical structures of the two initiators are shown in Figure 3.15). The miniemulsions were prepared by mixing 24 g ultrapure H_2O (MilliQ-grade), 6 g distilled styrene (57.6 mmol), 60 mg SDS as surfactant (0.21 mmol), 250 mg hexadecane as hydrophobic agent (1.1 mmol), and either 100 mg V59 (0.52 mmol) or 100 mg V70 (0.32 mmol) as initiator, and the treatment with ultrasound (1/2" tip, 90 % amplitude, Branson Sonifier 450D) for 2 min, applied in 10 s pulses with 10 s break. During and after the emulsification, the miniemulsions were ice-cooled to reduce any possible polymerization prior to the measurements.
For the time resolved polymerization monitoring, 1.5 mL of the miniemulsion were put into the sample tube together with the membranes (see Figure 3.14 in section 3.6.1). After an initial pressurizing step, the gas flow containing hyperpolarized ^{129}Xe was fed through the membranes into the still cold sample tube for 2 min, allowing for the initial dissolution of Xe gas into the sample. Subsequently, the sample tube was inserted into the NMR magnet heated to 343 K. The insertion of the sample tube was considered as the time $t = 0$ for the polymerization reaction. Starting after one minute of reaction, ^{129}Xe NMR spectra were recorded. For each spectrum of the time-resolved measurements, four

1 Tube caps built by XXX, MPIP Mainz.

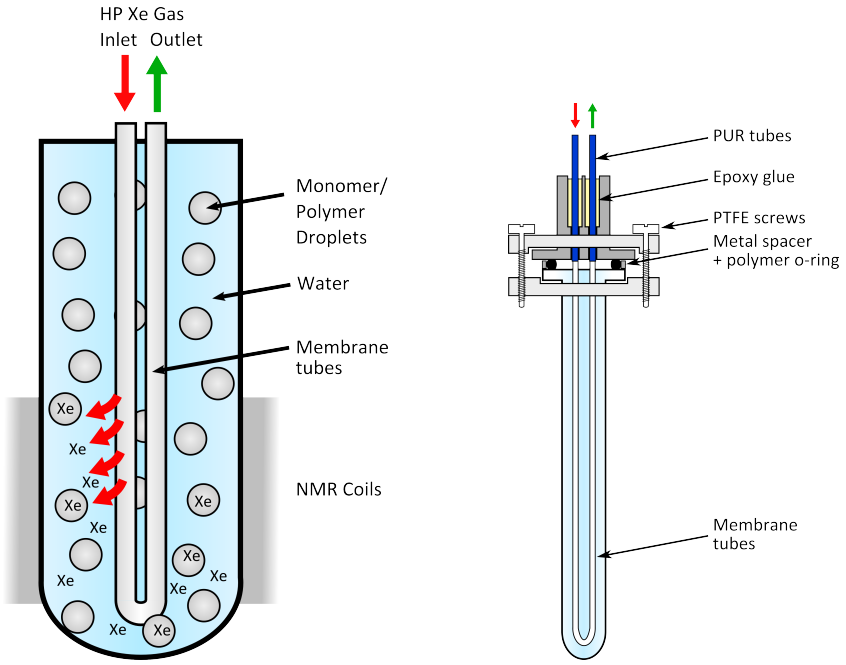

(a) Schematic drawing of xenonizer in liquid

(b) Connection of tubes to the NMR tube by PEEK caps

Figure 3.14: Xenonizer

(a) V70

(b) V59

Figure 3.15: Chemical structures of the two thermally activated, radical initiators used in the miniemulsion polymerization experiments.

scans with a repetition delay of 10 s were recorded to allow for a sufficient signal-to-noise ratio. For the first 10 min of reaction time, spectra were recorded every minute, for the next 30 min every 3 min, then until the first hour of reaction time every 5 min, and finally for the second hour of reaction time every 10 min.
All ^{129}Xe NMR spectra were analyzed by using Matlab for fitting the ^{129}Xe NMR spectra and determining the chemical shifts as the center of gravity of the adsorbed or dissolved Xe gas peaks. The peak of the free Xe gas was used as a reference and set to 0 ppm. In the case of two distinct peaks for the dissolved ^{129}Xe (beginning of the reaction), both peaks have been fitted and the mean center of gravity of both peaks was calculated and used for the further evaluation.

3.6.3 Mole-fraction Dependent Experiments

For the mole-fraction dependent experiments, polystyrene (mole weight 100,000 $g \cdot mol^{-1}$, polymer standard, PSS, Germany) and styrene (Sigma-Aldrich, Germany) were used. Nine mixtures of styrene and polystyrene were made with styrene mole fractions ranging from 0.95 to 0.3. Thermal ^{129}Xe NMR spectra of pure styrene, pure polystyrene, and the nine different monomer-polymer mixtures were recorded by averaging the thermal ^{129}Xe NMR signal for several hundred scans after evacuating the sample tube and pressurizing it with up to 3 bar of Xe gas. The ^{129}Xe NMR spectra were analyzed as described in the previous Section.

3.6.4 Calorimetry and further Characterization Techniques[2]

The calorimetric measurements were carried out on a RC-micro reaction heat calorimeter (Thermal Hazard Technology, UK) at 343 K. The sample volume was 1 mL. The solids content was determined by evaporation of the liquid phase from the dispersion at 323 K under a pressure of 50 mbar and weighing the solid residue. Particle sizes were measured by photon cross correlation spectroscopy (PCCS) using a Nanophox PCCS (Sympatec GmbH, Germany). For the measurement, 35 μL of the dispersion was diluted with 1.5 mL of MilliQ water. Scanning electron micrographs were recorded on a Gemini 1530 microscope (Carl Zeiss AG, Germany). From the electron micrographs, mean particle diameters were determined from 150 polymer particles for each polymerization. Size exclusion chromatography (SEC) was performed at 303 K with a Waters Alliance 2000 auto sampler, and Waters 510 HPLC Pump using PSS-SDV columns with pore sizes of 500, $1 \cdot 10^4$ and $1 \cdot 10^5$ Å, respectively. The signals were detected on an Erma UV

2 Calorimetry and further characterization measurements performed with the help of XXX and XXX, MPIP Mainz.

detector (λ =254 nm) and a SOMA RI detector. The eluent and the solvent for the samples was THF, the elugrams were calibrated against PS standards.

4 Towards Medical Applications of Hyperpolarized ^{129}Xe

Many applications, published or proposed, of NMR and MRI with hyperpolarized noble gases like ^{3}He, ^{129}Xe, or ^{83}Kr are connected with the field of medical science. Especially the use of hyperpolarized ^{129}Xe for imaging and spectroscopic applications seems to be promising because xenon dissolves in blood and other bio-relevant liquids and shows a suitable large range of chemical shift. Starting around 1994 with the imaging of excised rodent lungs by Albert et al. [Alb94], many other examples of NMR and MRI experiments with ^{129}Xe and other hyperpolarized gases can be found in the literature, escpecially for lung imaging (concerning ventilation [Kau00, Bec07, Pat07, Mee08, Hor09, Riz11a], but also the perfusion [Amo09, Dri09, Lor09]). Furthermore, xenon atoms can cross the blood-brain barrier, giving the possibility of perfusion measurements of the brain [Wak04, Maz11] and allowing the recognition of stroke [Zho11]. The administration of hyperpolarized ^{129}Xe is often carried out by respiration or forced respiration, but the administration of a bolus of a suitable solvent containing ^{129}Xe is possible, too. Figure 4.1 shows schematically the in- and outflow of hyperpolarized xenon in the bloodstream through the biophysiological membranes of the lung system.

In order to use hyperpolarized ^{129}Xe for imaging purposes in medical applications, it is normally accumulated as ice in liquid N_2 as described in section 3.1.1 and 3.2. There are several circumstances, however, which impede the simple use of the hyperpolarized gas:

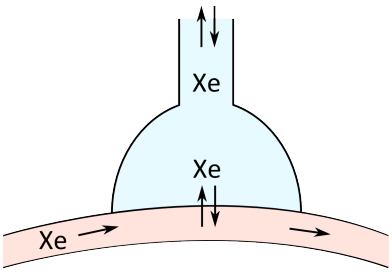

Figure 4.1: Schematic drawing of the possible flow of hyperpolarized ^{129}Xe in an alveolar.

The accumulation as ice is a discontinuous process which normally requires many manually operated steps. An automation of the process would work towards the simplification and reliability of the process. To this end, the automated freeze-thaw setup described in section 3.2 has been designed and built during this work. Below, results concerning the signal strength after thawing of the frozen hyperpolarized ^{129}Xe using the new setup are presented.

Since a xenon polarizer is a somewhat complicated setup, the polarizer is often not present at the imaging facilities. For application, the ^{129}Xe has then to be polarized and transported to the imaging facilities. Considering the inevitable decay of the polarization due to the longitudinal T_1 rate of the polarized ^{129}Xe, the time available for transport

is far from being unlimited.[1] Considering the total measurement time of an extensive MRI examination in the range of 1/2 hour, applications (especially for more than one proband or patient) may be limited by the T_1 time. Thus, extending the T_1 time of a hyperpolarized sample during storage and transport by simple means would be advantageous for many applications and a promising improvement. Below, results are shown for experiments in which the hyperpolarized ^{129}Xe is mixed with N_2 as a buffer gas to reduce the dipolar relaxation taking place between ^{129}Xe and therefore enhancing the T_1 time.
For MRI applications, the *contrast* of an MR image is of great importance in oder to distinguish regions with different properties. The contrast may stem from the density differences of the observed spins or from different relaxation rates due to different surroundings (this holds true for ^{1}H as well as for ^{129}Xe MRI). One important parameter in the MRI of hyperpolarized gases in lungs is the diffusion of the gas during the measurement. The obtained contrast of the MR images is changed by different diffusion coefficients, the (preferred) imaging of smaller or larger hollow structures is possible. By determining the (apparent) diffusion rates of hyperpolarized gases in structures, conclusions about the structure of the imaged cavities are possible. Below, some results are shown for MRI experiments where the diffusion coefficient of hyperolarized ^{129}Xe has been changed by the admixture of a buffer gas.

4.1 Optimization of the Separation/Accumulation process of ^{129}Xe

As described above, an important step in the use of hyperpolarized ^{129}Xe in (medical) imaging applications is the separation of the hyperpolarized xenon from the gas mixture from the polarizer. Using the new, helical freezing cell, the maximal usable signal amplitude of a hyperpolarized ^{129}Xe sample after the separation step (i.e. after freezing and thawing) was determined for three different thawing methods. The three different methods reflect three typical thawing methods used in experiments before.
All the methods use the general separation approach described in Section 3.2, using liquid N_2 in a dewar to freeze the xenon out and the Halbach array magnet to generate the magnetic field during the accumulation process (also thawing in case of Method 3). A freeze-out time of 15 min at a gas flow of 50 $^{mL}/_{min}$ was used in all experiments. For Method 1, the N_2 containing dewar was removed after the freezing out, leaving the freezing cell fixed inside the Halbach magnet. After evacuation, both the cell and the magnet were brought into the vicinity of the NMR magnet, and the cell was subsequently brought into the NMR magnet and coil. After a thawing and equilibration time of 15 min under an airflow at ambient temperatures, the pressure and the temperature of the freezing cell and its content were assumed to be at ambient conditions (compare

1 That is nearly the case for hyperpolarized ^{3}He, where T_1 times of >100 h have been found which in principle allows the transport of the gas to the whole globe.

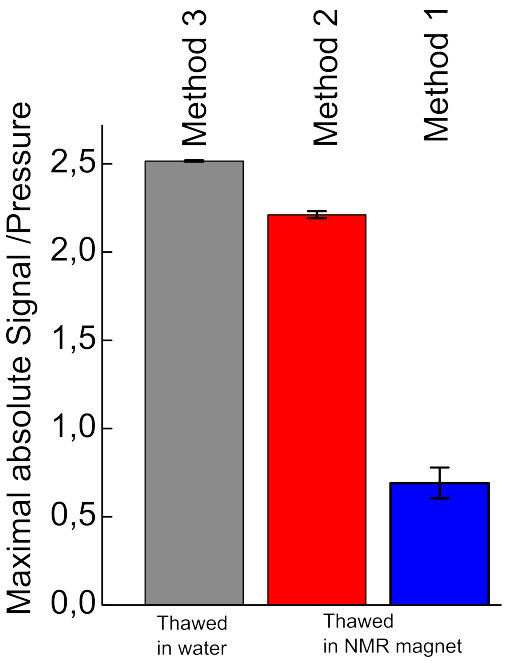

(a)

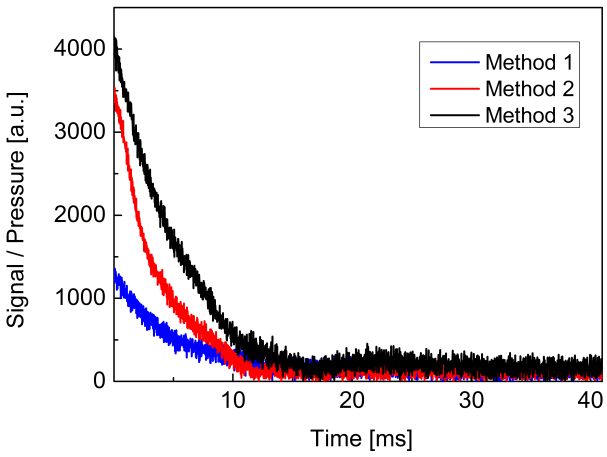

(b)

Figure 4.2: (a) The graph shows the absolute amplitudes of the first point of the FIDs for the three different methods of thawing the frozen xenon (Method (1) in blue, method (2) in red, method (3) in black). The maximal signal amplitudes have been corrected by the different pressures. (b) Three representary FIDs of the ^{129}Xe obtained by the three different thawing methods, illustrating the relative enhancement of usable signal by using the newly-built freeze-thaw setup.

with Figure 4.3), and a FID was recorded.
For Method 2, after the freezing out process and the evacuation of the cell, all three components (Halbach magnet, N_2 containing dewar and freezing cell) were brought into the vicinity of the NMR magnet, and again, the cell was subsequently brought into the NMR magnet and coil. Again, after a time period of 15 min, a FID was recorded. The FIDs for Method 1 and 2 were recorded 19 min after the freezing out process was finished (4 min for evacuation and handling of the freezing cell and the described 15 min thawing time).
For Method 3, the frozen xenon was thawed inside the Halbach magnet by help of a second dewar containing water at room temperature, instead of inside the NMR magnet. Using this method, the thawing is quasi-instaneous (no development of the pressure can be observed during the thawing, but only a pressure jump to the final pressure value). After the thawing process, the Halbach magnet with the freezing cell were again brought to the NMR magnet and the freezing cell was inserted into the magnet and coil. The FID was recorded instantly after the insertion of the cell in the magnet. The measurement took place 4 min after the freezing out process was finished.

Figure 4.2 (a) shows the average values of the maximal absolute signal amplitudes of the FIDs obtained after the three described thawing methods. For each method, three single experiments (polarizing, freezing out, thawing) were carried out. Due to fluctuations in the gas flow through the polarizer, which cannot be ruled out completely, the final pressures in the freezing cell was slightly different for all experiments. In order to account for these difference, the maximal signal ampltudes were normalized by dividing the maximal signal amplitude by the final pressure in the freezing cell. The maximal signal amplitude of Method 1 is much smaller than these of Method 2 and 3 (only 32 and 28 % of the maximal amplitude, respectively). The large difference can be attributed to the transport of the freezing cell from the polarizer to the NMR magnet **outside** the liquid N_2, resulting in the thawing of a large part of the frozen xenon. During the transport of the cell and its insertion into the NMR magnet, large magnetic field gradients (due to the strayfield of the NMR magnet) are crossed. ^{129}Xe is much more sensitive concerning relaxation in the gaseous state in the presence of these magnetic field gradients. Therefore, extensive relaxation processes take place before the freezing cell can be placed in

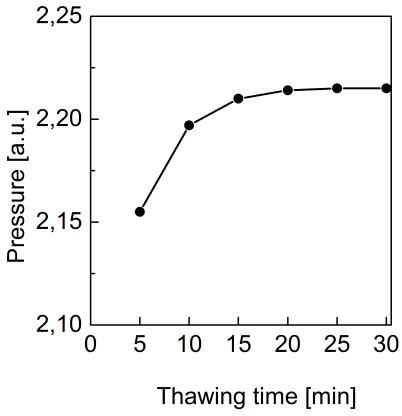

Figure 4.3: The graph shows the pressure inside the freezing cell for a cell containing initially frozen Xe (pressure 1 bar at room temperature) under an airstream inside an NMR magnet. The majority of the thawing process takes place at times t <5 min, after 15 min the final pressure is reached to 99.8 %.

the homogeneous magnetic field inside the NMR magnet and the maximal usable NMR signal amplitude is greatly reduced. Thus, Thawing Method 1 proved to be inapplicable for the production of hyperpolarized ^{129}Xe for imaging applications. The difference between Method 2 and Method 3 is much smaller. Although the thawing process of Method 3 takes place in the Halbach magnet, whose magnetic field homogeneity is worse than that of the NMR magnet, Method 3 gives the largest maximal signal amplitude with the smallest deviations, around 12 % larger than that of Method 2 (in relation to the maximal signal amplitude of Method 3). Both methods seem in principle suitable for the production of hyperpolarized ^{129}Xe, but a large advantage of Method 3 (i.e. the thawing by means of insertion of the freezing cell into water) is the speed-up of the whole separation process by omitting the time-consuming thawing and equilibration step, leading to the benefit of a measurement which is possible at a much earlier time point.
Using the newly-built freeze-thaw setup, not only a large gain in speed and reproducibility, but an enhancement of the 'usable polarization' of over 10 % could be found. When using the freeze-thaw setup with computer-controlled linear motors and valves, a semi-continually operation mode of the polarizer seems feasible due to the extremely short thawing periods.

Cell Design	T_1 time [h]
'Old'	1.3
'New'	4.0

Table 4.1: T_1 times for gaseous ^{129}Xe in the two different freezing cells.

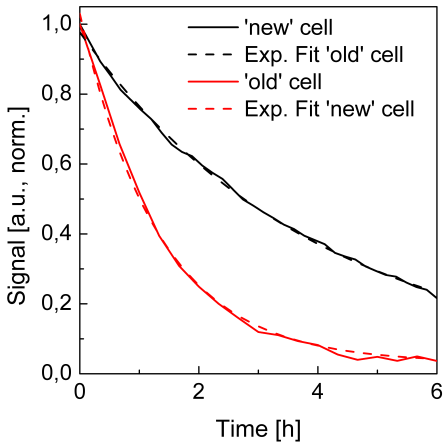

Figure 4.4

4.2 T_1 Times of Gaseous HP ^{129}Xe

4.2.1 Comparison of T_1 Times in two different Freezing Cells

As described in Section 3.2, two different freezing cells were used in this work, one a simple cold finger ('old' cell), which has been used for several years, and one consisting of a helical glass tube ('new' cell), providing a larger storage volume and a large inner surface. Both cells have been used both for the accumulation of ^{129}Xe and for its storage prior to experiments. For the storage, the most important factor is the relaxation rate of the hyperpolarized gas, which is preferably as low as possible in order not to lose (too) much of the valuable nuclear polarization. To prove the usability of the new freezing cell, T_1 times of hyperpolarized ^{129}Xe gas in the two different freezing cells were measured. Figure 4.4 shows two T_1 measurements of 1 bar of pure, hyperpolarized Xe gas in the two different cells. The exponential fit of the decay following Equation 2.14 gives the T_1 times noted in Table 4.1. Surprisingly, the relaxation rate is slower for the new freezing cell by a factor of 3 (1.3 h versus 4 h). In comparison, longitudinal relaxation times in deflating polymer bags (Tedlar bags) which are often used for the application of hyperpolarized gases during MRI experiments were found to be around $2.55\,\mathrm{h} \pm 0.22$ [Moe11].
Since the gas pressure was the same in both freezing cells, the relaxation due to intrinsic mechanisms like intermolecular interactions are the same in both experiments. Following the contributions to the relaxation described in Section 2.5, the most probable reason for the large difference in the relaxation time originates from different surface relaxation rates for both freezing cells. Different kinds of glass used for the freezing cells could be a reason for the difference. Moreover, the extensive use of the 'old' freezing cell has possibly lead to the contamination of the inner surface of the cell with rubidium. The deposited metal ions act as paramagnetic relaxation agents, decreasing the effective relaxation time. Another trivial source of paramagnetic relaxation, a small inflow of oxygen due to an incomplete sealing of the freezing cell, can be ruled out due to the fact that both freezing cells hold gas pressures of several bars for weeks.
Using the semi-empirical calculation of the relaxation rate given in Equation 2.30 (see also [Ang08]) with the used gas pressure 1 bar at 295 K, which corresponds to a gas density of 0.91 amagat, and a magnetic field strength of 4.7 T, the longitudinal relaxation rate would be 4.0 h. This calculated value matches the experimental value for the 'new' freezing cell. Assuming the correctness of Equation 2.30, no further increase in the longitudinal relaxation time can be expected by use of other freezing cells for gaseous Xe at these conditions. In order to increase relaxation times and gain access to longer storage times, lower gas pressures or the introduction of an buffer gas must be used, both at the cost of a reduced storage volume. Results on the admixture of a buffer gas are presented in Section 4.2.2.
For the future, it could be interesting to measure an evolution of T_1 times for the 'new' freezing cell during its use in subsequent experiments in order to see whether a ongoing

deposition of Rb from the gas flow during the freezing-out process will likewise lead to an increased relaxation rate. For the storage of hyperpolarized gases for time periods as long as possible, it would be helpful to use a setup which includes the controlled deposition of any Rb **before** the gas flow enters the freezing cell. A possible setup, which allows for the separation of the Rb vapour from the gas flow while still illuminated from the laser light, is presented in [Rus05]. Another possibility is the use of separated freezing cells and storage cells for the hyperpolarized gas. Thus, any Rb would only be deposited in the freezing cell and its influence would be limited to short periods.

4.2.2 T_1 Times of of Gaseous HP ^{129}Xe in Gas Mixtures with N_2

As described in Section 2.5, the presence of persistent dimers (^{129}Xe–^{129}Xe) in the gaseous phase is a large, and often dominant, source of relaxation. To reduce the relaxation, it has been proposed to admix a buffer gas to the Xe gas to increase the break-up rate of these persistent dimers and thus decrease their lifetime. Thus, the longitudinal relaxation time of hyperpolarized ^{129}Xe can be increased (compare with [Ang08, Cha02]). Two buffer gases considered for the T_1 time increasing admixture are He and N_2, which are present in the gas mixture before the accumulation process of Xe and which are inert and non-toxic for (human) imaging purposes.
Here, the longitudinal relaxation times of pure hyperpolarized Xe and two different

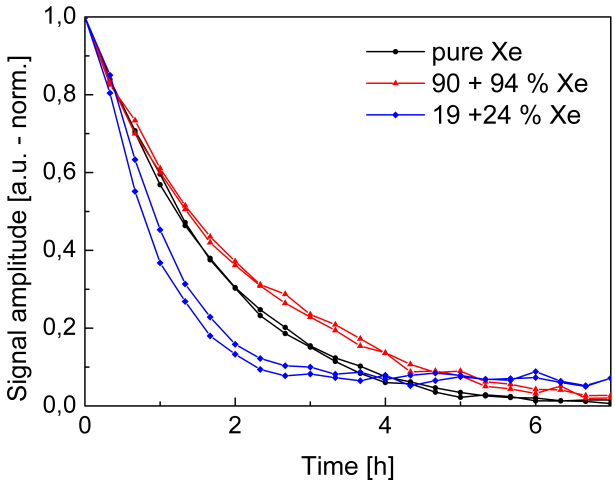

Figure 4.5: The maximal signal amplitudes of series of FIDs plotted against the time are shown for pure Xe (black), 90 %+94 % Xe (red), and 19 %+24 % Xe (blue). Using the procedure using described in Section 3.4, the amount of admixed buffer gas cannot be completely controlled quantitatively during the admixture, but the exact amount is subsequently determined exactly by an NMR experiment.

Approx. amount of Xe [%]	T_1 time [h]
100	1.63
90	1.96
20	0.93

Table 4.2: T_1 times for different gas mixtures.

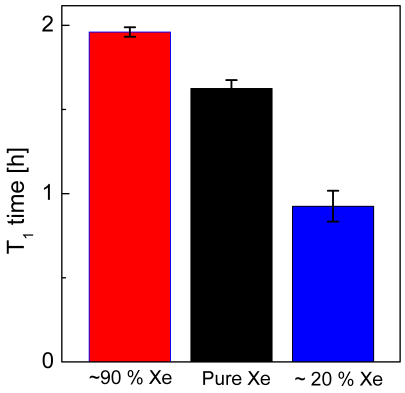

mixtures of with N_2 have been determined at a pressure of 2 bar and temperature of 295 K at a magnetic field strength of 4.7 T. Compared with He, N_2 should have a larger influence on the lifetime of the persistent Xe dimers ([Ang08, Cha02]) and thus was used in this work as the admixed buffer gas. The gas mixtures have been prepared as described in Section 3.4 and the ratio Xe/N_2 has been determined accordingly. For mixing purposes, the 'old' freezing cell has been used in these experiments.[1] The amount of admixed buffer gas cannot be completely controlled quantitatively during the admixture process, but the admixed amount is determined subsequently by an NMR experiment. To obtain the relaxation times, series of FIDs have been recorded (one measurement each 15 min), starting after the thawing or the admixture of the buffer gas, respectively. Figure 4.5 shows the maximal signal amplitudes for the three different samples in respect to the measurement time. These exponential decays have been fit according to Equation 2.14. Table 4.2 gives the relaxation times for the three samples. The longest T_1 is obtained for mixtures containing around 90 % of hyperpolarized Xe and 10 % of N_2 (1.6 amagat Xe vs. 0.2 amagat N_2) with approx. 2 h, exceeding the relaxation time of pure Xe gas by 20 %. According to Equation 2.30 and using an persistent dimer break-up factor $r = 0.5$ (taken from [BP06]), a smaller increase of around 7 % would be expected for such a mixture. The increase in relaxation time observed here would correspond to a value for $r = 1.75$ which is much higher than reported in the cited literature.

For the mixtures containing around 20 % Xe and 80 % of N_2 (0.4 amagat Xe vs. 1.4 amagat

1 Similar experiments with the 'new', helical freezing cell did not show any differences after the supposed admixture of the buffer gas: Instead of mixing with the Xe gas, the buffer gas was pressed into the freezing cell as a bolus and subequently removed during the pressurizing-down step.

N_2), only very short relaxations times could be obtained in spite of the expected **increase** in the relaxation time: Equation 2.30 would suggest relaxation times $> 10\,\mathrm{h}$ for these mixtures in which case, of course, other extrinsic relaxation mechanisms as the wall relaxation would limit the effective obtainable relaxation times. The most probable reason for this drastic decrease of the T_1 time is an experimental imperfection in the mixing procedure, which was performed two times in this case, during which an amount of O_2 is involuntarily added into the freezing cell, allowing for an effective relaxation.

4.3 Diffusion-weighted Imaging of Gas Mixtures of Xe and N_2

When using hyperpolarized gases, MR images are often influenced by diffusion of the gas. A strong diffusion weighting of the image and the loss of image quality cannot be averted, especially at longer echo times. Agulles-Pedrós et al. [AP09] presented a method to influence the diffusion weighting of a ^{3}He MR image at given echo times by control of the diffusion coefficient. By admixing slower buffer gases to the very mobile helium atoms, a large gain in SNR for large hollow structures was obtained. For a simple gradient echo imaging sequence as used in this work, the signal attenuation due to the diffusion in dependence of an experimental factor b can be expressed as follows (compare [Ste65]):

$$\frac{lnS(b)}{S_0} = -b \cdot D = \gamma^2 G^2 \delta^2 \left(\Delta - \frac{\delta}{3}\right) \cdot D \tag{4.1}$$

with γ the magnetogyric ratio, G the gradient strength, Δ the delay between the starting points of the two bipolar gradient pulses and S the NMR signal amplitude. In the

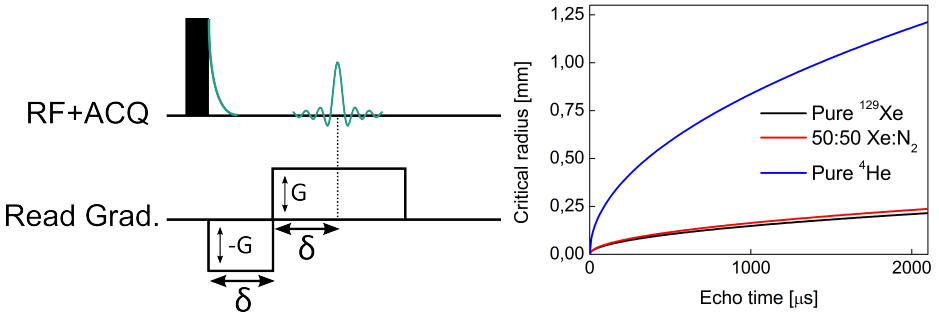

(a) Sequence. **(b)** Critical radius.

Figure 4.6: Simplified MRI sequence and critical radius r_c versus the echo time for pure ^{4}He (blue), pure ^{129}Xe (black), and a 50:50 Xe:N_2 mixture (red).

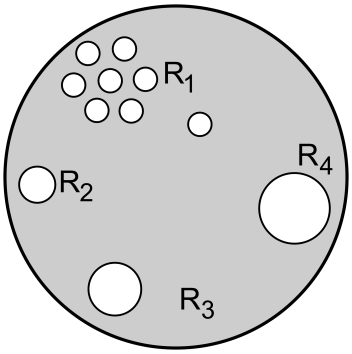

(a) Schematic drawing of the phantom.

(b) pure He (1 bar)

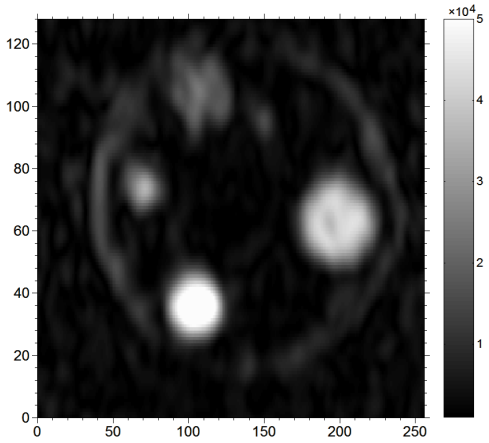

(c) pure Xe (1 bar)

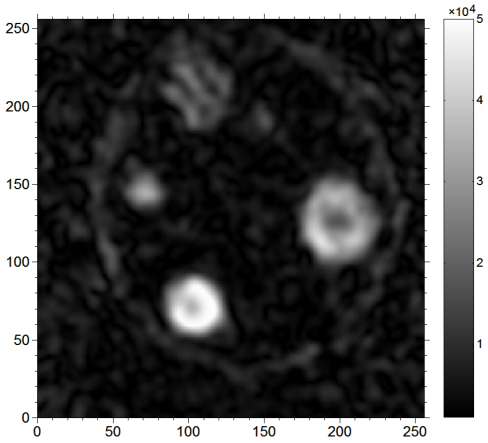

(d) Xe-N_2 (50:50, 1 bar)

Figure 4.7: A schematic cross-cut of the capillary phantom used in the imaging experiments (a) and three MR images of the phantom filled with 1 bar of hyperpolarized pure ^{3}He (b, taken from [AP09]), pure ^{129}Xe (c) and a 50:50 mixture of hyperpolarized ^{129}Xe and N_2 (d). The radii of the capillaries of the phantom are R_1 =0.75 mm, R_2 =1.4 mm, R_3 =2.4 mm, and R_4 =3.2 mm. The echo time for all three MR images is approx. 1.8 ms. For the Xe images, scans with 64 pixels with 64 phase gradient steps were recorded and 2D-FT transformed into 256^2 matrices.

experiments here, $\delta = \Delta$ was used as can be seen in the (simplified) NMR pulse sequence in Figure 4.6 (a).
The mean square displacement $\langle r^2 \rangle$ of a spin in this NMR experiment between excitation and detection can be calculated by

$$\langle r^2 \rangle = 2D\,(\delta + \Delta)\,. \tag{4.2}$$

Regarding the diffusion of a gas in a thin capillary, the radius $\widetilde{R}_{cap}$ of the capillary is related to the displacement as $\widetilde{r}$ is a one dimensional variable ranging from $-\widetilde{R}_{cap}$ to $+\widetilde{R}_{cap}$. Using $\delta = \Delta$, the following equation can be derived:

$$\langle r^2 \rangle = 4D\delta. \tag{4.3}$$

From this equation, an expression for the so called *critical radius* $\widetilde{r}_{crit}$ can be derived, over which the diffusing spin does not encounter any borders:

$$\widetilde{r}_{crit} = \sqrt{4D_0\delta} \tag{4.4}$$

with D_0 the free diffusion coefficent of the observed species. When the capillary possesses a radius smaller than $\widetilde{r}_{crit}$, the rate of diffusion can be expressed by the apparent diffusion coefficent (ADC) which is (generally) smaller than the free diffusion coefficient. The ADC is dependent on the size of cavity (here: the radius of the capilllary) and the duration of the gradients used in the imaging sequence (compare with Equation 4.4). The diffusion coefficent D can then be expressed by following equation:

$$D\,(\widetilde{r},\delta) = \begin{cases} ADC = \frac{\langle r^2 \rangle}{4\delta} & \text{for } r < \widetilde{r} < \widetilde{r}_{crit} \\ D_0 & \text{for } \widetilde{r} > \widetilde{r}_{crit} \end{cases}. \tag{4.5}$$

For small, very fast diffusing gases like ^{3}He, it is useful to minimize the duration of the bipolar gradients (δ and Δ) during the imaging sequence in order to minimize the influence of diffusion (according to Equation 4.1). In practice, the gradient strength - and therefore the gradient duration - is mandated by the field of view (FOV) and the number of points across the k-space trajectories. Two different effects are observed in read direction and in phase direction. In read direction, if the spatial resolution is well below the critical radius, a very strong attenuation of the signal will take place and the structure cannot be resolved. In phase direction, for very high rates of diffusion or very small structures, a blurring with a Gaussian distribution function will occur.
Compared with the free diffusion coefficient D_{He} =1.8·10^{-4} m^2/s of ^{3}He at a pressure of 1 bar, the free diffusion of ^{129}Xe with D_{Xe} =5.5·10^{-6} m^2/s is nearly 1.5 orders of magnitudes smaller. By admixing buffer gases like N_2, the diffusion coefficient of the gas mixture is decreased instead of increased as it is the case for ^{3}He.
In Figure 4.6 (b), the critical radius of a cyclindrical capillary is plotted against the echo time 2δ for ^{3}He, ^{129}Xe and a mixture of ^{129}Xe and N_2 in the ratio 50:50 at a pressure of

1 bar. The large difference between ^{3}He and ^{129}Xe concerning their diffusion coefficient is visible: With an echo time of 1000 μs, the critical radius for ^{129}Xe is over five times larger than for ^{3}He. The difference between pure ^{129}Xe and a gas mixture of ^{129}Xe and N_2 in the ratio 50:50 is much smaller (around 15 μm or 10 % for an echo time of 1000 μs). In order to go below the critical radius when imaging ^{129}Xe, structures (e.g. pores or capillaries) with very small diameters or very long echo times in the imaging sequence have to be used. Both of these requisites increase the difficulty of the experiments, by requiring a very fine spatial resolution (which is more difficult to obtain for ^{129}Xe than for ^{3}He due to the smaller magnetogyric ratio) and by the relatively short T_2-time (which is again much shorter for ^{129}Xe than for ^{3}He).
However, as a proof of principle, images of a capillary phantom filled with pure, hyperpolarized ^{129}Xe and the 50:50 Xe:N_2 mixture were acquired. The capillary phantom is the same than that described in [AP09] and consists of a number of glass capillaries with different diameters from 0.75 to 3.2 mm. A cross cut of the phantom can be found in Figure 4.7 (a). In Figure 4.7 (b-d), three different MR images of the capillary phantom are shown. In (b), an image of the capillaries filled with 1 bar hyperpolarized ^{3}He is shown (taken from literature [AP09]), whereas (c) and (d) depict hyperpolarized ^{129}Xe MR images. For all images, the echo time was chosen to be relatively long, i.e. 1.8 ms. A difference between the He and Xe images lies in the better spatial effective resolution of the He images, visible in the much clearer depiction of the small capillaries with radius R_1. For ^{3}He, the critical radius is larger than those of the imaged capillaries at an echo time of 1.8 ms, which manifests itself also in the weak and distorted reproduction of the larger capillaries (R_2 to R_4).

As described above, only for very long echo times, the critical radius for the slowly diffusing ^{129}Xe becomes large enough to matter. As can be inferred from Figure 4.6 (b), the critical radius for pure Xe and for the 50:50 Xe-N_2 mixture at an echo time of 1.8 ms is 2.2 and 2.0 mm, respectively. Thus, the capillaries with the radii R_3 and R_4 (right and bottom center) should be larger than the critical radius in both cases. However, the expected (strong) signal attenuation and deterioration in image quality, as can be seen in the He image for the capillaries with larger radii, cannot be observed here. The large structures show the highest signal amplitudes for both the pure Xe and the Xe-N_2 mixture. Nevertheless, comparing the images obtained from pure Xe and the Xe-N_2 mixture (Figure 4.7) (c) and (d)), the so called effect of *edge enhancement* can be observed for the two larger

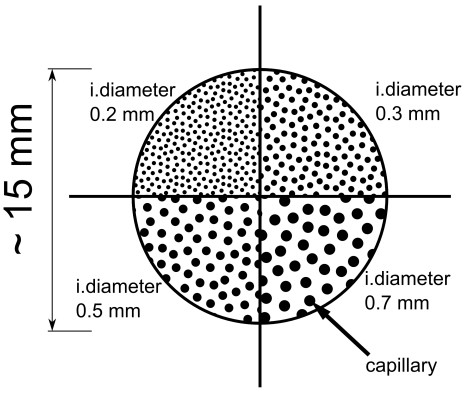

Figure 4.8: Possible new capillary phantom.

capillaries. By admixing the N_2, the diffusion coefficent has been increased by around 21 % (from $5.5 \cdot 10^{-6}$ to $6.7 \cdot 10^{-6}\,\mathrm{m^2/s}$). By admixing higher volumes of N_2, it would be possible to alter the diffusion coefficent of the gas mixture more strongly, but only at the cost of loss of signal amplitude due to further dilution of the ^{129}Xe. The use of even longer echo times proved to be difficult due to the fast $T_2{}^*$ relaxation of the ^{129}Xe between excitation and detection. Shorter echo times would be preferrable to obtain a sufficient signal.
As the capillary phantom used in these experiments features hollow structures with rather large diameters, it would be helpful for future experiments to build a new phantom using microcapillaries with much smaller dimensions. A proposal for a new phantom can be found in Figure 4.8. The proposed capillary diameters would be under (0.2 mm), right around (0.3 mm) and over (0.5 and 0.7 mm) the critical size for pure ^{129}Xe at a shorter echo time of 1 ms. These diameters are in the range of small structures in the human lung. It will not be necessary to resolve the small capillaries (which will be difficult for ^{129}Xe MRI), but due to the high density of capillaries, the measurement of an averaged ^{129}Xe signal will suffice to demonstrate different contrasts caused by different diffusion coefficients of gas mixtures.

4.4 Conclusion

In this work, several improvements for medical applications of hyperpolarized ^{129}Xe were achieved and the feasibility of the proposed improventments could be shown experimentally.
The use of the new automated freeze-thaw apparatus gives a large increase in speed and reliabilty in the separation process of the hyperpolarized ^{129}Xe as well as an increase of the usable polarization of $> 10\,\%$. Besides a larger storage volume, the 'new', helical freezing cell proved to be advantageous concerning ^{129}Xe relaxation times, exhibiting an increase in the longitudinal relaxation time by a factor of three. The further lengthening of the effective relaxation time proved to be feasible with a relatively simple setup, e.g. offering an increase in longitudinal relaxation time of 20 % by decreasing the stored volume of hyperpolarized ^{129}Xe by 10 %. When using a simple setup for the gas admixture, special care should be taken in respect to the involuntarily admission of oxygen into the stored gas mixture, which effectively destroys the polarization. The influence of a change in the rate of diffusion in ^{129}Xe MR images could be shown. By using of a newly proposed phantom, this effect should be much more distinct, allowing for conclusions for ^{129}Xe MRI of lungs in the future.

5 ^{129}Xenon in Nanoporous Polystyrene Films

In these studies, nanoporous polystyrene films have been investigated by ^{129}Xe NMR spectroscopy. The polymer films feature nanosized empty cavities, either isolated or connected, the latter type forming channels through the films. The cavities or channels are oriented to a certain degree inside the films by a suitable film preparation (for a description of the film preparation, see Section 3.5). The hollow space of the cavities and channels can be filled, at least partially, with ^{129}Xe atoms by spontaneous adsorption, allowing for NMR spectroscopy experiments on these films. As described in Section 2.7, ^{129}Xe NMR spectroscopy is often used in material sciences to characterize (nano-)porous materials. Due to the nanoporous structure of the syndiotactic polystyrene films and their related uptake ability of molecular guests, a proposed application of one of the crytalline phases of the films lies in the removal of ethylene in food packaging [Alb08b]. By using ^{129}Xe NMR, a distinction between films with different crystalline phases and orientations is possible. Furthermore, it is shown that the orientation of the cavities inside the films transfers to adsorbed ^{129}Xe atoms (see Section 5.2). By simply changing the macroscopic orientation of the polymer film, the anistropic orientation of adsorbed ^{129}Xe atoms to the external magnetic field is changed. This orientational change can be easily observed by changes of the chemical shift of adsorbed ^{129}Xe (Section 5.3). In addition, experiments on the temperature-dependence of the ^{129}Xe chemical shift were performed in this work (Section 5.4).
As the structure of the used polymer system is important for the interpretation of the Xe NMR experiments, a detailed description of the polymer systems is given in the next section.

5.1 Polymer system

The polymer films are formed from syndiotactic polystyrene, a thermoplastic polymer system which features several crystalline phases, two with trans-planar polymer chains (α and β phase, accessible from the polymer melt)and three with helical chains (δ, ε, and γ phase, accessible from polymer solutions and co-crystals with solvent molecules) [Riz05, Mil09]. Two of these phases of syndiotactic polystyrene are nanoporous. They are able to include small guest molecules or atoms in their pores. The two phases are the δ crystalline phase and the ε crystalline phase which consists of nanosized cavitities and channels, respectively [Gue09a, Alb09b].

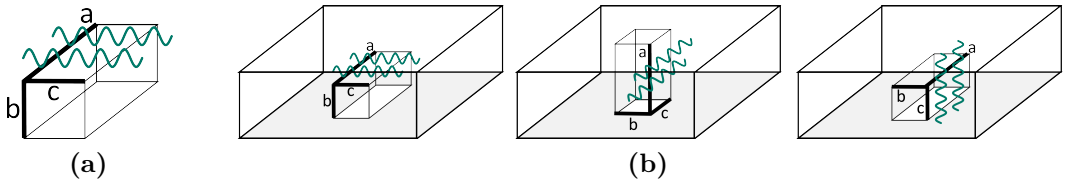

Figure 5.1: Scheme of the three uniplanar orientations in the co-crystalline phase and the δ phase. a) Two chains of syndiotactic polystyrene form a layer in the ac plane of the unit cell. b) Three different orientations of the unit cell and the layers inside the macroscopic polymer film (from left to right: $a\|$ $c\|$, $a\perp$ $c\|$, and $a\|$ $c\perp$). (Figure according to [Alb09b].)

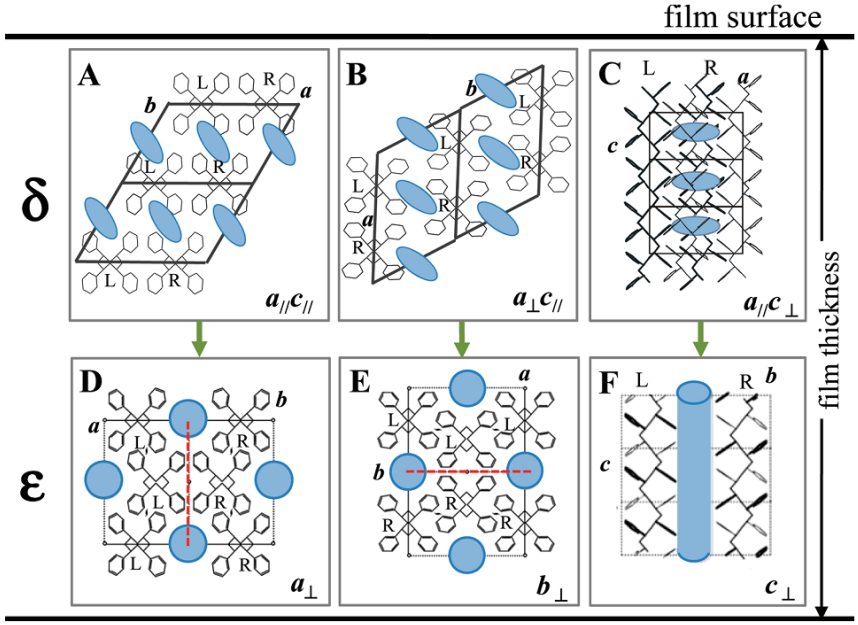

Figure 5.2: Different nanoporous crystalline phases of syndiotactic polystyrenewith channels (ε phase) and their corresponding predecessor phases consisting of nanocavities (δ phase). During film synthesis, another dense helical phase, the γ phase, is crossed between the two phases shown here. The thick horizontal lines depict the surfaces of the macroscopic polymer plane. (Figure taken from [Alb09b].)

5.1.1 δ Phase

The δ phase with a monoclinic unit cell (a=1.74 nm, b=1.185 nm, c=0.77 nm, and γ =117 °) has nanocavities with an empty volume of 0.12-0.15 nm^3 as isolated entities. Assuming, for simplicity, a nearly spherical cavity, the resulting diameter of the cavitity lies in the order of 600 pm. A xenon atom with a van der Waals radius of 216 pm should be able to fit into the nanocavity. However, according to [Mil09], the cavity of the δ phase features an oblonged, cylindrical shape with two different dimensions: the longer one nearly 8.1 Å, the much shorter nearly 3.4 Å.[1] According to these dimensions, an adsorped ^{129}Xe atom will strongly experience the boundaries of the cavities and its electron hull will be distorted according to the shape and size of the cavity. Thus, anisotropic peaks of the adsorbed ^{129}Xe are expected in the NMR spectra.
With larger guest molecules, the cavities can include guests up to a volume of 0.36 nm^3 by inducing changes in the crystal structure of the polymer. The unit cell of the δ phase includes two polymer chains per unit cell. In Figure 5.1 (a), the two polymer chains can be seen in context of the unit cell. The density of the δ phase is comparable to that of the nanochannel ε phase of 0.98 g/cm^3, and lower than that of amorphous syndiotactic polystyrene.

5.1.2 ε Phase

From the δ phase, it is possible to form another crystalline phase of syndiotactic polystyrene by thermal annealing. The resulting γ phase features also the helical structures of the polymer chains, but is dense and not porous. It can be used as the precursor structure to yet another porous crystalline phase, the orthorhombic ε phase (a=1.61 nm, b=2.18 nm, and c=0.79 nm). The cavities of the ε phase are connected and form nanochannels leading through the crystallites of the polymer film. The unit cell of the ε phase includes four polymer chains per unit cell. The density of the ε phase is with 0.98 g/cm^3 comparable to the density of the δ phase and a little lower than the density of normal (amorphous) polystyrene with 1.05 g/cm^3.

5.1.3 Unique uniaxial orientations in the polymer film

Orientation is a quite common phenomenon in polymers. A special property of the polymer system used here is the unique orientation of the crystalline phases with respect to the plane of the polymer film. For all semicrystalline polymer systems, a single axial orientation of the crystalline phases is relatively easy to obtain by aligning the polymer

1 These dimensions of the cavity have been calculated with a spherical probe with a radius $r = 1.8$ Å, for the slightly larger Xe atom $r = 2.2$ Å, the cavity may appear even more obstructed.

chains parallel to a stretching direction. Perpendicular orientation of the chain axis with respect to the film plane can not be obtained by common processing, but only by solution techniques and epitaxial growth in thin films. However, the polymer system used here exhibits up to three unique uniplanar orientations, i.e. films presenting one of the three orthogonal crystalline faces parallel to the film plane [Alb08a, Alb08c]. The different orientations are formed during co-crystallization with small molecular guests (e.g. chloroforme or trichloroethylene), but are retained after guest extraction. It is difficult to get a degree of orientation above 0.85 as well as a degree of cristallinity above 35 %, at least when considering metastable syndiotactic PS phases presenting chains in helical conformations. In its properties, syndiotactic polystyrene strongly resembles zeolite materials, with the advantage that the two nanoporous polymer phases can easily adapt their crystalline structure to different guests [Gue09b, Tar10a] and can be easily shaped into different macroscopic forms [Alb09b, Alb11c, Riz11b], getting rid of the laborious single crystal growth step. The disadvantage is the presence of an amorphous phase and a lower degree of orientation in comparison with zeolite materials.
For the co-crystalline phase and the δ phase exhibiting the nanocavities, the three uniplanar orientations are formed by three different orientations of layers of close-packed, enantiomorphous syndiotactic polystyrene helices. Figure 5.1 (a) shows the two polystyrene helices in the plane of the unit cell spanned by the a and the c axis of the cell. The orientation of the unit cell (and therefore the layers of polystyrene helices) inside the macroscopic film determines the orientation of the crystalline phases (see (b) in Figure 5.1). The three different orientations are named after the parallel or perpendicular orientation of the a and c axes in the plane of the polymer film, $a\| \; c\|$, $a\perp \; c\|$, and $a\| \; c\perp$.
Figure 5.2 shows the two nanoporous crystalline phases and all the different unique orientations of their cavities and channels with respect to the plane of the macroscopic polymer film. The upper row depicts the three different orientations of the δ phases described above, whereas the lower row depicts the three different orientations of the ε phase. Two of the modifications of the ε phase feature nanochannels parallel to the plane of the polymer film ($a\perp$ and $b\perp$), the third, $c\perp$, exhibits nano channels perpendicular to the outer macroscopic plane.
The anisotropy of the samples has provided the opportunity to perform vibrational analysis of syndiotactic polystyrene [Tor09] and to study the (re)orientational dynamics in dependence of guest molecules [Alb05, Alb09a, Alb11a, Alb11b]. In all these studies, strong anisotropy effects are always correlated to the δ phase. For the 'very' open channel structure of the ε phase, only small differences in the diffusivity and the orientation of guest molecules has been observed [Alb09b, Alb10].[1]
In this work, experiments on four different modifications of the nanoporous phases were

1 With the exception of molecules with very long chains, but these are very hard to incorporate in the nanoporous polymer.

performed: two modifications of the δ phase with the orientations $a\perp$ $c\parallel$ and $a\parallel$ $c\perp$, and the corresponding modifications of the ε phase with the orientations $b\perp$ and $c\perp$ have been used. An overview of all samples and the corresponding sample label can be found in Table 3.1 in Section 3.5.1.

5.2 Different phases of syndiotactic polystyrene probed by ^{129}Xe NMR spectroscopy

All NMR spectra of the polymer films were recorded with thermally polarized ^{129}Xe. Initial experiments with a continuous flow of hyperpolarized ^{129}Xe showed no signal of adsorbed xenon inside the materials. Regardless of the type of cavities in the polystyrene film (isolated cavities or channels), the diffusion of xenon atoms into the films seems to be very slow (especially when compared to the reported diffusion times of 200 ms for the diffusion of xenon into porous crystalline material in [Soz00]). Fortunately, the advantages of fast measurements and large signal enhancements due to hyperpolarization are not necessary for the characterization of static materials besides longer measurement times. The experimental details of the ^{129}Xe NMR measurements can be found in Sections 3.5.2 and 3.5.3.
Additionally to the numerous studies of ^{129}Xe in zeolite materials present in the literature (see Section 2.7), Sozzani et al. have presented ^{129}Xe NMR results on organic, porous crystalline materials, either in powder form [Soz00], or as a macroscopic crystal [Soz07]. Due to the nature of the organic crystals used in these studies, both samples showed a very high crystallinity and, for the single crystal, a very high degree of orientation. The macroscopic polymer films used in this work are far from the ideal state of a single crystal. They possess an amorphous part (around $^2/_3$ of the film) and the degree of orientation of the cavities and channels is imperfect (approx. 70-80 %, compare with Table 3.1). However, in spite of these imperfections, it is possible to gain knowledge of the inner structure of these polymer films and their anistropic nature by using ^{129}Xe NMR spectroscopy.

5.2.1 δ phase - Nanocavities

Figure 5.3 shows the ^{129}Xe NMR spectra for two samples of the δ phase in two different orientations as well as a sample of the amorphous, non-nanoporous α phase (for experimental details, see Section 3.5). The features observed in these three spectra are typical and similar for all ^{129}Xe NMR measurements on polymer films presented in this work. The spectra show two Xe peaks: The free Xe gas peak is narrow in comparison and is used as an internal reference set to 0 ppm in all spectra. The second peak is much broader for all samples. For the samples with nanocavities (Sample 02+03), the peak appears around 200 ppm (with different peak widths), whereas the peak from the amorphous sample is found above 200 ppm.
Each of the broad(er) peaks can be attributed to Xe adsorbed inside the polymer films. The width of the peaks varies greatly between the amorphous sample and the nanoporous samples. Due to the lack of any defined nanoporous structure inside the amorphous phase and thus the lack of any anisotropy, the amorphous sample features a much narrower peak. The anisotropy, which leads to the broadness and the shape of the peaks of the nanocavity samples, is caused by the size and shape of the cavities (as

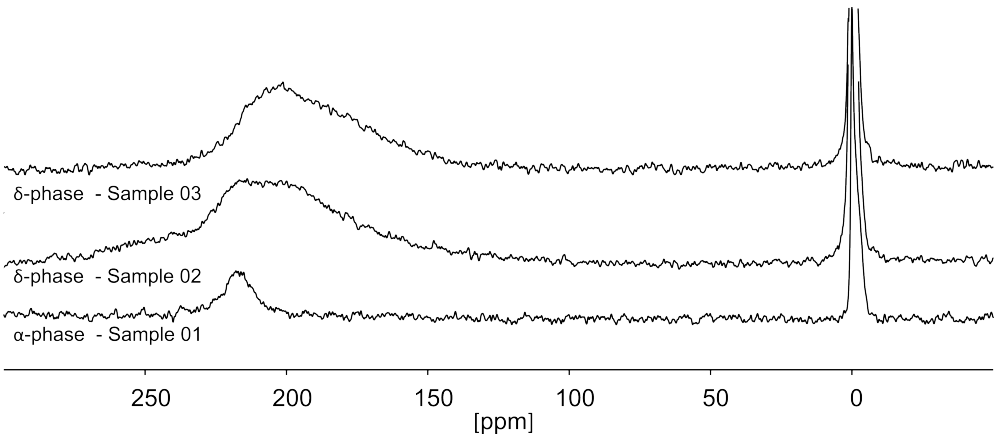

Figure 5.3: ^{129}Xe NMR spectra of the amorphous, non-nanoporous α phase (spectrum at the bottom) and two orientations of the δ phase (spectrum in the middle and at the top). Both δ phase samples consist of isolated nanocavities: Sample 02 (a $\parallel$ c $\perp$ orientation) and Sample 03 (a $\perp$ c $\parallel$ orientation).

predicted in Section 5.1.1) as well as by the orientation of the cavities with respect to the external magnetic field. Diffusion of Xe atoms between the separated cavities on the timescale of the NMR experiment is improbable. The observed anistropy is slightly higher for Sample 03, which also features a higher degree of orientation (compare Table 3.1).

Due to the broadness of the peaks of the adsorped Xe, the isotropic chemical shift of the peaks were determined by fitting the ^{129}Xe NMR spectra and determining the center of gravity of the peaks. Figure 5.4 shows the signal (red points), the fits of the peaks (blue line) as well as the chemical shift of the center of gravity (vertical black line), and a threshold value calculated from the signal-to-noise ratio from each sample and used in the determination of the center of gravity. The isotropic chemical shifts of all nanoporous samples (cavities and channels) are summarized in Table 5.1. The chemical shift of the center of gravity is 190.9 ppm for the $a\perp$ $c\parallel$ sample and 195.2 ppm for the $a\parallel$ $c\perp$ sample. For the amorphous α phase, the center of gravity appears at 217.6 ppm and is nearly 20 ppm higher than the highest value for the δ phase.

5.2.2 ε phase - Nanochannels

Figure 5.5 shows the ^{129}Xe NMR spectra of three samples of the ε phase: two samples with different orientations (Sample 04+05) as well as a sample of an unoriented ε phase,

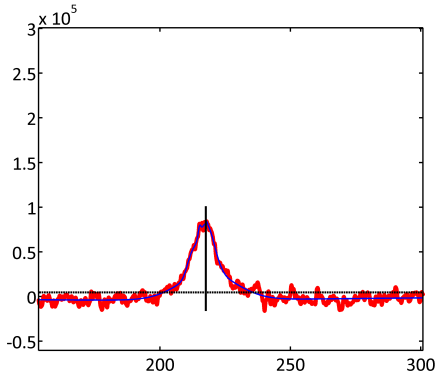

(a) Sample 01

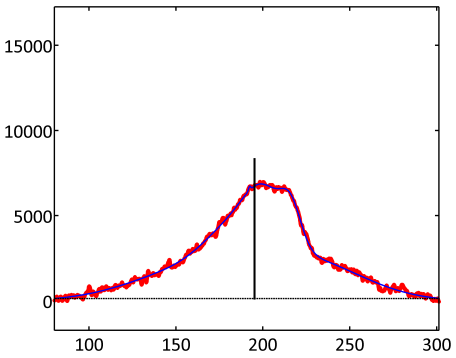

(b) Sample 02

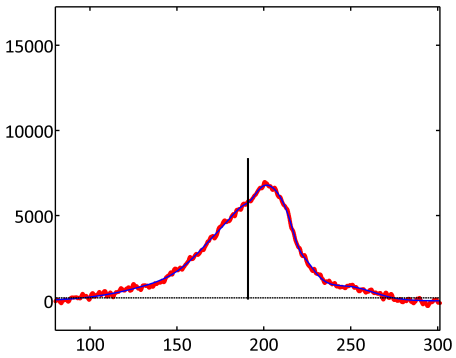

(c) Sample 03

Figure 5.4: Fits (blue line) of the NMR signal of xenon (red points) adsorbed in the α (Sample 01) and δ phase (Sample 02 and Sample 03). The center of gravity (vertical black line) and the threshold value (horizontal black, dotted line) used in the calculation for the center of gravity are shown.

Sample number	Phase and Orientation	Porosity	Center of Gravity [ppm]
01	α phase amorphous	non-porous	217.6
03	δ phase $a\perp$ $c\parallel$	cavities	190.9
02	δ phase $a\parallel$ $c\perp$	cavities	195.2
05	ε phase $b\perp$	channels	191.9
04	ε phase $c\perp$	channels	198.3

Table 5.1: Center of gravity for the film samples containing cavities and channels.

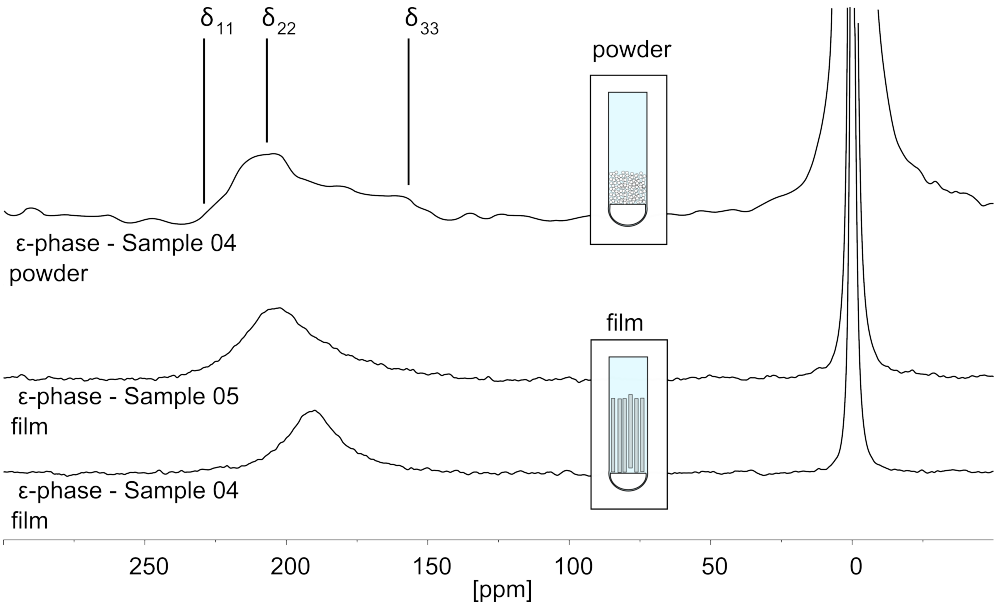

Figure 5.5: ^{129}Xe NMR spectra of two samples of two different orientations of the ε phase (Sample 04 (lower spectrum) and Sample 05 (middle spectrum)). The spectrum at the top is obtained from the powder of Sample 04. All ε phase samples consist of connected nanocavities or channels, but only the two films samples show an orientation of the channels (Sample 04 (b $\perp$ orientation) and Sample 05 (c $\perp$ orientation).

which has been obtained by grinding of Sample 04.[1] The peaks of the adsorbed ^{129}Xe in the oriented channels are significantly narrower than for the samples containing the nanocavities, whereas the chemical shift difference between the two orientations of the channels is larger (channels: 6.4 ppm vs. cavities 4.3 ppm).
According to the structure of the samples containing the channels, there should be two anistropy effects contributions: the first one is the influence of the channels and the anisotropic confinement of the ^{129}Xe atoms therein, and the second one is the influence of a prevalent orientation of the channels inside the polymer films and, thus, an orientation of the channels in the external magnetic field B_0.
The powder sample (upper spectrum in Figure 5.5) features the same channels as the two oriented samples (as it has been obtained from one of them), but due to the small size of the single particles in the powder sample, no prevalent orientation of the channels is present. The adsorbed ^{129}Xe experiences the confinement in the channels, but any contributions due to an orientation of the channels to the external magnetic field should

1 The use of Sample 10, which should also feature unoriented nanochannels, proved to be unsuccessful due to the 'aerogel' nature of the sample: The ^{129}Xe atoms experienced anistropy even outside the crystalline phases due to the abundance of pores and channels with different sizes in the material.

be averaged out by the random alignment of the channels.[1] The spectrum of the powder sample reflects the confinement by the presence of the large chemical shift anisotropy visible in the peak of the adsorbed ^{129}Xe. Although the SNR of the experiment is rather bad, the principal components of the chemical shift have been determined as $\delta_{11} = 230\,\text{ppm}$, $\delta_{22} = 206\,\text{ppm}$, and $\delta_{33} = 158\,\text{ppm}$. Following Sozzani et al. [Soz00], the shape of the anistropic peak reflects the dominance of interactions between Xe atoms in the channels compared to interactions between Xe atoms and the walls of the channels, i.e. the density of Xe atoms in the channel is high enough to counter the axial symmetry which is given by the channels. The shape of the electronic shell of the ^{129}Xe atoms in the channels is therefore oblate.

The signals, the fits, the centers of gravity, and the threshold values for the peaks of the adsorped ^{129}Xe can be found in the Appendix, see Section A.1.1. The chemical shift of the center of gravity has been determined as 191.9 ppm for the $b\perp$ sample and 198.3 ppm for the $c\perp$ sample.

For the first time, the strong anisotropy in the ε phase related to the presence of atomar or molecular hosts could be shown in these experiments. The measurement of a powder sample provided the opportunity to distinguish between the anisotropy caused by the orientation (see also the results concerning the macroscopic rotation of the films in Section 5.3) and the anisotropy from the confinement of the ^{129}Xe atoms inside the porous structures of the films.

1 Due to the film nature of the precursor of the powder sample, the grinding may have been imperfect, giving rise to a residual spatial orientation of slightly oblonged particles in the NMR tube.

5.2.3 Reproducibility - 'Old' vs. 'new' Nanochannel Samples

In order to check for the reproducibility of the ^{129}Xe NMR measurements, experiments with different samples of the same modification of polystyrene film were carried out. As described in 3.5.1, two batches of polymer film consisting of the same nanoporous modifications were available. Four samples of the nanochannel ε phase, two from each batch, could be compared.
Figure 5.6 shows the results of the ^{129}Xe NMR spectroscopy measurements. On the left side (a), the spectra for the samples of the 'old' batch are shown (sample 04 and 05), on the right side (b), the spectra for the samples of the 'new' batch (sample 11 and 12).
The position of the peaks of the two orientational modifications of the crystalline phases are comparable and their order is the same: The signal peak of the ε phase in $c\perp$ orientation (sample 04 and 11) is shifted to higher ppm-values compared to the signal peak of the ε phase in $b\perp$ orientation (sample 05 and 12).
But at the same time, distinct differences between the spectra of the different batches are visible, too. The signal, the fits, the center of gravity, and the threshold value for the samples of the 'new' batch of films with channels can be found in the Appendix, see Section A.1.2. The signal-to-noise ratio for the broad peaks of the adsorped xenon is much smaller for the 'new' films though the same Xe gas pressure and number of scans were used in the NMR experiments. The low signal-to-noise ratio can be seen especially with sample 12 in (b) in Figure A.2: The horizontal black line, depicting the threshold value below which the signal values were not considered in the calculation of the center of gravity, lies at nearly 10 % of the maximal signal amplitude. According to the known properties of the two batches (see Table 3.1 on page 47), the amount of crystalline phase and therefore the amount of nanochannels should be even slightly larger for the samples

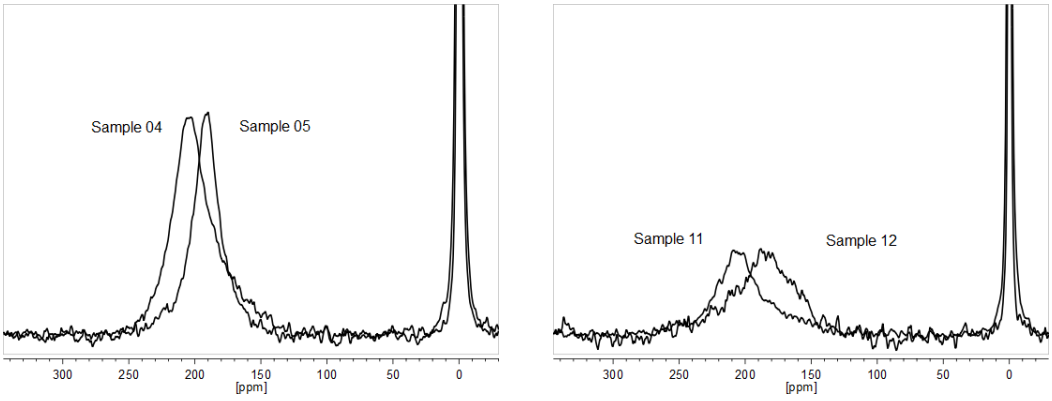

(a) Channels - OLD - Sample 04 05 **(b)** Channels - NEW - Sample 11 12

Figure 5.6: Comparison between 'old' and 'new' film samples with channels.

of the 'new' batch, but this could not be proven by the ^{129}Xe NMR experiments.
The peak shapes are similar for both samples of the ε phase in $c\perp$ orientation, but the peak of the 'new' sample of the ε phase in $b\perp$ orientation is broader than the peak of the 'old' sample (compare in Figures A.1 and A.2).
Table 5.2 lists the chemical shifts of the center gravity for all four samples. The chemical shift difference between the two orientational modifications of the crystalline phase does differ between the two sample batches: For the 'old' samples, the difference is 6.4 ppm while for the 'new' samples, the difference is more than twice as large with 14.8 ppm.
Assuming the correctness of the ^{129}Xe NMR results, the NMR results point towards quite substantial differences between different batches of the polymer films. These differences can probably be explained by the higher degree of orientation of the 'new' batch of the syndiotactic polystyrene films (0.75/0.65 for the 'old' films vs. 0.85/0.80 for the 'new' films (see Table 3.1)), already introduced during the complex film preparation process. . The higher degree of orientation leads to a larger influence of the orientation on the chemical shift of the adsorbed ^{129}Xe, which causes the larger Δ of the chemical shift between the two orientation of the channels for the 'new' films.

Sample number		Phase and Orientation	Porosity	Center of Gravity [ppm]
04	'old'	ε phase $c\perp$	channels	198.3
11	'new'	ε phase $c\perp$	channels	201.2
05	'old'	ε phase $b\perp$	channels	191.9
12	'new'	ε phase $b\perp$	channels	186.4

Table 5.2: Center of gravity for the film samples containing channels - 'old' vs. 'new'

5.3 Rotation of the film with respect to B_0

In these experiments, the (macroscopic) rotation of the semi-crystalline polymer film samples was used to verify the orientation of the porous structures inside the material. As described in Section 5.1.3, the syndiotactic polystyrene films consists of crystalline and amorphous parts. The crystalline parts are composed of a large number of small crystallites which share a preferred orientation with respect to the surface planes of the macroscopic films. Accordingly, any nanoporous structures inside the films, be it cavities or channels, show a certain orientation towards the film surface. As shown in Section 5.2, the resulting anisotropy leads to differences in the chemical shift of adsorped ^{129}Xe. The film samples with the nanochannels show an larger influence of the macroscopic film orientation, because adsorbed Xe atoms will show a higher degree of freedom along the channel axis compared to Xe atomes adsorbed in separated nanocavities (compare

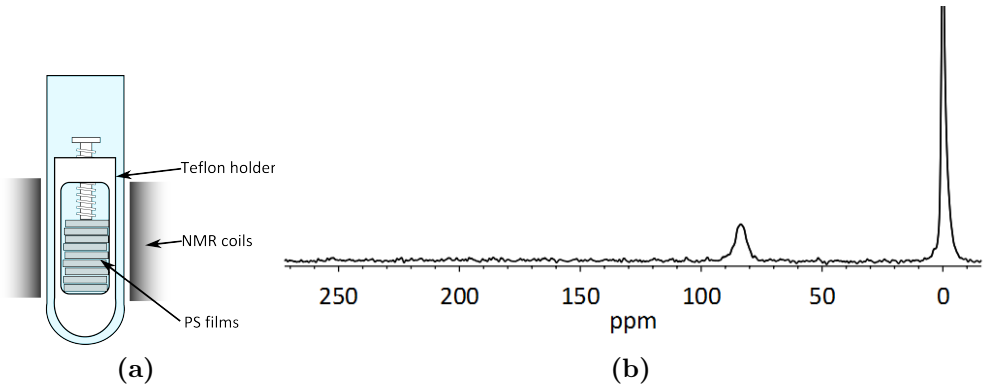

Figure 5.7: Schematic drawing of teflon sample holder (a) used to orientate the films inside the external magnetic field and the ^{129}Xe NMR spectrum obtained from Xe adsorbed in the sample holder. The peak arising from the sample holder (at 83 ppm) is outside the chemical shift range of ^{129}Xe adsorbed in the polystyrene films and does not interfere with any measurements.

Table 5.1).[1] Therefore, the channel samples are used in the experiments here. By rotating the polymer films inside the B_0 field between subsequent measurements, some of the different orientations should be easy to identify.
In order to orientate the films inside the NMR tube – and therefore in the magnetic field – a teflon sample holder is used, which is shown in Figure 5.7 (a). Since an amount of ^{129}Xe is also adsorbed in the material of the sample holder (teflon), Figure 5.1.3 (b) shows the corresponding ^{129}Xe NMR spectrum. Due to its position at around 83 ppm, it does not interfere with the peaks of ^{129}Xe adsorbed in the syndiotactic polystyrene films.
Figure 5.8 shows ^{129}Xe NMR spectra for Sample 04 and 05, both containing the oriented nanochannels. The difference for the two samples lies in the orientation of the channels with respect to the external magnetic field. The (idealized) orientations of the channels in the macroscopic polymer films and with respect to the external magnetic field is shown in Figure 5.8, too. For Sample 05, a rotation of the macroscopic film does not change the (perpendicular) orientation of the channels with respect to the external field, whereas a rotation of Sample 04 does change the channel orientation from parallel to perpendicular with respect to the external field. This difference is reflected in the chemical shift of the adsorbed ^{129}Xe. For Sample 05, practically no change in the chemical shift is observable (the small difference in the peak width can be explained by an imperfect orientation of the maroscopic film slices or by a slightly elliptical shape of the channels). In contrast,

1 Because the separated nanocavities in the δ phase do not feature a perfectly spherical shape, the same orientational effect is observed for these samples, but on a smaller scale.

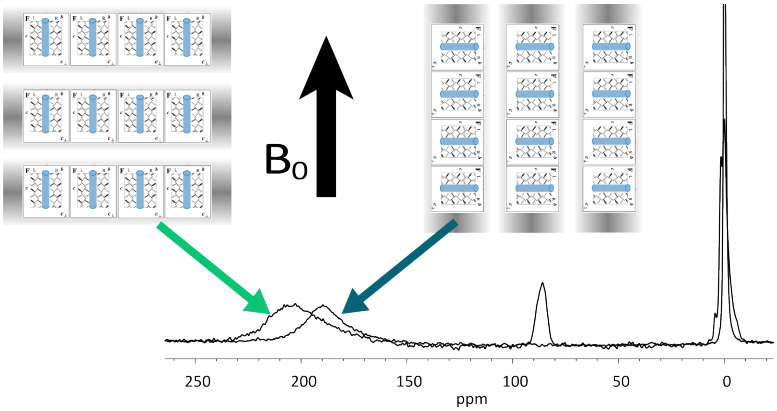

(a) Sample 04, film plane parallel and perpendicular to B_0

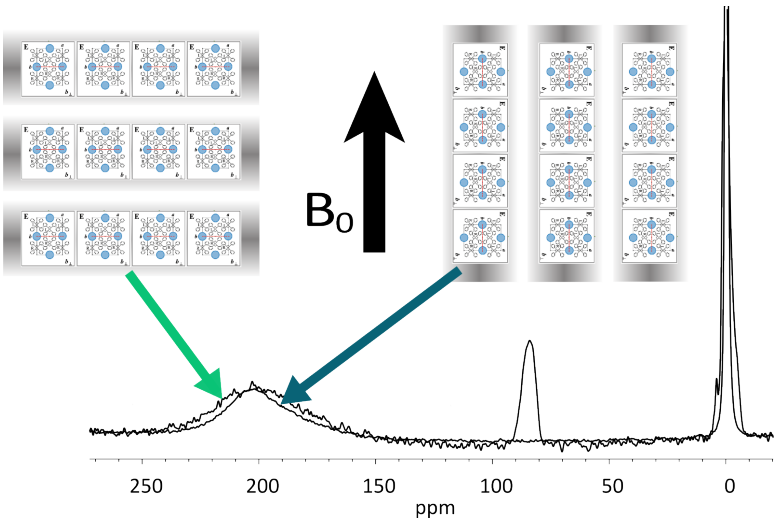

(b) Sample 05, film plane parallel and perpendicular to B_0

Figure 5.8: ^{129}Xe NMR spectra of Sample 04 (a) and 05 (b), containing the nanochannels, oriented with their film plane parallel and perpendicular to B_0. For each film and orientation, three schematic film slices are shown. The large black arrow depicts the direction of the external magnetic field, the light blue structures in the schematic film drawings show the orientation of the channels with respect to the external magnetic field. A difference in the chemical shift in dependence of the orientation can only be observed for Sample 04.

for Sample 04, a difference of 15 ppm in the chemical shift can be observed for the two orientations. By assuming relatively strong interactions of Xe atoms inside the channels (see also Section 5.4) and therefore a deshielding of the ^{129}Xe nucleus along the channel axis, the downfield shift for the peak of the channels parallel to the magnetic field can be explained.
The observed anisotropy and the dependence on the film orientation shown here is related to the upper spectrum of Figure 5.5. The two spectra here show two limiting cases of the orientation, whereas the powder spectrum of Sample 04 does include all possible orientations. The correlation is not perfect, since the anisotropy recorded for the powder spectrum is larger than for the two (limiting) orientations shown here. The difference may be explained by an imperfect orientation of the film slices in the experiments here or by an influence of interstitial cavities between the small powder particles, which behave as unoriented channels with a large size distribution.[1]

5.4 Temperature dependence of the chemical shift of ^{129}Xe in nanoporous polystyrene films

In order to influence the interactions of the Xe atoms inside the nanoporous structures of the polymer films, temperature-dependent measurements were performed (see Section 3.3 for the temperature control and Section 3.5 for the experimental details). Fig 5.9 (a) shows a series of ^{129}Xe NMR spectra of Sample 05 (containing oriented nanochannels) recorded at seven different temperatures between 240 and 303 K at different pressures (depending on the sample temperature). With the exception of the spectrum at 295 K, three peaks are visible. The peak at 0 ppm is the free ^{129}Xe inside the NMR tube and is used as reference. The peak just under 100 ppm is caused by the presence of the teflon sample holder inside the NMR tube (see Section 5.3) and can be neglected. As usual, the broad peaks between 150 and 250 ppm are assigned to the adsorbed ^{129}Xe in the polymer films. Figure 5.9 (b) shows the evolution of the isotropic chemical shifts of the adsorbed ^{129}Xe peaks as determined by the centers of gravity. A large increase of the chemical shift in dependence of the sample temperature is observed, from 189.2 ppm at 240 K to 208.8 ppm at 303 K. A jump-like increase between 250 and 260 K from 193 up to 205 ppm is distinct, the chemical shift does not change strongly anymore at higher temperatures.
By changing the temperature inside the NMR magnet, and therefore changing the temperature of the NMR containing the ^{129}Xe gas and the sample, several effects occur: First, a change in the amount of the adsorped ^{129}Xe is expected. At lower temperatures, the loading of the polymer films will be higher, although in the experiments conducted here, this effect could be subverted by the lowering of the gas pressure at

1 Such an effect could be observed, as noted above, for the 'aerogel' Sample 10.

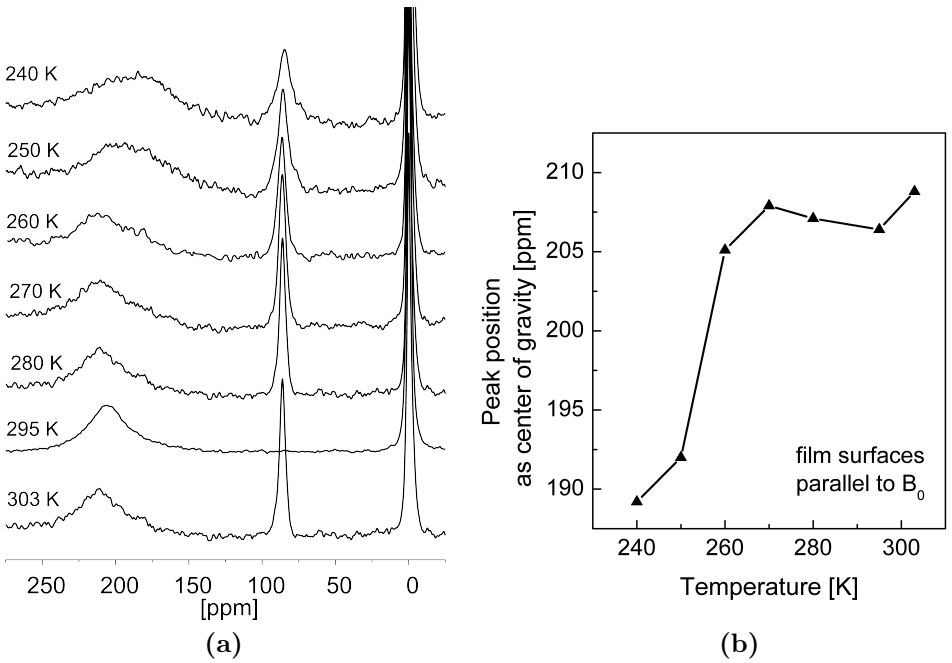

Figure 5.9: Series of ^{129}Xe NMR spectra of Sample 05 in dependence of the sample temparture (a) and the isotropic chemical shift (determined as the center of gravity) of the adsorbed ^{129}Xe versus the sample temperature. The peaks just below 100 ppm for temperatures other than 295 K are caused by the presence of the sample holder inside the NMR tube and can be neglected. The macroscopic film surfaces have been oriented parallel to the external magnetic field during these experiments.

lower temperatures. Figure 5.10 (a) shows the evolution of the gas pressure inside the NMR tube (neglecting any Xe adsorption). A second effect is the change in the free mean path λ of the gas atoms, which increases with lower pressures, and can be estimated by following equation:

$$\lambda = \frac{1}{\sqrt{2}\pi n d^2} \tag{5.1}$$

with the particle density $n = {}^{N}/_{V}$ and the diameter of the gas particles d. For the temperature and pressure range involved in the experiments here, the mean free path changes about 20 % from around 16 nm to 20 nm. Surely, any movement of ^{129}Xe atoms inside the channels is not comparable with the movement of a free gas atom, but a slight influence is expected, since the relative 'open' channel structure will allow some displacement of Xe atoms. Figure 5.10 (b) shows the evolution of the mean free path in dependence of the sample temperature (causing the change in the gas pressure). In summary, an increase in the interactions between Xe atoms is expected at lower temperatures.

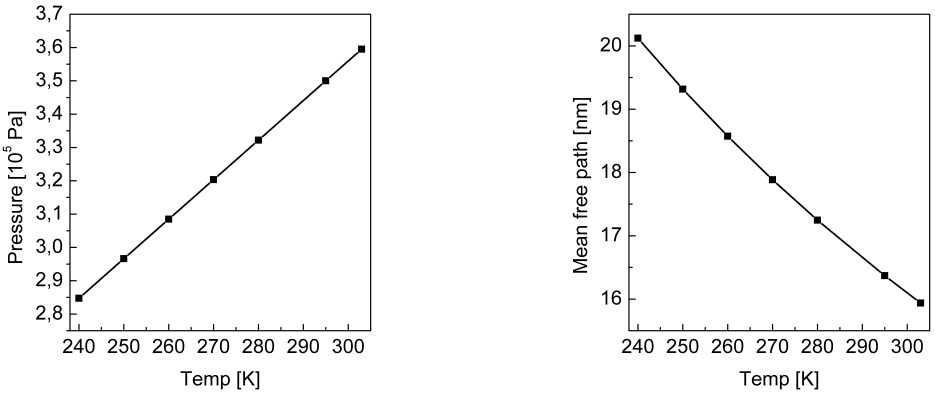

(a) **(b)**

Figure 5.10: Plot of gas pressure inside the NMR tube versus the sample temperature (a) and plot of the mean free path of a Xe atom versus the sample temperature (b). The NMR tube was initially filled with Xe gas at pressure of 3.5 bar at a temperature of 295 K. Due to the different experimental temperatures, the pressure and accordingly the free mean path of the gas atoms changed.

A third contribution, the change of the chemical shift of the free ^{129}Xe gas with respect to the temperature and pressure changes was neglected and the signal of the free ^{129}Xe gas was used as reference and set to 0 ppm for all measurements. In the used temperature range between 240 and 303 K and at the resulting pressures between 2.85 and 3.59 bar, no condensation of Xe gas takes places and thus the gas density (expressed in [amagat]) does not change in the sealed NMR tube (unless the amount of adsorped Xe gas inside the material in- or decreases drastically). According to [Jam92] and [Mün05], the change in the chemical shift for the free ^{129}Xe gas is smaller than 0.3 ppm between the lowest and the highest temperature (compare with the width of the free gas signal at half height of approx. 1 ppm).
As the channels present in the sample are oriented perpendicular to the external magnetic field B_0, the increase in the chemical shift can be explained by the expected increase of the interactions between ^{129}Xe atoms inside the channels at lower temperatures (similar to the perpendicular orientation in [Soz07]). The increasing interactions change the chemical shift tensor in the direction perpendicular to the magnetic field, causing the upfield shift with increasing temperatures. Using the anisotropy present in the syndiotactic polystyrene films, it is possible to draw conclusions about the behavior of the adsorbed ^{129}Xe atoms.

5.5 Conclusion

^{129}Xe NMR proved to be an excellent tool to characterize the anisotropic properties of nanoporous syndiotactic polystyrene films. The results showed a 'transfer of anisotropy' from the material to the gaseous NMR probe, i.e. ^{129}Xe, which has previously only been shown for crystal materials (zeolites or organic crystals). Here, ^{129}Xe NMR was successfully applied to a only semi-crytalline system whose inner structural orientation were far from perfect. Despite the use of this 'real-world' system, interesting results concerning the anisotropy of the polymer films were obtained.
For the two nanoporous phases, δ and ε phase, strong anisotropic effects towards atomar hosts in the system could be shown. This behavior was known for the δ phase from previous studies, but could be proven here for the ε system for the first time. Differences between batches of the polystyrene films, i.e. the degree of orientation inside the film, could be detected by ^{129}Xe NMR. By measuring a larger number of samples with differing degrees of orientation, it could be possible to interpolate to the chemical shift values of a perfectly oriented crystal phase in the future.
For the samples containing nanochannels, the dominance of interactions between Xe atoms in the channels compared to interactions between Xe atoms and the channel walls could be shown by measurements of a powder sample and experiments including the rotation of the films in the external magnetic field as well as temperature-dependent measurements. At the pressure used here, Xe atoms do interact with each other when adsorbed in the channels. At low temperatures, the interactions increase, probably due to a higher Xe loading of the polystyrene films.
As demonstrated here, ^{129}Xe NMR will be very useful to determine degrees of anisotropy even in far less than ideal systems in future applications.

6 Online Monitoring of Miniemulsion Polymerizations by ^{129}Xenon NMR spectroscopy

As described in Section 2.6, polymerization reactions are a very important and widely-used class of chemical reactions. Polymerization products are found everywhere in the modern life. Many chemical and physical properties of these polymers depend on the numerous parameters of the polymerization process. Adjusting the polymer properties can thus be achieved by tailoring the polymerization process [Mat07], improvements in the control of the polymerization reaction are very valuable. Online monitoring methods offer an efficient control of the reaction, which leads to products with constant quality at minimal costs [Gut10]. The most valuable monitoring methods work without the need of sample extraction which ideally allows for the constant and direct process control. Common techniques to monitor industrial polymerization reactions are reaction calorimetry, optical spectroscopy methods like IR or Raman spectroscopy, and process gas chromatography [Fon09, Fra10]. The widely used calorimetric measurements are suitable for immediate reaction control, but only for exo- or endothermic reactions (the large majority of polymerization reactions are exothermic).
NMR spectroscopy is another useful tool for online monitoring of polymerization reactions, providing valuable information about the composition of the reaction mixture [Had00, Gra05, Abd07]. It has been shown that online NMR spectroscopy for monitoring polymerizations can provide an acceptable time resolution using ^{1}H NMR and ^{13}C NMR [Gut10, Lan98]. However, the intrinsic low sensitivity of NMR measurements and the need of time consuming signal averaging often lead to problems in achieving this, which is especially true for ^{13}C at natural abundance limiting the achievable time resolution to a few minutes. Isotopic enrichment of ^{13}C would help to overcome this problem but is much too costly. Moreover, ^{1}H NMR mostly requires the use of expensive deuterated solvents hampering its application for industrial processes.
As described in Section 2.3, several so-called hyperpolarization methods can overcome the lack of sensitivity of NMR spectroscopy allowing for an excellent time resolution in dynamic measurements. In this work, hyperpolarization of the noble gas ^{129}Xe via SEOP (described in Section 2.4) was applied using the apparatus described in Section 3.1. The signal enhancement in NMR spectroscopy due to the hyperpolarization of ^{129}Xe offers the possibility of fast measurements and the online monitoring of dynamic processes [Kil04, Han04, Sch09]. Furthermore, one can take advantage of two other properties of the ^{129}Xe nucleus: Firstly, the large polarizability of the xenon electron cloud by its physical and chemical environment leads to a large chemical shift range of ^{129}Xe NMR.

This sensitivity allows for reporting of sample properties by the chemical shift of the Xe atom without the need of covalent bonding between the Xe atom and the sample molecules. Many examples of gaseous ^{129}Xe NMR exploiting this effect can be found in the material science of porous media (see Sections 2.2 and 2.7). Another useful property of Xe is its solubility in liquid phases, both organic and aqueous, which allows for the use of ^{129}Xe in liquid reaction mixtures.

In this contribution, the real-time monitoring of a free radical polymerization of styrene in a miniemulsion is demonstrated, using a continuous flow of hyperpolarized ^{129}Xe through the reaction mixture. The polymerization techniques of emulsion and miniemulsion polymerization are described in Section 2.6. A short description of the monitoring of a batch polymerization of methyl methacrylate at 35 G was given by Gloeggler et al. [Glo11]. However, the current work gives the first full length report demonstrating that hyperpolarized ^{129}Xe can be used for online monitoring of a polymerization reaction (published in [Due12]). By combining all properties of hyperpolarized ^{129}Xe as described above, it is used here as an NMR probe in a polymerization reaction of an industrially important monomer in the complex environment of a miniemulsion. The absence of xenon from common chemical substances leads to the absence of any undesired background signal rendering the interpretation of the sparse Xe spectra very convenient. In this work, only two distinct peaks of xenon inside the reaction mixture are recorded (Section 6.1). The resulting simple NMR spectra can be analyzed in a very straightforward manner by the determination of the chemical shift of the ^{129}Xe peaks giving access to the conversion of the polymerization (Section 6.2). Therefore, the kinetics of two polymerization reactions were recorded by hyperpolarized ^{129}Xe NMR spectroscopy using two oil-soluble azo-initiators with different decomposition temperatures (Section 6.4).

In order to prove the validity of the method, the progress of the polymerization reaction observed by ^{129}Xe NMR was compared to results obtained by calorimetry. Calorimetric measurements on similar emulsion and miniemulsion systems can also be found in the literature [Bec00, Li06, Bly99, Tar10b]. To allow for better comparison and to exclude any time-dependent changes of the miniemulsion, small samples of the same batch of miniemulsion were measured simultaneously by ^{129}Xe NMR spectroscopy and calorimetry (Section 6.5). Thereafter, the conversion of the different samples and reactions were determined by measuring the solids content. To check for differences between the polymer colloids obtained from the individual reactions monitored by NMR and calorimetry, the mean particle diameters were measured by PCCS and scanning electron micrographs.

A possible influence of the particle size in a (polystyrene) polymer dispersion on the chemical shift of ^{129}Xe, which could represent a complicating factor for the online monitoring in emulsions and dispersions, is excluded (see Section 6.3). Finally, the online monitoring of another type of reaction in a miniemulsion, an enzymatic esterification, by ^{129}Xe NMR spectroscopy is presented. The results illustrate a limitation of the reaction monitoring method by ^{129}Xe NMR.

6.1 ^{129}Xe NMR in Miniemulsions

To record typical spectra of ^{129}Xe in a miniemulsion, samples with water and styrene as the main components were prepared as described in Section 3.6.2 and hyperpolarized ^{129}Xe was dissolved in these miniemulsions using the setup described in Section 3.6.1. Figure 6.1 shows representative NMR spectra of ^{129}Xe atoms dissolved in the miniemulsion after the cold sample was introduced in the spectrometer and heated to the temperature of the polymerization. Three distinct peaks can be observed corresponding to Xe in different physical and chemical environments. The peak of free Xe gas inside the hollow-fiber membranes has the lowest chemical shift and can be used as an internal reference (0 ppm). The Xe atoms dissolved in the different phases (aqueous and organic) of the miniemulsion give rise to the peaks at 186 and 192 ppm, respectively.
In case of a relatively slow exchange of the xenon atoms between the continuous aqueous phase and the discontinuous organic phase, as it is the case for room temperature and below, two distinct peaks can be observed in the NMR spectra (lower spectra in Figure 6.1). Heating the sample to 343 K (temperature of the polymerization) results in higher exchange rates and the two distinct peaks start to merge until only one exchange peak is visible (upper spectra in Figure 6.1, this process is also visible in the spectra of the first 15 min in Figure 6.6, see below).

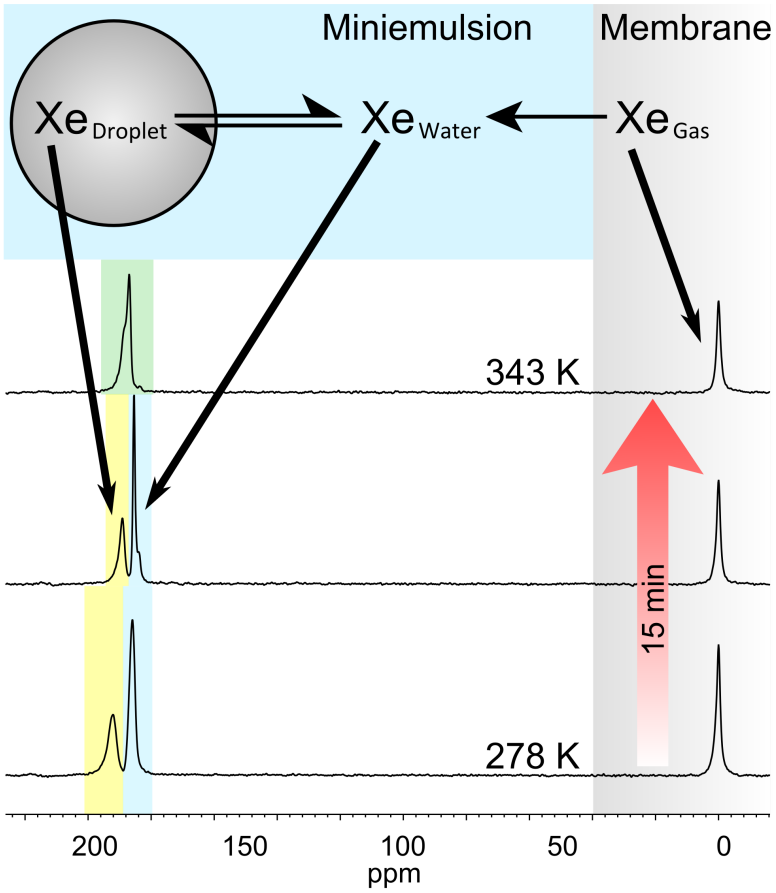

Figure 6.1: NMR spectra of hyperpolarized ^{129}Xe dissolved in the miniemulsion. According to the number of phases, up to three Xe peaks are observable. The right peak in the spectra corresponds to the free Xe gas located in the hollow fiber membranes, whereas the middle and the left peak correspond to Xe dissolved in the aqueous (blue background) and organic (yellow) environment, respectively. The cold sample (278 K) was heated during the first minutes in the NMR spectrometer to 343 K giving rise to a faster exchange of the Xe atoms between the organic and aqueous phase and the appearance of an exchange peak (green).

6.2 Dependence of the chemical shift on the monomer/ polymer ratio

In order to easily monitor polymerization reactions by ^{129}Xe NMR spectroscopy, a (preferably linear) dependence of the chemical shift of the dissolved ^{129}Xe on the conversion of the polymerization should exist.
In miniemulsion polymerizations however, four contributions to the chemical shift of dissolved Xe must be considered (see Figure 6.2):

First, there are the interactions between ^{129}Xe atoms and H_2O molecules of the continuous phase whose contribution to the total chemical shift can be considered constant during the reaction because the amount of water in the system does not change substantially. Second, interactions exist between the dissolved ^{129}Xe atoms themselves, but the contribution is very small due to the very low Xe density in these experiments (only 1% of Xe in the gas mixture) and can be neglected. Furthermore, there are two chemical shift contributions in the organic phase of the miniemulsion stemming from the interactions between the ^{129}Xe atoms and the monomer and polymer molecules, respectively. The first contribution is decreasing during the reaction as the amount of the monomer molecules is depleting, the latter contribution is increasing during the reaction as the polymerization degree increases. By taking into account all described contributions, the behavior of the chemical shift can be calculated by the following equation [Buc56, Jam73, Jam92]:

$$\begin{aligned}\delta_{dissolved\,Xe} = &-\sigma_0^{Xe-mono}(T)\cdot[mono](T) - \sigma_0^{Xe-poly}(T)\cdot[poly](T)\\ &-\sigma_1^{Xe-H_2O}(T)\cdot[H_2O](T) - \sigma_0^{Xe-Xe}(T)\cdot[Xe](T)\,.\end{aligned} \tag{6.1}$$

$\delta_{dissolved\,Xe}$ is the resulting chemical shift of ^{129}Xe dissolved in the miniemulsion. The constants $\sigma_0^{Xe-mono}$, $\sigma_0^{Xe-poly}$, $\sigma_0^{Xe-H_2O}$, and σ_1^{Xe-Xe} are the shielding contributions due to interactions of Xe with the monomer, the polymer, the water of the aqueous phase, and itself, respectively. The terms $[mono]$, $[poly]$, $[H_2O]$, and $[Xe]$ depict the amount of monomer, polymer, water and xenon in the miniemulsion, and T is the temperature.

By omitting the Xe-Xe interactions as described above and assuming the Xe-H_2O interactions and the temperature constant, the equation simplifies to:

$$\delta_{dissolved\,Xe} = -\sigma_0^{Xe-mono}\cdot[mono] - \sigma_0^{Xe-poly}\cdot[poly] - const. \tag{6.2}$$

By using $[poly] = 1 - [mono]$, the equation can be further simplified, giving the following linear dependence on the mole fraction of the monomer $[mono]$:

$$\delta_{dissolved\,Xe} = \left(\sigma_0^{Xe-poly} - \sigma_0^{Xe-mono}\right)\cdot[mono] - \sigma_0^{Xe-poly} - const. \tag{6.3}$$

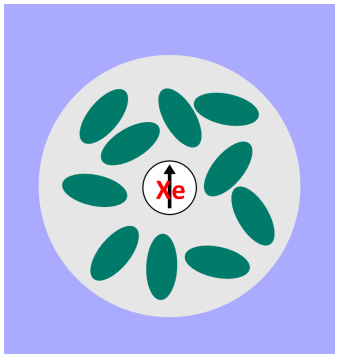

(a) Xenon - Monomer

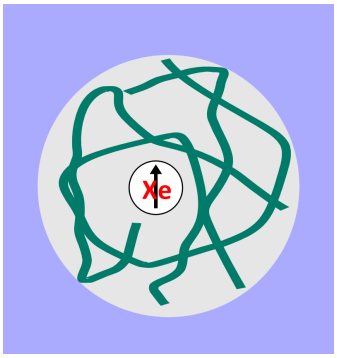

(b) Xenon - Polymer

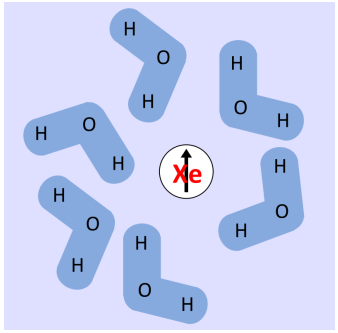

(c) Xenon - Water

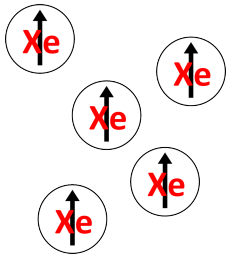

(d) Xenon - Xenon

Figure 6.2: Four different contributions to the interactions of ^{129}Xe dissolved in the miniemulsion of a miniemulsion polymerization reaction. The contributions of the Xe-Monomer (a) and Xe-Polymer interactions will change during the polymerization reaction, whereas the contributions of the Xe-Water (c) and Xe-Xe interactions (d) will stay constant.

In order to check for the linear dependence of the chemical shift on the monomer concentration, the chemical shifts of ^{129}Xe in pure styrene and pure polystyrene (M_w = 100,000 g $\cdot$ mol^{-1}) as well as in nine mixtures of styrene and polystyrene with increasing monomer to polymer ratios were determined. The preparation of the monomer-polymer mixtures and the experimental details are described in Section 3.6.3.

In Figure 6.3, the chemical shift of dissolved ^{129}Xe is plotted versus the mole fraction of the polymer and the mole fraction of the monomer in the mixture, respectively. A linear dependence of the chemical shift on the sample composition is clearly observed. The values were fit linearly, yielding the following relationship between chemical shift and the mole fraction of the monomer $[mono]$:

$$\delta_{Xe\,in\,mix} = -27.6\,\text{ppm} \cdot [mono] + 224.8\,[ppm] \tag{6.4}$$

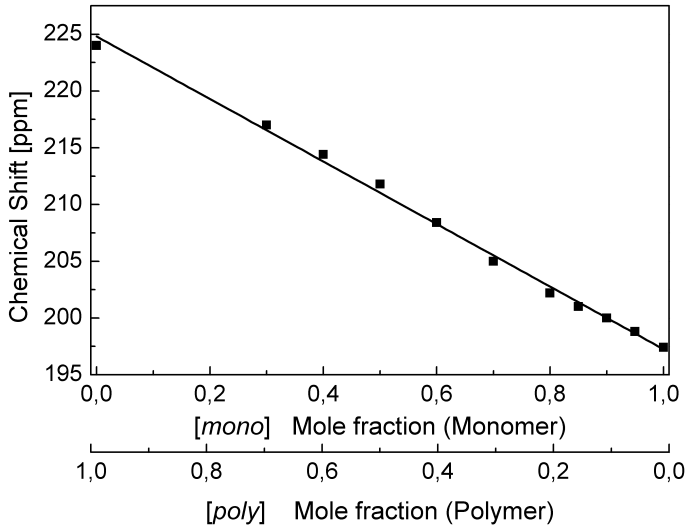

Figure 6.3: Plot of the chemical shift of ^{129}Xe versus the mole fraction of a monomer/polymer mixture. The black squares are the chemical shift values of pure polystyrene (M_w = 100,000 g · mol^{-1}), nine mixtures of styrene and polystyrene with decreasing polymer ratio, and pure styrene. A linear fit of the data points is shown as a solid line.

In this work, the studied polymerization reactions took place in a miniemulsion, a heterophase system, which is not only consisting of the mixture of styrene and polystyrene but also of water. Thus, the fit values based on Equation 6.4 cannot be used to directly determine the conversion of the reaction mixture in the following dynamic experiments (Section 6.4), because of the contribution of the aqueous phase to the chemicals shift in miniemulsions. However, it will be demonstrated in the following that the underlying dependence of the chemical shift shown above is just as well applicable to the monitoring of complex systems like miniemulsion polymerization reactions.

6.3 Dependence of the chemical shift on the particle size in a polymer dispersion

When using ^{129}Xe NMR to investigate polymer dispersions and emulsions as done here, an influence of the size of the polymer particles is conceivable. Polystyrene particles with particle diameters between 100 and 1000 nm are obtainable by (surfactant-free) emulsion polymerization reactions or by miniemulsion polymerization reactions as described in Section 2.6.2 and used here in the online-monitoring experiments presented in Section 6.4. The ratio of surface-to-volume changes drastically going from particle diameters of 100 nm to particle diameters of 1,000 nm: The larger particles feature a tenfold lower

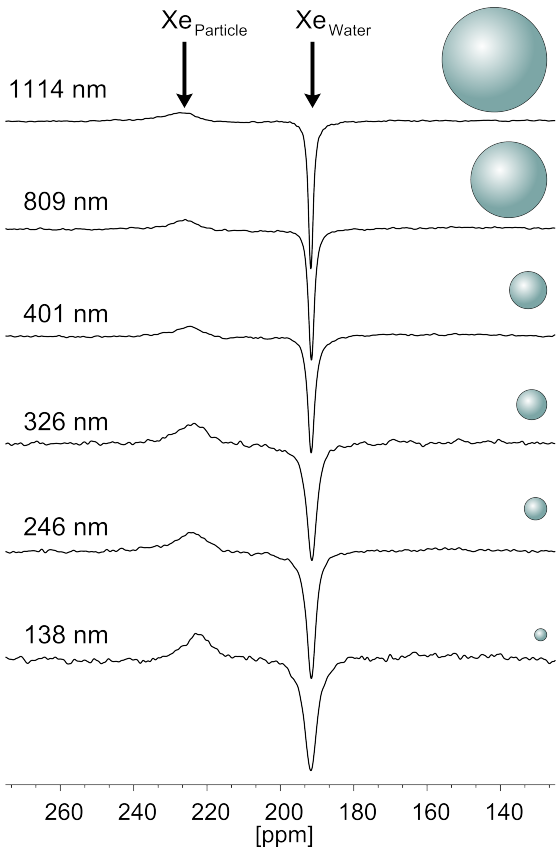

Figure 6.4: Series of NMR spectra of ^{129}Xe dissolved in polystyrene particle dispersions with particle diameters ranging from 138 to 1114 nm. All spectra were recorded at room temperature. A continuous flow of hyperpolarized ^{129}Xe was dissolved by use of the hollow-fibre membranes, equal to the experiments monitoring the miniemulsion polymerization reactions. The green spheres at the right side represent the different sizes of the polymer particles and are to scale.

surface-to-volume ratio.

During NMR measurements of hyperpolarized ^{129}Xe on polymer particle dispersions, the hyperpolarized xenon atoms are dissolved in the continuous, liquid (aqueous) and the discontinuous, solid (polymer) phase. In simple terms, the solid polymer phase consists of two parts: the bulk of the material inside the polymerparticle and the (probably very) thin surface area surrounding the particle and forming the interface to the continuous, aqueous phase. The ^{129}Xe atoms which are in the bulk region of the polymer particle do not experience any influence of the surrounding continuous phase, whereas an influence on atoms in the surface region could be possible.

Figure 6.4 shows a series of ^{129}Xe NMR spectra of six polystyrene particle dispersions with different diameters ranging from 138 to 1114 nm at room temperature T =295 K.

Particle diameter [nm]	^{129}Xe Chemical Shift [ppm]
138	223.5
246	224.1
326	223.8
401	224.8
809	225.3
1114	226.0

Table 6.1: Chemical shift of ^{129}Xe dissolved in dispersed polymer particles with different diameters.

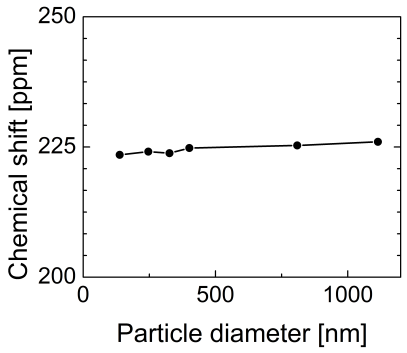

Figure 6.5: Chemical shift ^{129}Xe plotted against the particle diameter of the polymer particles.

The peak of the free ^{129}Xe gas inside the membranes is not shown, but has been used as reference and set to δ_{gas} =0 ppm. Two other peaks occur, both stemming from the dissolved ^{129}Xe in the particle dispersion (similar to the spectra of Figure 6.1). The peak at 192 ppm is attributed to ^{129}Xe dissolved in the aqueous phase and the broader peak around 224 ppm is attributed to ^{129}Xe dissolved in the polymer phase. The exchange between the two phases is slow at these temperatures and therefore Table 6.1 lists the chemical shifts of the polymer peaks of the dissolved ^{129}Xe. The values vary between 223.5 and 226 ppm and show only a slight trend to higher chemical shift values for larger particles. A small influence of the larger surface-to-volume ratio for smaller particles seems to be observable: When a ^{129}Xe atom is located in the surfacial area (or volume) of a polystyrene particle, its chemical shift is still influenced by the surrounding aqueous environment. (As noted above, the chemical shift of ^{129}Xe in water is approx. 192 ppm.) For the larger particles, the relative number of ^{129}Xe which are located in the surfacial volume decreases and the effective chemical shift reported from these particles is up to 2 ppm higher.
Overall, the effect of different particle diameters seems to be small and surely is negligible when monitoring the miniemulsion polymerization reactions presented in the following sections. The particle diameters of these miniemulsion polymerization reaction are well defined during the preparation of the miniemulsion and are narrowly distributed around the average value (between around 70 and 100 nm, compare with Table 6.2).

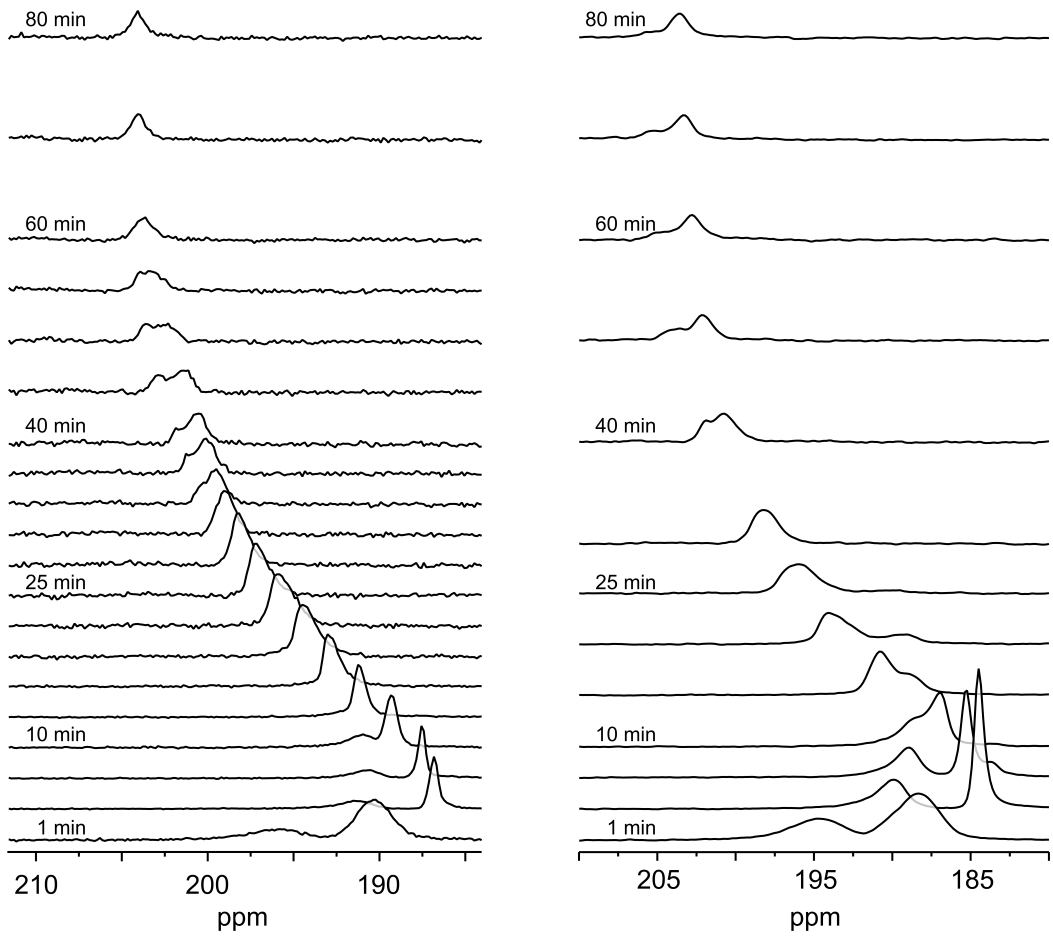

(a) Fast polymerization reaction (initiated by V59).

(b) Slow polymerization reaction (initiated by V70).

Figure 6.6: Two time series of ^{129}Xenon NMR spectra recorded during two miniemulsion polymerization reactions at 343 K. The plots show the chemical shift range of the dissolved Xe. The insertion of the sample tube into the heated magnet was used as the starting time $t = 0$ min. The spectra depict a strong dependence of the Xe chemical shift on the progress of the polymerization.

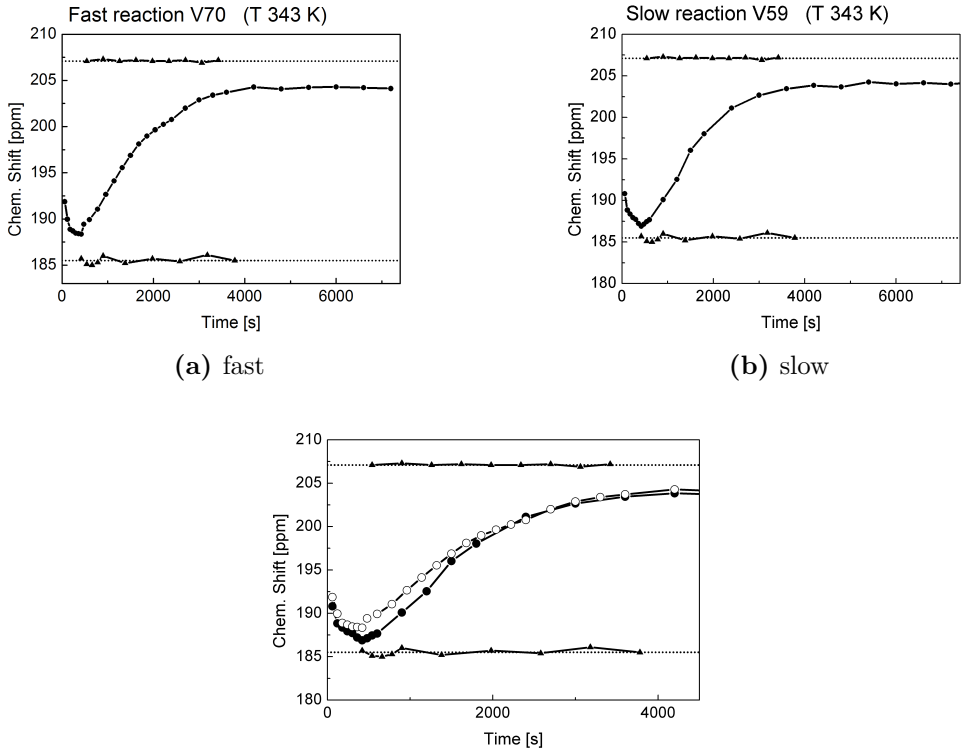

(a) fast **(b)** slow

(c) both

Figure 6.7: Plot of the chemical shift of ^{129}Xe versus reaction time with V70 as initiator (plot (a) and open circles in (c)), resulting in a faster increase in chemical shift, and V59 as initiator (plot (b) and filled circles in (c)), resulting in a slower increase. The triangles in all plots correspond to the Xe chemical shift in a fully polymerized colloid of the same particle size (207.0 ppm) and a miniemulsion containing only monomer droplets (185.5 ppm) at 343 K. The lines are for guiding the eyes.

6.4 Polymerization reactions in Miniemulsions

Two series of ^{129}Xe NMR spectra recorded during two different miniemulsion polymerizations of styrene are presented in Figure 6.6. The preparation and the experimental details of the ^{129}Xe NMR measurements are described in Section 3.6.2. For each series of spectra, the plots show a zoomed region containing the peaks of the hyperpolarized ^{129}Xe dissolved in the reaction mixture in the range of 186 to 205 ppm and 184 and 204 ppm, respectively. For the sake of visibility, not all recorded spectra from the start to the end of the reaction are depicted in these series of spectra. During the course of the polymerization, a clear shift of the ^{129}Xe peaks to higher chemical shift values is observed. Thus, the progress of the reaction is directly observable from the evolution of

the ^{129}Xe NMR signal. In the beginning, a temperature effect is visible as the xenon peaks move to smaller chemical shift values (compare first and second spectra for both series in Fig. 6.6). This shift is attributed to the heating of the samples from 278 K to 343 K. In the first spectra the heating effect counters and partially compensates the effect of the starting polymerization reaction, which simultaneously causes an increase in chemical shift. The resulting "equilibration time" due to heating is in fact comparable with the time which is needed for the heating of the sample in the calorimeter used in these studies (see below). Figure 6.6 shows also the merging of the two ^{129}Xe peaks mentioned already in Section 6.1 stemming from the aqueous and the organic phase of the miniemulsions to only one exchange peak due to changes in the exchange rate in the course of the experiment (compare spectra before and after 15 min in Fig. 6.1). The exchange rate increases as the temperature inside the sample increases. However, substantial broadening and distortion of the dissolved ^{129}Xe peak occurs between 30 and 60 min reaction time. The line broadening can be attributed to an increase of viscosity inside the monomer/polymer droplets which leads to a decreased mobility of the Xe atoms and the polymer chains. The decreased mobility cause a rise of dipolar interactions between Xe atoms and protons resulting in a net dipolar broadening of the ^{129}Xe NMR lines [Ken91, Sau96].

In this study, time-resolved spectra for two different polymerization reactions for a reaction time of 120 min were obtained by using two different azo-initiators, namely 2,2'-azobis(2-methylbutyronitrile) (commercial name V59) and 2,2'-azobis(4-methoxy-2,4-dimethyl valeronitrile) (commercial name V70) (chemical structure and the 10 h half-life decomposition temperatures are denoted in the Experimental section). At the reaction temperature of 343 K, polymerization reactions started by the two initiators follow the expected miniemulsion mechanism described by Bechthold et al. [Bec00] (see also below). However, the two initiators used here decompose at very different rates at 343 K. The very fast decomposition of V70 compared to V59 leads to a shorter nucleation phase and a faster on/off mechanism for the polymerization reaction initiated by V70 resulting in a higher reaction rate at the beginning of the polymerization. The faster on/off mechanism leads to shorter polymer chains compared to the reaction initiated by V59 (for SEC results, see below). The different molecular weights of the polymer suspensions allow us to the check for a dependence of the chemical shift of ^{129}Xe on the molecular weight of the polymers. A more detailed mechanistic insight into the two reactions from calorimetric data and the molecular weight distributions can be found below.

For both polymerization reactions, the chemical shift of the dissolved ^{129}Xe was determined for each spectrum of the time series and plotted in Figure 6.7. The open and filled circles in Plot (c) of Figure 6.7 show the development of the chemical shift of the dissolved ^{129}Xe for the reaction initiated by V70 and V59, respectively. As expected due to the shorter nucleation phase, the chemical shift of the dissolved Xe in the reaction started with the initiator V70 shows a faster increase than the one obtained in the reaction employing the initiator V59. For longer reaction times, the chemical

shift values of both reactions become the same due to the complete conversion of both polymerizations. Accordingly, the difference in the molecular weights of the products of the two polymerizations does not influence the chemical shift of ^{129}Xe in our experiments. For comparison all plots in Figure 6.7 also shows the two extremes for the chemical shift of the dissolved ^{129}Xe in theses polymerizations (triangles). The lower limit at 185.5 ppm represents ^{129}Xe dissolved in a miniemulsion at a temperature of 343 K containing only monomer, no polymer. It has been determined using a miniemulsion consisting of all reaction components except the initiator. Due to the lack of the initiator, no reaction could take place in the sample. The curve of the chemical shift of the reaction mixture nearly reaches the lower boundary (counteraction between thermal effect and shift due to the ongoing reaction). The upper limit at 207.0 ppm is given by the chemical shift of dissolved Xe in a completely polymerized miniemulsion at a temperature of 343 K. It was measured by using a colloidal polymer suspension of the same particle size as in the miniemulsions. During the monitored polymerization reactions, the chemical shift values do not reach this boundary, but stay approximately 3 ppm lower. This chemical shift difference can be attributed to the manufacturing of the colloid particles. The particles have been subjected to a dialysis process which removes any residual monomer, surfactant and charged, soluble oligomers from the system. Thus, the colloid particles obtained in this manner differ from the in-situ particles in the reaction mixture, giving rise to the observed difference in chemical shift.

6.5 Comparison between Calorimetry and ^{129}Xe NMR

To check the validity of the ^{129}Xe NMR monitoring method presented here, calorimetric measurements of the polymerization reactions were also carried out for polymerization reactions with the two initiators. In order to allow for a good comparison between the results obtained from calorimetry and ^{129}Xe NMR spectroscopy, two samples from the same miniemulsion batch were simultaneously measured by the two methods for each polymerization reaction. Thus, any change of the miniemulsion or any polymerization reaction prior to the start of the experiment can be ruled out for the interpretation of the differences between ^{129}Xe NMR and calorimetry.
The effect measured by a calorimeter is the heat flow in dependence of time which directly correlates with the reaction kinetics of the observed reaction. Thus, reaction heat calorimetry is a differential method. The chemical shift data measured by the NMR experiments depend on the polymerization degree or reaction conversion. Therefore, NMR reaction monitoring is an integral method. To compare the data from the two methods, the calorimetric data were numerically integrated.
Figure 6.8 shows the integrated calorimetric data (red line) and the corresponding ^{129}Xe NMR data (black circles) for both polymerization reactions. For the calorimetric data, the point of zero conversion was chosen as the time from which the reaction heat

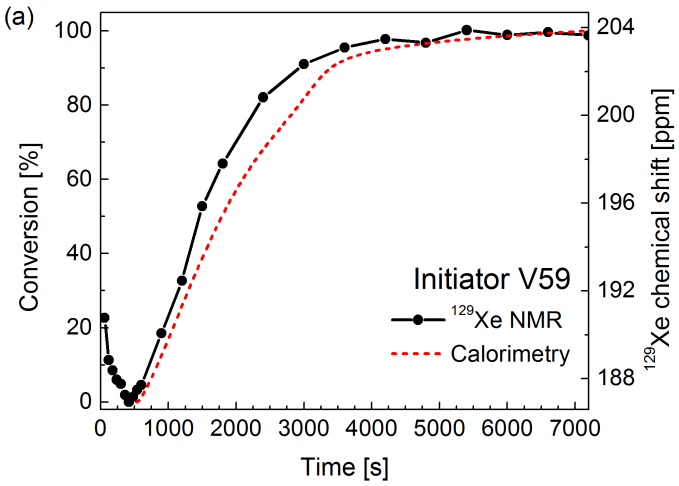

(a) V59

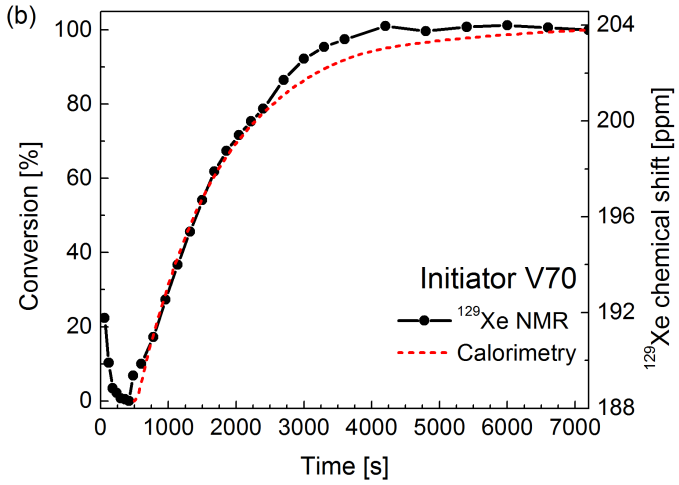

(b) V70

Figure 6.8: Comparison between the (integrated) calorimetry data (red dotted line) and the ^{129}Xe NMR data (solid line with filled circles showing the measured chemical shift) for the polymerization initiated by V59 (a) and V70 (b). The left y-axis shows the conversion, the right y-axis shows the corresponding ^{129}Xe chemical shift values.

becomes exothermic (the first point of the positive slope, at $t = 500\,\mathrm{s}$). Comparably, the lowest chemical shift values derived from the ^{129}Xe NMR data for each of the two experimental series are assumed to be the points of zero conversion (at $t = 420\,\mathrm{s}$ for both ^{129}Xe NMR experiments). After a reaction time of 7200 s, full conversion can be expected for both miniemulsion polymerization reactions (the calorimetric data can be found in the Appendix, see Section A.2). Therefore, the calorimetric data have been scaled to conversion=100 % after 7200 s. Accordingly, the highest chemical shift values derived from the ^{129}Xe NMR data have been scaled to 100 % conversion in order to reflect the anticipated full conversion. Both methods show a good qualitative agreement demonstrating the validity of our approach. For the polymerization reaction initiated by V70 we even observe an excellent agreement for conversion rates up to 65 %. However, small differences occur for high conversion rates for both polymerizations and the reactions seem to be slightly faster when observed by ^{129}Xe NMR. In order to reveal the differences of both observation methods a thorough characterization of the polymerization products was performed.

Characterization of the polymer product

To reveal the differences of both observation methods, the solids content of the four miniemulsions as well as the mean diameter of the particles were determined (see Table 6.2). For both ^{129}Xe NMR experiments, the solids content is lower and the particle diameters are smaller than for the corresponding calorimeter experiments. As there was no visible coagulum of the miniemulsion particles, this would suggest a lower conversion in the polymerizations measured by ^{129}Xe NMR thereby contradicting the previously mentioned observation of a faster reaction observed by ^{129}Xe NMR. In order to reconcile the observed differences, we consider a mass loss of the monomer occuring during the ^{129}Xe NMR experiments. This mass loss is attributed to a diffusion of the hydrophobic monomer across the hydrophobic membrane into the dry gas flow and was tried to be minimized by a bypass of the gas flow between subsequent measurements. However, the loss of monomer could not be totally avoided due to the necessary Xe supply during the measurements. Such a loss of monomer during the polymerization reactions leads to both a higher polymer-monomer ratio after shorter reaction times (higher chemical shift in ^{129}Xe NMR) as well as to smaller particle diameters. Despite the mass loss, the accordance between the polymerizations observed by calorimetry and ^{129}Xe NMR is quite good. Due to the large concentration of monomer in the droplets at the start of the polymerization, the significance of the monomer loss is small for short reaction times. For longer reactions times, the significance of monomer loss increases which can lead to the larger difference in the observed conversions measured by calorimetry and ^{129}Xe NMR (see reaction initiated by V59 in Fig. 6.8 (a)). However, the mass loss of the hydrophobic monomer can be suppressed in future experiments by optimization of the experimental setup, for example, by the use of another type of hollow fiber membrane.

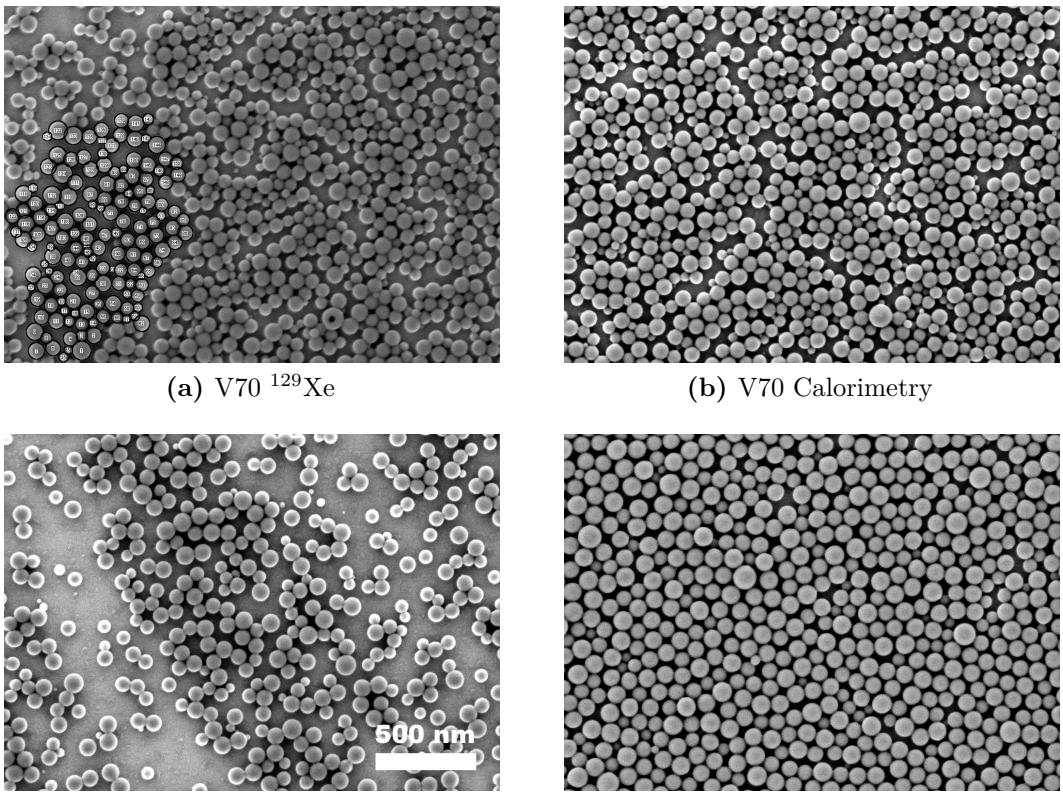

(a) V70 ^{129}Xe **(b)** V70 Calorimetry

(c) V59 ^{129}Xe **(d)** V59 Calorimetry

Figure 6.9: Scanning electron micrographs of the polymer suspensions after the polymerization.

	Solids content [%]			**Particle diameter [nm]**			
				by PCCS		**from micrographs**	
	Calorimetry	^{129}Xe NMR	Theory	Calorimetry	^{129}Xe NMR	Calorimetry	^{129}Xe NMR
V70	20.4	16.3	20.8	94.4±12.0	87.7±12.0	71.6±13.4	66.6±14.6
V59	20.4	16.3	20.8	105.6±12.0	93.9±12.0	88.8±11.0	76.9±11.0

Table 6.2: Characterization of the polymer dispersions after polymerization.

The solids content in the calorimeter experiments is only 0.4 % and 1.2 % lower than the theoretical value for a complete reaction which highlights the very high conversion achievable by miniemulsion polymerizations [Sch05, Li06]. According to the calorimetric data (see below), the conversion reached 100 % for the calorimeter experiments after a reaction time of 7200 s, which corresponds well with the very small deviation from the theoretical solids content. To obtain an insight into the particle size distributions for

the two methods, SEM images of the particles from each polymerization reaction were acquired. Normally, the droplet size and the size distribution in a miniemulsion polymerization of a given amount of monomer are determined by the amount of surfactant in the reaction mixture and fixed in the emulsification step. Due to the hydrophobic nature of the membrane surfaces present during the ^{129}Xe NMR experiments, possible changes in particle size distribution were considered due to ad- and desorption processes of the droplets to and from the membrane surface. Figure 6.9 shows two SEM images for the fast and slow polymerization from the reaction inside the NMR spectrometer and in the calorimeter. No major differences in the particle size distribution can be found for all experiments. Besides the mentioned loss of monomer in the ^{129}Xe NMR experiments, the products and the course of the polymerization reactions in both methods seem to be very well comparable.

6.6 Enzymatic Esterification in Miniemulsions

Other reaction types besides polymerization reactions can be monitored by ^{129}Xe NMR spectroscopy, too. Here, the online-monitoring of a enzymatic esterification in a miniemulsion by ^{129}Xe NMR spectroscopy is presented. When carrying out enzymatic reactions in two-phase systems, the active enzyme is often situtated in the interphase between the aqueous and the organic phase. Using a miniemulson with its enormous interphase area due to the small volume of the single droplets, enzymatic reactions can be performed very effectively [Wei09]. The online-monitoring of enzymatic reactions often proves to be difficult because this type of reactions is practically thermoneutral, ruling out the often used method of calorimetry for the reaction monitoring. However, ^{129}Xe NMR spectroscopy as a method for online-monitoring is not hindered by the lack of a reaction enthalpy. Alas, as shown here, it has other restrictions which can severely impede the use of this method.
Figure 6.10 (a) shows a series of ^{129}Xe NMR spectra recorded during the enzymatic esterification of nonanoic acid with 3-phenylpropanol to 3-phenylpropyl-nonanoate (the reaction equations is shown in Figure 6.10 (b)). The series covers a time period of 61 min with each scan taken after 2 min. The setup used here is the same as for the miniemulsion polymerization reaction and can be found in Section 3.6.
In the beginning, the heating effect due to the insertion of the sample into the heated NMR magnet is observed, similar to the series of NMR spectra for the polymerization reaction. In contrast to the polymerization reactions, no clear shift of the peak of the dissolved Xe is observable over the course of the reaction (the observed time period is long enough for a full reaction conversion). The lower part of Figure 6.10 (b) gives the reason for the non-existent shift: it shows the ^{129}Xe NMR spectra of bulk volumes of the reaction educts 3-phenylpropanol and nonanoic acid with signals of the dissolved Xe at 198 ppm and 175 ppm, respectively, and the reaction product 3-phenylpropyl-nonanoa

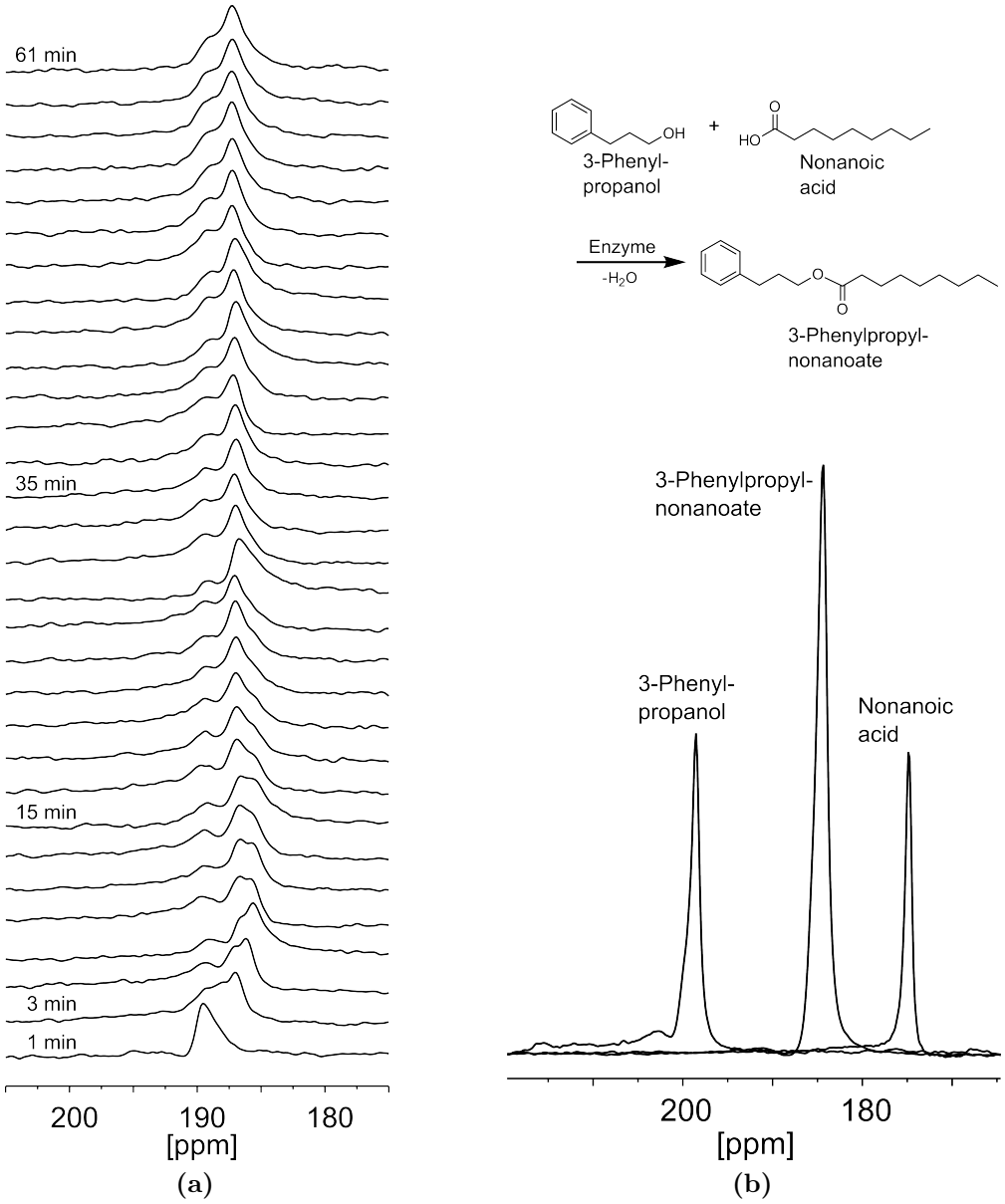

Figure 6.10: (a) Time series of ^{129}Xe NMR spectra recorded during an enzyme-catalyzed esterification in a miniemulsion at 303 K. The plots show the chemical shift range of the dissolved Xe. The enzyme was given to the miniemulsion containing the educts (alcohol and carboxylic acid) and the NMR tube was inserted into the heated NMR magnet. The insertion was used as $t = 0$ min. (b) Scheme of the enzyme-catalyzed esterification monitored by ^{129}Xe NMR spectroscopy and the ^{129}Xe NMR spectra of bulk volumes of the educts (3-phenylpropanol and nonanoic acid) and the product of the enzymatic esterification (3-phenylpropylnonanoate).

with the Xe signal at 185 ppm. Correlating these values with the NMR spectra in Figure 6.10 (a) shows some development from two, only partially separated peaks between 5 and 35 min reaction time (189 and 186 ppm) to one broad peak at 187 ppm featuring a shoulder slightly under 189 ppm for longer reaction times. Thus, although some evolution of the Xe signal in dependence of the conversion is observable, a simple tracking of the reaction is not possible for this reaction.
For the online monitoring of reactions by ^{129}Xe NMR spectroscopy, the chemical shift difference of the dissolved ^{129}Xe of the reaction educts and products plays an important role. Not all reactions are observable by the method presented in this work. This limitation is of less importance for homopolymerizations because it can be assumed that the chemical shift of ^{129}Xe in the small monomer will differ substantially from that in the polymer. Nevertheless, if the chemical shift difference between educts and products is sufficiently large, ^{129}Xe NMR spectroscopy can become a valuable and reliable method especially for the monitoring of thermoneutral reactions.

6.7 Conclusion

In the experiments presented here, the chemical shift dependence of ^{129}Xe on the conversion of polymerization reactions has been demonstrated. Using this dependence and the large NMR signal of hyperpolarized ^{129}Xe, the online monitoring of a chemical reaction by ^{129}Xe NMR was successfully accomplished (see Figure 6.11 for a schematic representation of the method). Kinetic data for free-radical polymerization reactions of an industrially important monomer with two different reaction rates were obtained with good time resolution. In order to approve the validity of our method the results of the ^{129}Xe NMR measurements were compared to calorimetric measurements [Due12].
Both methods showed a good qualitative agreement except for minor differences at higher conversion rates that could be explained by a monomer loss during the ^{129}Xe NMR experiments which can most likely be circumvented by optimization of the experimental setup. The comparability of both methods was proven by a thorough characterization of the polymer products. Hyperpolarized ^{129}Xe NMR can thus provide an excellent

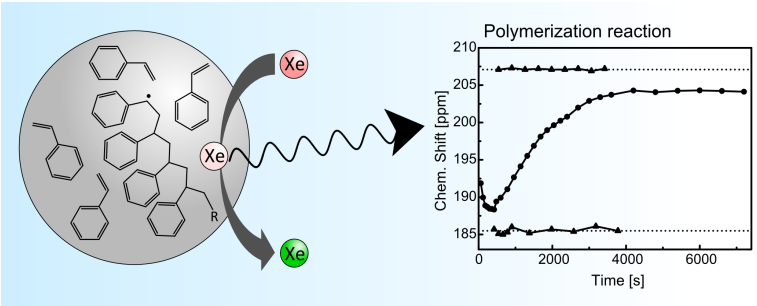

Figure 6.11: Online reaction monitoring by ^{129}Xe NMR spectroscopy.

method to investigate polymerizations exhibiting very complicated ^{1}H and ^{13}C NMR spectra due to the simplicity of the ^{129}Xe NMR spectra and the simple relationship of the ^{129}Xe chemical shift on the composition of the reaction mixture.
Besides the described experimental imperfections in this work, the accuracy of the ^{129}Xe NMR method is limited by the signal-to-noise ratio (SNR) which influences the accuracy of the determination of the chemical shift of ^{129}Xe and the achievable time-resolution. In general, the ^{129}Xe chemical shift can be determined easily and accurately given a certain signal amplitude. Thus, the limiting factor for this is the obtained signal-to-noise ratio (SNR). The same holds true for the achievable time resolution: The larger the signal, the less measurement time is necessary (here: averaging over less scans). A higher SNR - and thus a better accuracy of the presented method - could be achieved by using a polarizer setup giving a higher ^{129}Xe polarization rate (see [Rus06] for a polyrizer setup achieving high polarization rates up to 60 % and high xenon through-put) or using isotopically enriched Xe gas (giving a nearly fourfold enhancement of the SNR at the disadvantage of the high costs for the enriched gas).
Furthermore, the application of hyperpolarized ^{129}Xe NMR spectroscopy for the online monitoring of co-polymerization reactions could allow to follow the conversion of each monomer independently which cannot be done by calorimetry. However, this would be only possible in favorable cases where the two monomers exhibit very different chemical shift values of the dissolved ^{129}Xe and extensive calibration measurements for the chemical shift of ^{129}Xe dissolved in mixtures of the used co-monomers would be necessary. ^{129}Xe NMR might also be well applicable for the online monitoring of other chemical reactions apart from polymerizations. It might, for example, allow for time-resolved measurements of thermoneutral reactions which cannot be assessed by calorimetry. In this work, preliminary results of the online-monitoring of an enzymatic reaction in a miniemulsion by ^{129}Xe NMR spectroscopy are presented, demonstrating the possible difficulty when applying the new method to other reactions. Since the chemical shift of dissolved ^{129}Xe was to similar for the educts and products, the reaction conversion could not be followed in this exeplary case.
The presented method would surely also be applicable to much larger reactor volumes by using a pump-around loop which would bring a sample volume inside the (high-field) NMR magnet. By using existent 'flow-through membrane modules', it would probably be possible to dissolve the needed amount of hyperpolarized ^{129}Xe into the sample flow before each single measurement. Given the independence of the signal amplitude from the magnetic field strength for hyperpolarized substances, the use of a low-field NMR spectrometer for routine reactor monitoring seems feasible under the condition of a sufficiently large chemical shift dispersion.

7 Summary and Conclusion

In this thesis, the application of ^{129}Xe NMR spectroscopy to very different systems was studied, including dynamic and static, solid and liquid, porous and non-porous systems. Using the large non-equilibrium polarization created by hyperpolarization, time-resolved NMR measurements were used for the online-monitoring of dynamic systems.
In the first part of this work, several improvements for medical applications were achieved and their feasibility shown experimentally. Two improvements in the accumulation and storage of the hyperpolarized ^{129}Xe were presented. A newly designed and built freeze-thaw setup for the accumulation of ^{129}Xe as ice not only allowed for a large gain in speed and reproducibility of the accumulation process, but also for the (relative) enhancement of the usable polarization of over 10 % in any experiment requiring prior accumulation. A semi-continuous operation mode of the polarizer can be realized with the new freeze-thaw setup due to the extremely short thawing time of the accumulated Xe ice. A newly built helical glass freezing cell proved to be advantageous, providing a larger storage volume and a threefold increase in the longitudinal relaxation time of stored hyperpolarized ^{129}Xe. A further enhancement of the longitudinal relaxation time of ^{129}Xe by 20 % was achieved by admixture of N_2 as a buffer gas during the storage of hyperpolarized ^{129}Xe. Pursuing the efforts of simplifying the accumulation process and enhancing the storage time of hyperpolarized ^{129}Xe will allow for a wider use of the hyperpolarized gas in (medical) MRI experiments.
Concerning the use of hyperpolarized ^{129}Xe in MRI, the influence of the diffusion coefficient of the gas on parameters of the image contrast was shown by admixture of a buffer gas and thus changing the diffusion coefficient. Using a newly proposed capillary phantom, this diffusion effect should be much more distinct in future experiments, allowing for valuable conclusions for ^{129}Xe MRI of lungs.
In the second part of this work, a polymer system with unique features was probed by ^{129}Xe NMR spectroscopy. The method proved to be a valuable tool for the characterization of the anisotropic properties of semicrystalline, syndiotactic polystyrene films. Depending on the phase, the polymer films contained either hollow cavities or channels with sizes in the sub-nanometer range, allowing for adsorption of ^{129}Xe and subsequent NMR measurements. Due to the preparation of the films, the cavities or channels were oriented to a certain degree inside the films. Despite the use of this 'real-world' system, the transfer of the anisotropic properties from the material to adsorbed ^{129}Xe atoms could be shown, which was previously only known for fully crystalline materials, e.g. zeolites or organic crystals.
For two nanoporous phases of the syndiotactic polystyrene films, the δ and the ε phase,

strong anisotropic effects towards the adsorbed ^{129}Xe atoms were recorded in NMR experiments. The anisotropic behavior towards atomar or molecular guests inside the polymer films could be proven here for the first time for the ε phase. In the future, further measurements of film samples with differing degrees of orientation will allow to interpolate to the chemical shift values a perfectly oriented crystal phase.
For the ε phase, containing nanochannels, the dominance of interactions between ^{129}Xe atoms in the channels compared to interactions between Xe atoms and the channel walls could be proven by measurements of a powder sample of the polymer material and experiments including the rotation of the films in the external magnetic field as well as temperature-dependent measurements.
In the last part of this work, a new method for the online monitoring of chemical reactions was proposed and its feasibility and validity were experimentally proven. The chemical shift dependence of dissolved ^{129}Xe on the composition of a reaction mixture was proven for different mixtures of monomer and polymer and used for the online monitoring of miniemulsion polymerization reactions. A chemical shift dependence on the size of any polymer particles in a dispersion could be excluded. Kinetic data for free-radical polymerization reactions of an industrially important monomer with two different reaction rates were obtained with good time resolution without the need of sample extraction. The results of the time-resolved ^{129}Xe NMR measurements were compared to those from calorimetric measurements, showing a good qualitative agreement. Minor differences at higher conversion were explained by monomer loss during the ^{129}Xe NMR measurements. These experimental imperfections can be circumvented in the future by an optimization of the experimental setup.
^{129}Xe NMR spectroscopy provided an excellent method for the online monitoring of polymerization reactions, due to the simplicity of the ^{129}Xe NMR spectra and the simple relationship between the ^{129}Xe chemical shift and the reaction conversion. Since the accuracy of the new method is limited by the achievable SNR, limiting the accuracy of determination of the chemical shift of the dissolved ^{129}Xe as well as the achievable time-resolution, an increase in SNR of the NMR measurements will further increase the accuracy of the new method in the future. A higher SNR could be achieved by use of isotopically enriched ^{129}Xe or by use of another polarizer setup giving a higher ^{129}Xe polarization rate. An application of the method described here to much larger reaction volumes seems feasible by use of a pump-around loop and the membrane technique to dissolve the hyperpolarized ^{129}Xe. Furthermore, since the signal amplitude of the hyperpolarized ^{129}Xe is independent from the magnetic field strength, the new method can be used in a low-field NMR spectrometer under the condition of a sufficiently large chemical shift dispersion.
The applicability of the new method to reactions other than polymerization reactions was investigated by the online monitoring of an enzymatic reaction in a miniemulsion. Enzymatic and other reactions, which are nearly thermoneutral, often prove to be impossible to follow in calorimetry. In the reaction investigated here, the reaction conversion could not be followed due to the similarity of the chemical shift of ^{129}Xe

dissolved in the educts and the product of the reaction. Nevertheless, the application of hyperpolarized ^{129}Xe NMR spectroscopy for the online monitoring of reactions which cannot be followed by calorimetry, e.g. the independent monitoring of each co-monomer in a co-polymerization, seems feasible under the favorable condition of different chemical shift values of the different monomers.
In this work, the remarkable versatility and usefulness of applications of ^{129}Xe NMR experiments could be further extended. The characterization of 'real-world' systems showing very high degrees of anisotropy by ^{129}Xe will be very valuable in future applications. The successful combination of the large sensitivity of ^{129}Xe, the NMR signal enhancements due to hyperpolarization, and the solubilty of ^{129}Xe gives access to the large new field of investigations of chemical reaction kinetics in dynamic and complex systems like miniemulsions.

A Appendix

A.1 Fits of the ^{129}Xe NMR signal in polystyrene films

A.1.1 Fits for the ε phase - Nanochannels

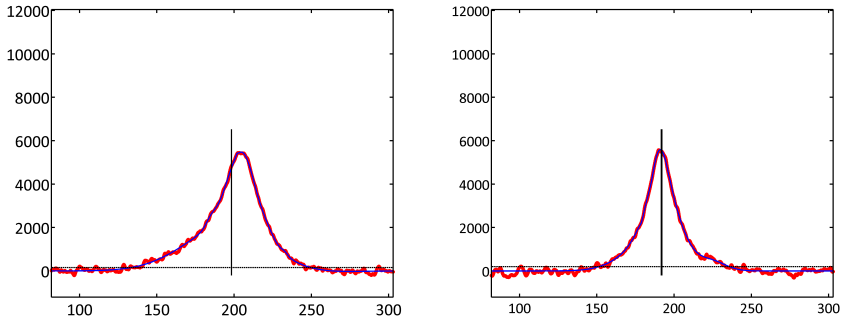

(a) Sample 05 **(b)** Sample 04

Figure A.1: Fits (blue line) of the NMR signal of xenon (red points) adsorbed in the ε phase (Sample 04 and Sample 05). The center of gravity gravity (vertical black line) and the threshold value (horizontal black, dotted line) used in the calculation for the center of gravity are shown.

A.1.2 Fits for the ε phase - 'New' Batch

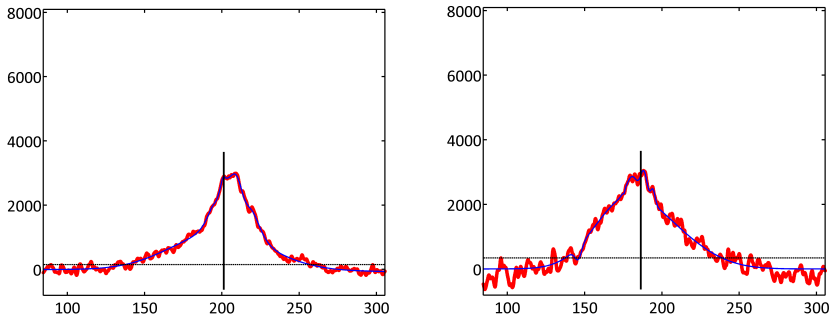

(a) Sample 11 **(b)** Sample 12

Figure A.2: Centers of gravity fitted for sample 11 and 12.

A.2 Mechanistic details of the Miniemulsion Polymerization Reaction

In order to gain a more detailed mechanistic insight into the two reactions and to see whether both reactions follow the classic on/off mechanism for miniemulsion polymerization, the original data from calorimetry were investigated (Figure A.3 (a) and (b)), and the molecular weight distributions were analyzed with SEC (Figure A.3 (c)).

The calorimeter data reveal additional information on the time courses and some mechanistic features of the polymerization reactions initiated with V59 and V70. At a conversion of 70 %, a gel peak is visible in the curve of the reaction initiated with V59. Despite the almost identical droplet size, the polymerization initiated with V70 does not produce a gel peak. This means that the viscosity in the latter system is lower, as the diffusion of monomer is not limited enough to cause a gel peak. The molecular weight obtained from SEC supports this statement. Initiation with V70 leads to a significantly lower molecular weight polymer with a very broad distribution (Table A.1, Figure A.3 (c)). This can be explained with the extremely fast decomposition of V70 during the nucleation stage. The average life time of a generated radical will be significantly shorter as in the case of V59. Thus, the polymerization can only proceed for a shorter time and thus, shorter polymer chains are generated.

The average number of radicals $\overline{n}$ per droplet was calculated using the procedure described by Bechthold et al. [Bec00]. Figure A.3 (c) shows $\overline{n}$ for both reactions around 0.5. Thus, both reactions follow the classic on/off mechanism of miniemulsion polymerization, where either one active or no radical can be found in a droplet.

	M_n $\left[g \cdot mol^{-1}\right]$	M_w $\left[g \cdot mol^{-1}\right]$	**D**
V70	$2.6 \cdot 10^4$	$1.4 \cdot 10^5$	5.4
V59	$2.5 \cdot 10^5$	$6.3 \cdot 10^5$	2.5

Table A.1: Molecular weight distributions obtained from SEC (RI-detector).

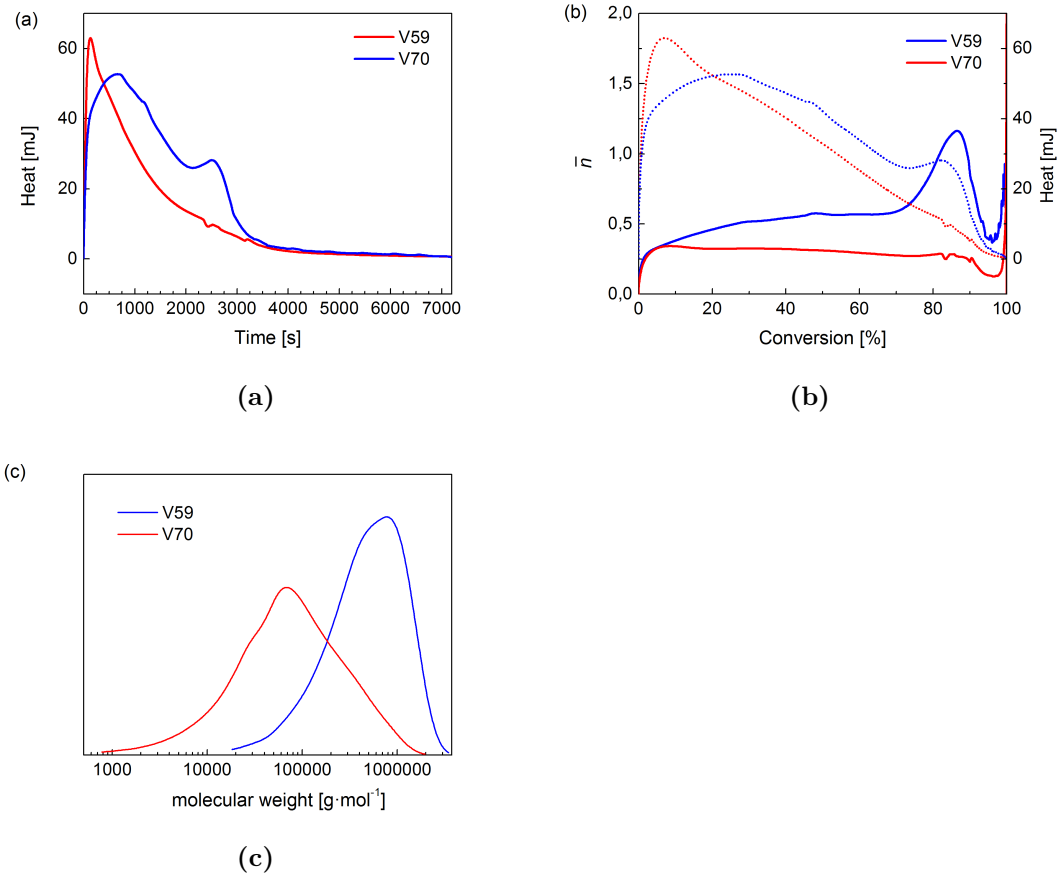

Figure A.3: Calorimeter data as obtained from the experiments versus time (a) and versus conversion ((b), dashed lines) and the average number of radicals $\overline{n}$ ((b), solid lines) versus the conversion. (c) Molecular weight (RI-detector) distributions obtained with SEC.

Bibliography

[Abd07] Abdollahi, M. and Sharifpour, M.: A New Simple Procedure to Calculate Monomer Reactivity Ratios by Using on-Line H-1 NMR Kinetic Experiments: Copolymerization System with Greater Difference between the Monomer Reactivity Ratios. *Polymer* (2007), vol. 48(1): pp. 25–30

[Aco12] Acosta, R. H.; Blümler, P.; Münnemann, K. and Spiess, H.-W.: Mixture and Dissolution of Laser Polarized Noble Gases: Spectroscopic and Imaging Applications. *Progress in Nuclear Magnetic Resonance Spectroscopy* (2012)

[Aim08] Aime, S.; Dastru, W.; Gobetto, R.; Santelia, D. and Viale, A.: *Agents for Polarization Enhancement in MRI*, vol. 185 of *Handbook of Experimental Pharmacology*, Springer-Verlag Berlin, Heidelberger Platz 3, D-14197 Berlin, Germany (2008), pp. 247–272

[AL03] Ardenkjaer-Larsen, J. H.; Fridlund, B.; Gram, A.; Hansson, G.; Hansson, L.; Lerche, M. H.; Servin, R.; Thaning, M. and Golman, K.: Increase in Signal-to-Noise Ratio of > 10,000 Times in Liquid-State NMR. *Proceedings of the National Academy of Sciences of the United States of America* (2003), vol. 100(18): pp. 10158–10163

[Alb94] Albert, M. S.; Cates, G. D.; Driehuys, B.; Happer, W.; Saam, B.; Springer, C. S. and Wishnia, A.: Biological Magnetic-Resonance-Imaging Using Laser Polarized Xe-129. *Nature* (1994), vol. 370(6486): pp. 199–201

[Alb05] Albunia, A. R.; Milano, G.; Venditto, V. and Guerra, G.: A Clear-Cut Experimental Method to Discriminate between in-Plane and out-of-Plane Molecular Transition Moments. *Journal of the American Chemical Society* (2005), vol. 127(38): pp. 13114–13115

[Alb08a] Albunia, A. R.; Annunziata, L. and Guerra, G.: Guest-Induced Syndiotactic Polystyrene Cocrystal Formation from Gamma and Alpha Phases. *Macromolecules* (2008), vol. 41(7): pp. 2683–2688

[Alb08b] Albunia, A. R.; Minucci, T. and Guerra, G.: Ethylene Removal by Sorption from Polymeric Crystalline Frameworks. *Journal of Materials Chemistry* (2008), vol. 18(9): pp. 1046–1050

[Alb08c] Albunia, A. R.; Rizzo, P.; Tarallo, O.; Petraccone, V. and Guerra, G.: Layers of Close-Packed Alternated Enantiomorphous Helices and

the Three Different Uniplanar Orientations of Syndiotactic Polystyrene. *Macromolecules* (2008), vol. 41(22): pp. 8632–8642

[Alb09a] Albunia, A. R.; Graf, R.; Grassi, A.; Guerra, G. and Spiess, H. W.: Geometry of Complex Molecular Motions of Guest Molecules in Polymers from Solid State 2h NMR. *Macromolecules* (2009), vol. 42(14): pp. 4929–4931

[Alb09b] Albunia, A. R.; Rizzo, P. and Guerra, G.: Polymeric Films with Three Different Orientations of Crystalline-Phase Empty Channels. *Chemistry of Materials* (2009), vol. 21(14): pp. 3370–3375

[Alb10] Albunia, A. R.; D'Aniello, C. and Guerra, G.: Three Different Co-Crystalline Phases of Syndiotactic Polystyrene with a Nitroxide Radical. *Crystengcomm* (2010), vol. 12(11)

[Alb11a] Albunia, A. R. and Graf, R.: The Effect of Inclusion of Dichloromethane in the -Clathrate Phase of Syndiotactic Polystyrene. *Soft Materials* (2011), vol. 9(2-3): pp. 183–198

[Alb11b] Albunia, A. R.; Oliva, P. and Grassi, A.: Interactions of Volatile Organic Compounds with Syndiotactic Polystyrene Crystalline Nanocavities. *Journal of Physical Chemistry A* (2011), vol. 115(4): pp. 443–452

[Alb11c] Albunia, A. R.; Rizzo, P. and Guerra, G.: Two Different Uniplanar - Axial Orientations of Syndiotactic Polystyrene Films. *Macromolecules* (2011), vol. 44(14): pp. 5671–5681

[Amm82] Ammann, C.; Meier, P. and Merbach, A. E.: A Simple Multi-Nuclear NMR Thermometer. *Journal of Magnetic Resonance* (1982), vol. 46(2): pp. 319–321

[Amo07] Amor, N.: NMR Und MRI Von Hyperpolarisiertem Xenon-129 in Biorelevanten Flüssigkeiten. Diploma thesis, Johannes Gutenberg University Mainz (2007)

[Amo09] Amor, N.; Münnemann, K.; Zänker, P. P.; Blümler, P.; Meise, F. M.; Schreiber, L. M.; Scholz, A.; Schmiedeskamp, J. and Spiess, H. W.: Magnetic Resonance Imaging of Dissolved Hyperpolarized ^{129}Xe Using a Membrane-Based Continuous Flow System. *Journal of Magnetic Resonance* (2009), vol. 201(1): pp. 93–99

[Amo11] Amor, N.; Hamilton, K.; Kuppers, M.; Steinseifer, U.; Appelt, S.; Blümich, B. and Schmitz-Rode, T.: NMR and MRI of Blood-Dissolved Hyperpolarized Xe-129 in Different Hollow-Fiber Membranes. *Chemphyschem* (2011), vol. 12(16): pp. 2941–2947

[Ang08] Anger, B. C.; Schrank, G.; Schoeck, A.; Butler, K. A.; Solum, M. S.; Pugmire, R. J. and Saam, B.: Gas-Phase Spin Relaxation of ^{129}Xe. *Physical Review A* (2008), vol. 78(4)

[AP07] Agulles-Pedros, L.: Diffusion of Laser-Polarized Gases in MRI. PhD thesis, Johannes Gutenberg University Mainz (2007)

[AP09] Agulles-Pedros, L.; Blümler, P.; Acosta, R. H. and Spiess, H. W.: Resolution Enhancement in MRI of Laser Polarized ^{3}He by Control of Diffusion. *Journal of Magnetic Resonance* (2009), vol. 197(1): pp. 56–62

[App98] Appelt, S.; Baranga, A. B.; Erickson, C. J.; Romalis, M. V.; Young, A. R. and Happer, W.: Theory of Spin-Exchange Optical Pumping of He-3 and Xe-129. *Physical Review A* (1998), vol. 58(2): pp. 1412–1439

[Atk09] Atkinson, K. D.; Cowley, M. J.; Duckett, S. B.; Elliott, P. I. P.; Green, G. G. R.; Lopez-Serrano, J.; Khazal, I. G. and Whitwood, A. C.: Para-Hydrogen Induced Polarization without Incorporation of Para-Hydrogen into the Analyte. *Inorganic Chemistry* (2009), vol. 48(2): pp. 663–670

[Bab03] Babcock, E.; Nelson, I.; Kadlecek, S.; Driehuys, B.; Anderson, L. W.; Hersman, F. W. and Walker, T. G.: Hybrid Spin-Exchange Optical Pumping of He-3. *Physical Review Letters* (2003), vol. 91(12)

[Bar62] Bartlett, N.: Xenon Hexafluoroplatinate(V) Xe+PtF_6. *Proceedings of the Chemical Society of London* (1962), (JUN): p. 218

[Bau06] Baumer, D.; Brunner, E.; Blümler, P.; Zänker, P. P. and Spiess, H. W.: NMR Spectroscopy of Laser-Polarized Xe-129 under Continuous Flow: A Method to Study Aqueous Solutions of Biomolecules. *Angewandte Chemie-International Edition* (2006), vol. 45(43): pp. 7282–7284

[Bau10] Bauer, C.; Becker, K.; Herrmann, T.; Lilge, D.; Roth, M. and Busch, M.: From Fundamental Polymerization Kinetics to Process Application - a Realistic Vision? *Macromolecular Chemistry and Physics* (2010), vol. 211(5): pp. 510–519

[Bec92] Beck, J. S.; Vartuli, J. C.; Roth, W. J.; Leonowicz, M. E.; Kresge, C. T.; Schmitt, K. D.; Chu, C. T. W.; Olson, D. H.; Sheppard, E. W.; McCullen, S. B.; Higgins, J. B. and Schlenker, J. L.: A New Family of Mesoporous Molecular-Sieves Prepared with Liquid-Crystal Templates. *Journal of the American Chemical Society* (1992), vol. 114(27): pp. 10834–10843

[Bec00] Bechthold, N. and Landfester, K.: Kinetics of Miniemulsion Polymerization as Revealed by Calorimetry. *Macromolecules* (2000), vol. 33(13): pp. 4682–4689

[Bec07] Beckmann, N.; Cannet, C.; Karmouty-Quintana, H.; Tigani, B.; Zurbruegg, S.; Ble, F. X.; Cremillieux, Y. and Trifilieff, A.: Lung MRI for Experimental Drug Research. *European Journal of Radiology* (2007), vol. 64(3): pp. 381–396

[Ber08] Berthault, P.; Bogaert-Buchmann, A.; Desvaux, H.; Huber, G. and Boulard, Y.: Sensitivity and Multiplexing Capabilities of MRI Based on Polarized ^{129}Xe Biosensors. *Journal of the American Chemical Society* (2008), vol. 130(49): pp. 16456–+

[Ber09] Berthault, P.; Huber, G. and Desvaux, H.: Biosensing Using Laser-Polarized Xenon NMR/MRI. *Progress in Nuclear Magnetic Resonance Spectroscopy* (2009), vol. 55(1): pp. 35–60

[Beu02] Beuermann, S. and Buback, M.: Rate Coefficients of Free-Radical Polymerization Deduced from Pulsed Laser Experiments. *Progress in Polymer Science* (2002), vol. 27(2): pp. 191–254

[Bha82] Bhaskar, N. D.; Happer, W. and Mcclelland, T.: Efficiency of Spin Exchange between Rubidium Spins and Xe-129 Nuclei in a Gas. *Physical Review Letters* (1982), vol. 49(1): pp. 25–28

[Blo46] Bloch, F.; Hansen, W. W. and Packard, Martin: Nuclear Induction. *Physical Review* (1946), vol. 69(3-4): p. 127

[Bly99] Blythe, P. J.; Klein, A.; Phillips, J. A.; Sudol, E. D. and El-Aasser, M. S.: Miniemulsion Polymerization of Styrene Using the Oil-Soluble Initiator Ambn. *Journal of Polymer Science Part a-Polymer Chemistry* (1999), vol. 37(23): pp. 4449–4457

[Bou60] Bouchiat, M. A.; Carver, T. R. and Varnum, C. M.: Nuclear Polarization in He-3 Gas Induced by Optical Pumping and Dipolar Exchange. *Physical Review Letters* (1960), vol. 5(8): pp. 373–375

[Bou69] Bouchiat, C. C.; Bouchiat, M. A. and Pottier, L. C. L.: Evidence for Rb-Rare-Gas Molecules from Relaxation of Polarized Rb Atoms in a Rare Gas . Theory. *Physical Review* (1969), vol. 181(1): p. 144

[Bow87] Bowers, C. R. and Weitekamp, D. P.: Para-Hydrogen and Synthesis Allow Dramatically Enhanced Nuclear Alignment. *Journal of the American Chemical Society* (1987), vol. 109(18): pp. 5541–5542

[Bow07] Bowers, C. R. and Cheng, C. Y.: Observation of Single-File Diffusion in Dipeptide Nanotubes by Continuous-Flow Hyperpolarized Xenon-129 NMR Spectroscopy. *Chemphyschem* (2007), vol. 8(14): pp. 2077–2081

[Bow11] Bowen, S.; Sekar, G. and Hilty, C.: Rapid Determination of Biosynthetic Pathways Using Fractional Isotope Enrichment and High-Resolution Dynamic Nuclear Polarization Enhanced NMR. *NMR in Biomedicine* (2011), vol. 24(8): pp. 1016–22

[BP06] Berry-Pusey, B. N.; Anger, B. C.; Laicher, G. and Saam, B.: Nuclear Spin Relaxation of Xe-129 Due to Persistent Xenon Dimers. *Physical Review A* (2006), vol. 74(6)

[Buc56] Buckingham, A. D. and Pople, J. A.: Electromagnetic Properties of Compressed Gases. *Discussions of the Faraday Society* (1956), (22): pp. 17–21

[Car56] Carver, T. R. and Slichter, C. P.: Experimental Verification of the Overhauser Nuclear Polarization Effect. *Physical Review* (1956), vol. 102(4): pp. 975–980

[Cat88a] Cates, G. D.; Schaefer, S. R. and Happer, W.: Relaxation of Spins Due to Field Inhomogeneities in Gaseous Samples at Low Magnetic-Fields and Low-Pressures. *Physical Review A* (1988), vol. 37(8): pp. 2877–2885

[Cat88b] Cates, G. D.; White, D. J.; Chien, T. R.; Schaefer, S. R. and Happer, W.: Spin Relaxation in Gases Due to Inhomogeneous Static and Oscillating Magnetic-Fields. *Physical Review A* (1988), vol. 38(10): pp. 5092–5106

[Cat92] Cates, G. D.; Fitzgerald, R. J.; Barton, A. S.; Bogorad, P.; Gatzke, M.; Newbury, N. R. and Saam, B.: Rb Xe-129 Spin-Exchange Rates Due to Binary and 3-Body Collisions at High Xe Pressures. *Physical Review A* (1992), vol. 45(7): pp. 4631–4639

[Cha02] Chann, B.; Nelson, I. A.; Anderson, L. W.; Driehuys, B. and Walker, T. G.: Xe-129-Xe Molecular Spin Relaxation. *Physical Review Letters* (2002), vol. 88(11)

[Cha03] Chann, B.; Babcock, E.; Anderson, L. W.; Walker, T. G.; Chen, W. C.; Smith, T. B.; Thompson, A. K. and Gentile, T. R.: Production of Highly Polarized He-3 Using Spectrally Narrowed Diode Laser Array Bars. *Journal of Applied Physics* (2003), vol. 94(10): pp. 6908–6914

[Che03] Cherubini, A. and Bifone, A.: Hyperpolarised Xenon in Biology. *Progress in Nuclear Magnetic Resonance Spectroscopy* (2003), vol. 42(1-2): pp. 1–30

[Che07] Chen, W. C.; Gentile, T. R.; Walker, T. G. and Babcock, E.: Spin-Exchange Optical Pumping of He-3 with Rb-K Mixtures and Pure K. *Physical Review A* (2007), vol. 75(1)

[Cle08] Cleveland, Z. I. and Meersmann, T.: Binary-Collision-Induced Longitudinal Relaxation in Gas-Phase ^{83}Kr. *Journal of Chemical Physics* (2008), vol. 129(24)

[Cle09] Cleveland, Z. I.; Moeller, H. E.; Hedlund, L. W. and Driehuys, B.: Continuously Infusing Hyperpolarized ^{129}Xe into Flowing Aqueous Solutions Using Hydrophobic Gas Exchange Membranes. *Journal of Physical Chemistry B* (2009), vol. 113(37): pp. 12489–12499

[Cun02] Cunningham, M. F.: Living/Controlled Radical Polymerizations in Dispersed Phase Systems. *Progress in Polymer Science* (2002), vol. 27(6): pp. 1039–1067

[Dan09] Daniel, C.; Giudice, S. and Guerra, G.: Syndiotatic Polystyrene Aerogels with Beta, Gamma, and Epsilon Crystalline Phases. *Chemistry of Materials* (2009), vol. 21(6): pp. 1028–1034

[Dav02] Davis, M. E.: Ordered Porous Materials for Emerging Applications. *Nature* (2002), vol. 417(6891): pp. 813–821

[Dem82] Demenorval, L. C.; Fraissard, J. P. and Ito, T.: Nuclear Magnetic-Resonance Study of Xenon Adsorbed on Metal-Nay Zeolites - a New Method for the Determination of the Mean Number of Atoms in Small Metallic Particles Supported on Y-Zeolites. *Journal of the Chemical Society-Faraday Transactions I* (1982), vol. 78: pp. 403–410

[Dem87] Demarquay, J. and Fraissard, J.: Xe-129 NMR of Xenon Adsorbed on Zeolites - Relationship between the Chemical-Shift and the Void Space. *Chemical Physics Letters* (1987), vol. 136(3-4): pp. 314–318

[Den06] Deninger, A.; Heil, W.; Otten, E. W.; Wolf, M.; Kremer, R. K. and Simon, A.: Paramagnetic Relaxation of Spin Polarized He-3 at Coated Glass Walls Part Ii. *European Physical Journal D* (2006), vol. 38(3): pp. 439–443

[Dmo09] Dmochowski, I.: Xenon out of Its Shell. *Nature Chemistry* (2009), vol. 1(3): pp. 250–250

[Doh11] Dohnalik, T.; Nikiel, A.; Palasz, T.; Suchanek, M.; Collier, G.; Grenczuk, M.; Glowacz, B. and Olejniczak, Z.: Optimization of the Pumping Laser Beam Spatial Profile in the Meop Experiment Performed at Elevated ^{3}He Pressures. *European Physical Journal-Applied Physics* (2011), vol. 54(2)

[Dri95] Driehuys, B.; Cates, G. D. and Happer, W.: Surface Relaxation Mechanisms of Laser-Polarized Xe-129. *Physical Review Letters* (1995), vol. 74(24): pp. 4943–4946

[Dri96] Driehuys, B.; Cates, G. D.; Miron, E.; Sauer, K.; Walter, D. K. and Happer, W.: High-Volume Production of Laser-Polarized Xe-129. *Applied Physics Letters* (1996), vol. 69(12): pp. 1668–1670

[Dri09] Driehuys, B.; Moeller, H. E.; Cleveland, Z. I.; Pollaro, J. and Hedlund, L. W.: Pulmonary Perfusion and Xenon Gas Exchange in Rats: Mr Imaging with Intravenous Injection of Hyperpolarized (129)Xe. *Radiology* (2009), vol. 252(2): pp. 386–393

[Dri11] Driehuys, B.; Kaushik, S. S.; Cleveland, Z. I.; Cofer, G. P.; Metz, G.; Beaver, D.; Nouls, J.; Kraft, M.; Auffermann, W.; Wolber, J. and McAdams, H. P.: Diffusion-Weighted Hyperpolarized ^{129}Xe MRI in Healthy Volunteers and Subjects with Chronic Obstructive Pulmonary Disease. *Magnetic Resonance in Medicine* (2011), vol. 65(4): pp. 1155–1165

[Due12] Duewel, M.; Vogel, N.; Weiss, C. K.; Landfester, K.; Spiess, H.-W. and Münnemann, K.: Online Monitoring of Styrene Polymerization in Miniemulsion by Hyperpolarized ^{129}Xe NMR Spectroscopy. *Macromolecules* (2012), vol. 45(4): pp. 1839–1846

[Eli09] Elias, Hans-Georg: Makromoleküle (2009)

[Emm10] Emmler, Thomas; Heinrich, Kathleen; Fritsch, Detlev; Budd, Peter M.; Chaukura, Nhamo; Ehlers, Dennis; Ratzke, Klaus and Faupel, Franz: Free Volume Investigation of Polymers of Intrinsic Microporosity (Pims): Pim-1 and Pim1 Copolymers Incorporating Ethanoanthracene Units. *Macromolecules* (2010), vol. 43(14): pp. 6075–6084

[Fei12] Feiz, S. and Navarchian, A. H.: Emulsion Polymerization of Styrene: Simulation the Effects of Mixed Ionic and Non-Ionic Surfactant System in the Presence of Coagulation. *Chemical Engineering Science* (2012), vol. 69(1): pp. 431–439

[Fil11] Filimonova, S., S Filimonova; Nossov, A.; Dumig, A.; Gedeon, A.; Kogel-Knabner, I. and Knicker, H.: Evaluating Pore Structures of Soil Components with a Combination of "Conventional" and Hyperpolarised ^{129}Xe NMR Studies. *Geoderma* (2011), vol. 162(1-2): pp. 96–106

[Fon09] Fonseca, G. E.; Dube, M. A. and Penlidis, A.: A Critical Overview of Sensors for Monitoring Polymerizations. *Macromolecular Reaction Engineering* (2009), vol. 3(7): pp. 327–373

[Fra10] Frauendorfer, E.; Wolf, A. and Hergeth, W. D.: Polymerization Online Monitoring. *Chemical Engineering and Technology* (2010), vol. 33(11): pp. 1767–1778

[Fry44] Fryling, C. F.: Emulsion Polymerization of Synthetic Rubber in 10-Gramme Systems. *Industrial and Engineering Chemistry (Analytical Edition)* (1944), vol. 16: pp. 1–44

[Fuj06] Fujiki, Y.; Tokunaga, N.; Shinkai, S. and Sada, K.: Anisotropic Decoration of Gold Nanoparticles onto Specific Crystal Faces of Organic Single Crystals. *Angewandte Chemie-International Edition* (2006), vol. 45(29): pp. 4764–4767

[Gar74] Garroway, A. N.; Grannell, P. K. and Mansfield, P.: Image-Formation in NMR by a Selective Irradiative Process. *Journal of Physics C-Solid State Physics* (1974), vol. 7(24): pp. L457–L462

[Gho10] Ghosh, R. K. and Romalis, M. V.: Measurement of Spin-Exchange and Relaxation Parameters for Polarizing (21)Ne with K and Rb. *Physical Review A* (2010), vol. 81(4)

[Glo11] Gloggler, S.; Blümich, B. and Appelt, S.: Real-Time Detection of Polymerization Reactions with Hyperpolarized Xenon at Low Magnetic Fields. *Magnetic Resonance in Porous Media* (2011), vol. 1330: pp. 101–104

[Gol03] Golemme, G.; Nagy, J. B.; Fonseca, A.; Algieri, C. and Yampolskii, Y.: Xe-129-NMR Study of Free Volume in Amorphous Perfluorinated Polymers: Comparsion with Other Methods. *Polymer* (2003), vol. 44(17): pp. 5039–5045

[Got04] Goto, A. and Fukuda, T.: Kinetics of Living Radical Polymerization. *Progress in Polymer Science* (2004), vol. 29(4): pp. 329–385

[Gra05] Gramm, S.; Komber, H. and Schmaljohann, D.: Copolymerization Kinetics of N-Isopropylacrylamide and Diethylene Glycol Monomethylether Monomethacrylate Determined by Online NMR Spectroscopy. *Journal of Polymer Science Part a-Polymer Chemistry* (2005), vol. 43(1): pp. 142–148

[Gue09a] Guerra, G.; Albunia, A. R. and D'Aniello, C.: *Preparation, Structure, Properties, and Applications of Co-Crystals and Nanoporous Crystalline Phases of Syndiotactic Polystyrene*, John Wiley and Sons, Inc. (2009), pp. 194–237

[Gue09b] Guerra, G.; Albunia, A. R.; D'Aniello, C.; Gatteschi, D.; Mannini, M. and Sorace, L.: Ordering Magnetic Molecules within Nanoporous Crystalline Polymers. *Chemistry of Materials* (2009), vol. 21(20): pp. 4750–4752

[Guo11] Guo, Y. and Zetterlund, P. B.: Particle Formation Mechanism in Radical Polymerization in Miniemulsion Based on in Situ Surfactant Formation without High Energy Homogenization. *Polymer* (2011), vol. 52(19): pp. 4199–4207

[Gup97] Gupta, V.; Kim, D.; Davis, H. T. and McCormick, A. V.: Xe-129 NMR Chemical Shifts in Zeolites: Effect of Loading Studied by Monte Carlo Simulations. *Journal of Physical Chemistry B* (1997), vol. 101(2): pp. 129–137

[Gut10] Guthausen, G.; Vargas, M. A.; Cudaj, M.; Hailu, K. and Sachsenheimer, K.: Online Low-Field (1)H NMR Spectroscopy: Monitoring of Emulsion Polymerization of Butyl Acrylate. *Macromolecules* (2010), vol. 43(13): pp. 5561–5568

[Had00] Haddleton, D. M.; Perrier, S. and Bon, S. A. F.: Copper(I)-Mediated Living Radical Polymerization in the Presence of Oxyethylene Groups: Online H-1 NMR Spectroscopy to Investigate Solvent Effects. *Macromolecules* (2000), vol. 33(22): pp. 8246–8251

[Han04] Han, S.; Kuhn, H.; Hasing, F. W.; Münnemann, K.; Blümich, B. and Appelt, S.: Time Resolved Spectroscopic NMR Imaging Using Hyper-

polarized ^{129}Xe. *Journal of Magnetic Resonance* (2004), vol. 167(2): pp. 298–305

[Hap72] Happer, W.: Optical-Pumping. *Reviews of Modern Physics* (1972), vol. 44(2): p. 169

[Hap84] Happer, W.; Miron, E.; Schaefer, S.; Schreiber, D.; Vanwijngaarden, W. A. and Zeng, X.: Polarization of the Nuclear Spins of Noble-Gas Atoms by Spin Exchange with Optically Pumped Alkali-Metal Atoms. *Physical Review A* (1984), vol. 29(6): pp. 3092–3110

[Har47] Harkins, W. D.: A General Theory of the Mechanism of Emulsion Polymerization. *Journal of the American Chemical Society* (1947), vol. 69(6): p. 1428

[Haw53] Hawkins, W. B. and Dicke, R. H.: The Polarization of Sodium Atoms. *Physical Review* (1953), vol. 91(4): pp. 1008–1009

[Hei95] Heil, W.; Humblot, H.; Otten, E.; Schafer, M.; Sarkau, R. and Leduc, M.: Very Long Nuclear-Relaxation Times of Spin-Polarized Helium-3 in Metal-Coated Cells. *Physics Letters A* (1995), vol. 201(4): pp. 337–343

[Hof11] Hoffmann, H. C.; Assfour, B.; Epperlein, F.; Klein, N.; Paasch, S.; Senkovska, I.; Kaskel, S.; Seifert, G. and Brunner, E.: High-Pressure in Situ ^{129}Xe NMR Spectroscopy and Computer Simulations of Breathing Transitions in the Metal-Organic Framework Ni(2)(2,6-Ndc)(2)(Dabco) (Dut-8(Ni)). *Journal of the American Chemical Society* (2011), vol. 133(22): pp. 8681–8690

[Hor09] Hori, Y.; Kimura, A.; Wakayama, T.; Kitamoto, M.; Imai, F.; Imai, H. and Fujiwara, H.: 3d Hyperpolarized ^{129}Xe MRI of Mouse Lung at Low Xenon Concentration Using a Continuous Flow-Type Hyperpolarizing System: Feasibility for Quantitative Measurement of Regional Ventilation. *Magnetic Resonance in Medical Sciences* (2009), vol. 8(2): pp. 73–79

[Hua01] Huang, X. Y. and Brittain, W. J.: Synthesis and Characterization of Pmma Nanocomposites by Suspension and Emulsion Polymerization. *Macromolecules* (2001), vol. 34(10): pp. 3255–3260

[Ish95] Ishizu, Koji; Tsubaki, Shigeki and Uchida, Satoshi: Free-Radical Polymerization of Macromonomers. *Journal of Macromolecular Science, Part A* (1995), vol. 32(7): pp. 1227–1234

[Jac01] Jacob, R. E.; Morgan, S. W.; Saam, B. and Leawoods, J. C.: Wall Relaxation of He-3 in Spin-Exchange Cells. *Physical Review Letters* (2001), vol. 87(14)

[Jam73] Jameson, C. J.; Jameson, A. K. and Cohen, S. M.: Temperature and Density Dependence of Xe-129 Chemical-Shift in Xenon Gas. *Journal of Chemical Physics* (1973), vol. 59(8): pp. 4540–4546

[Jam88] Jameson, C. J.; Jameson, A. K. and Hwang, J. K.: Nuclear-Spin Relaxation by Intermolecular Magnetic Dipole Coupling in the Gas-Phase - Xe-129 in Oxygen. *Journal of Chemical Physics* (1988), vol. 89(7): pp. 4074–4081

[Jam92] Jameson, C. J. and Dedios, A. C.: Abinitio Calculations of the Intermolecular Chemical-Shift in Nuclear-Magnetic-Resonance in the Gas-Phase and for Adsorped Species. *Journal of Chemical Physics* (1992), vol. 97(1): pp. 417–434

[Jam93] Jameson, C. J.: Distribution and NMR Chemical-Shifts of Xenon in Zeolites. *Abstracts of Papers of the American Chemical Society* (1993), vol. 206: pp. 260–PHYS

[Jam94] Jameson, C. J.; Jameson, A. K.; Lim, H. M. and Baello, B. I.: Grand-Canonical Monte-Carlo Simulations of the Distribution and Chemical-Shifts of Xenon in the Cages of Zeolite Naa .2. Structure of the Adsorbed Fluid. *Journal of Chemical Physics* (1994), vol. 100(8): pp. 5977–5987

[Kas50] Kastler, A.: *Quelques Suggestions Concernant La Production Optique Et La Detection Optique Dune Inegalite De Population Des Niveaux De Quantification Spatiale Des Atomes - Application a Lexperience De Stern Et Gerlach Et a La Resonance Magnetique. *Journal De Physique Et Le Radium* (1950), vol. 11(6): pp. 255–265

[Kau00] Kauczor, H. U. and Kreitner, K. F.: Contrast-Enhanced MRI of the Lung. *European Journal of Radiology* (2000), vol. 34(3): pp. 196–207

[Kek10] Kekkonen, P. M.; Telkki, V. V. and Jokisaari, J.: Effect of Thermal Modification on Wood Cell Structures Observed by Pulsed-Field-Gradient Stimulated-Echo NMR. *Journal of Physical Chemistry C* (2010), vol. 114(43): pp. 18693–18697

[Ken91] Kentgens, A. P. M.; Vanboxtel, H. A.; Verweel, R. J. and Veeman, W. S.: Line-Broadening Effects for Xe-129 Absorbed in the Amorphous State of Solid Polymers. *Macromolecules* (1991), vol. 24(12): pp. 3712–3714

[Kil26] Killian, T. J.: Thermionic Phenomena Caused by Vapors of Rubidium and Potassium. *Physical Review* (1926), vol. 27(5): pp. 578–587

[Kil01] Kilian, W.: Erzeugung Von Hyperpolarisiertem ^{129}Xe-Gas Und Nachweis Mittels in Vivo NMR-Bildgebung, NMR-Spektroskopie Sowie Squid-Messtechnik. PhD thesis, Freie Universität Berlin (2001)

[Kil04] Kilian, W.; Seifert, F. and Rinneberg, H.: Dynamic NMR Spectroscopy of Hyperpolarized Xe-129 in Human Brain Analyzed by an Uptake Model. *Magnetic Resonance in Medicine* (2004), vol. 51(4): pp. 843–847

[Krj05] Krjukov, E. V.; O'Neill, J. D. and Owers-Bradley, J. R.: Brute Force Polarization of Xe-129. *Journal of Low Temperature Physics* (2005), vol. 140(5-6): pp. 397–408

[Lan98] Landfester, K.; Spiegel, S.; Born, R. and Spiess, H. W.: On Line Detection of Emulsion Polymerization by Solid State NMR Spectroscopy. *Colloid and Polymer Science* (1998), vol. 276(4): pp. 356–361

[Lan99] Landfester, K.; Bechthold, N.; Tiarks, F. and Antonietti, M.: Formulation and Stability Mechanisms of Polymerizable Miniemulsions. *Macromolecules* (1999), vol. 32(16): pp. 5222–5228

[Lan06] Landfester, K.: Synthesis of Colloidal Particles in Miniemulsions. *Annual Review of Materials Research* (2006), vol. 36: pp. 231–279

[Lan09] Landfester, K.: Miniemulsion Polymerization and the Structure of Polymer and Hybrid Nanoparticles. *Angewandte Chemie-International Edition* (2009), vol. 48(25): pp. 4488–4507

[Lan10a] Landfester, K. and Crespy, D.: Miniemulsion Polymerization as a Versatile Tool for the Synthesis of Functionalized Polymers. *Beilstein Journal of Organic Chemistry* (2010), vol. 6: pp. 1132–1148

[Lan10b] Landfester, Katharina and Weiss, Clemens: *Encapsulation by Miniemulsion Polymerization*, vol. 229 of *Advances in Polymer Science*, Springer Berlin / Heidelberg (2010), pp. 1–49

[Lar93] Larsen, R. G.; Shore, J.; Schmidt-Rohr, K.; Emsley, L.; Long, H.; Pines, A.; Janicke, M. and Chmelka, B. F.: NMR-Study of Xenon Dynamics and Energetics in Na-a Zeolite. *Chemical Physics Letters* (1993), vol. 214(2): pp. 220–226

[Lau73] Lauterbur, P. C.: Image Formation by Induced Local Interactions - Examples Employing Nuclear Magnetic-Resonance. *Nature* (1973), vol. 242(5394): pp. 190–191

[Li99] Li, H.; Eddaoudi, M.; O'Keeffe, M. and Yaghi, O. M.: Design and Synthesis of an Exceptionally Stable and Highly Porous Metal-Organic Framework. *Nature* (1999), vol. 402(6759): pp. 276–279

[Li06] Li, D. H.; Sudol, E. D. and El-Aasser, M. S.: Miniemulsion and Conventional Emulsion Copolymerization of Styrene and Butadiene: A Comparative Kinetic Study. *Journal of Applied Polymer Science* (2006), vol. 101(4): pp. 2304–2312

[Loc01] Locci, E.; Dehouck, Y.; Casu, M.; Saba, G.; Lai, A.; Luhmer, M.; Reisse, J. and Bartik, K.: Probing Proteins in Solution by Xe-129 NMR Spectroscopy. *Journal of Magnetic Resonance* (2001), vol. 150(2): pp. 167–174

[Lor09] Loring, S. H.; Butler, J. P. and Patz, S.: Science to Practice: How Do We Interpret the Transfer of Hyperpolarized ^{129}Xe from Blood into Alveolar Gas? *Radiology* (2009), vol. 252(2): pp. 319–321

[Man77] Mansfield, P.: Multi-Planar Image-Formation Using NMR Spin Echoes. *Journal of Physics C-Solid State Physics* (1977), vol. 10(3): pp. L55–L58

[Mat07] Matyjaszewski, Krzysztof; Gnanou, Yves and Leibler, Ludwik: *Macromolecular Engineering: Precise Synthesis, Materials Properties, Applications*, Macromolecular Engineering: Precise Synthesis, Materials Properties, Applications, Wiley-VCH Verlag GmbH and Co. KGaA (2007)

[Maz11] Mazzanti, Mary L.; Walvick, Ronn P.; Zhou, Xin; Sun, Yanping; Shah, Niral; Mansour, Joey; Gereige, Jessica and Albert, Mitchell S.: Distribution of Hyperpolarized Xenon in the Brain Following Sensory Stimulation: Preliminary MRI Findings. *Plos One* (2011), vol. 6(7)

[Mee08] Meersmann, T.; Cleveland, Z. I.; Pavlovskaya, G. E.; Elkins, N. D.; Stupic, K. F. and Repine, J. E.: Hyperpolarized Kr-83 MRI of Lungs. *Journal of Magnetic Resonance* (2008), vol. 195(2): pp. 232–237

[Mei90] Meijs, Gordon F. and Rizzardo, Ezio: Reactivity of Macromonomers in Free Radical Polymerization. *Journal of Macromolecular Science, Part C: Polymer Reviews* (1990), vol. 30(3-4): pp. 305–377

[Mil01] Milano, G.; Venditto, V.; Guerra, G.; Cavallo, L.; Ciambelli, P. and Sannino, D.: Shape and Volume of Cavities in Thermoplastic Molecular Sieves Based on Syndiotactic Polystyrene. *Chemistry of Materials* (2001), vol. 13(5): pp. 1506–1511

[Mil09] Milano, G. and Guerra, G.: Understanding at Molecular Level of Nanoporous and Co-Crystalline Materials Based on Syndiotactic Polystyrene. *Progress in Materials Science* (2009), vol. 54(1): pp. 68–88

[Moe11] Moeller, H. E.; Cleveland, Z. I. and Driehuys, B.: Relaxation of Hyperpolarized ^{129}Xe in a Deflating Polymer Bag. *Journal of Magnetic Resonance* (2011), vol. 212(1): pp. 109–115

[Mou04] Moudrakovski, I.; Soldatov, D. V.; Ripmeester, J. A.; Sears, D. N. and Jameson, C. J.: Xenmr Lineshapes in Channels of Peptide Molecular Crystals. *Proceedings of the National Academy of Sciences of the United States of America* (2004), vol. 101(52): pp. 17924–17929

[Mue07] Muehlbauer, F.: Polarimetrie an Hyperpolarisiertem ^{129}Xe. PhD thesis, Johannes Gutenberg University Mainz (2007)

[Mue11] Mueller, P. A.; Richards, J. R. and Congalidis, J. P.: Polymerization Reactor Modeling in Industry. *Macromolecular Reaction Engineering* (2011), vol. 5(7-8): pp. 261–277

[Mün05] Münnemann, K.: Xenon NMR with Spectroscopic, Spatial, and Temporal Resolution. PhD thesis, RWTH Aachen University (2005)

[Mün11] Münnemann, K. and Spiess, H. W.: Nuclear Magnetic Resonance the Art of Signal Enhancement. *Nature Physics* (2011), vol. 7(7): pp. 522–523

[New93] Newbury, N. R.; Barton, A. S.; Cates, G. D.; Happer, W. and Middleton, H.: Gaseous He-3 He-3 Magnetic Dipolar Spin Relaxation. *Physical Review A* (1993), vol. 48(6): pp. 4411–4420

[Nom04] Nomura, M.: Kinetics and Mechanisms of Emulsion Polymerization. *Journal of Industrial and Engineering Chemistry* (2004), vol. 10(7): pp. 1182–1216

[Pat07] Patz, S.; Hersman, F. W.; Muradian, I.; Hrovat, M. I.; Ruset, I. C.; Ketel, S.; Jacobson, F.; Topulos, G. P.; Hatabu, H. and Butler, J. P.: Hyperpolarized Xe-129 MRI: A Viable Functional Lung Imaging Modality? *European Journal of Radiology* (2007), vol. 64(3): pp. 335–344

[Paw07] Pawsey, S.; Moudrakovski, I.; Ripmeester, J.; Wang, L. Q.; Exarhos, G. J.; Rowsell, J. L. C. and Yaghi, O. M.: Hyperpolarized Xe-129 Nuclear Magnetic Resonance Studies of Isoreticular Metal-Organic Frameworks. *Journal of Physical Chemistry C* (2007), vol. 111(16): pp. 6060–6067

[Paw10] Pawsey, Shane; Kalebaila, Kennedy K.; Moudrakovski, Igor; Ripmeester, John A. and Brock, Stephanie L.: Pore Structure and Interconnectivity of Cds Aerogels and Xerogels by Hyperpolarized Xenon NMR. *The Journal of Physical Chemistry C* (2010), vol. 114(31): pp. 13187–13195

[Pen94] Penlidis, A.: Polymer Reaction-Engineering - from Reaction-Kinetics to Polymer Reactor Control. *Canadian Journal of Chemical Engineering* (1994), vol. 72(3): pp. 385–391

[Pil09] Pileio, G. and Levitt, M. H.: Theory of Long-Lived Nuclear Spin States in Solution Nuclear Magnetic Resonance. Ii. Singlet Spin Locking. *Journal of Chemical Physics* (2009), vol. 130(21)

[Pon08] Pons, M.; Blobel, J.; Fayos, R.; Garcia, J.; Marimon, O. and Perez, Y.: Low-Molecular-Weight Spies of Protein-Protein Interactions. *Comptes Rendus Chimie* (2008), vol. 11(4-5): pp. 499–505

[Pri11] Pribat, C. and Dutartre, D.: Anisotropy Effects During Non-Selective Epitaxial Growth of Si and Sige Materials. *Journal of Crystal Growth* (2011), vol. 334(1): pp. 138–145

[Pur46] Purcell, E. M.; Torrey, H. C. and Pound, R. V.: Resonance Absorption by Nuclear Magnetic Moments in a Solid. *Physical Review* (1946), vol. 69(1-2): pp. 37–38

[Rai04] Raich, H. and Blümler, P.: Design and Construction of a Dipolar Halbach Array with a Homogeneous Field from Identical Bar Magnets: NMR Mandhalas. *Concepts in Magnetic Resonance Part B-Magnetic Resonance Engineering* (2004), vol. 23B(1): pp. 16–25

[Riz05] Rizzo, P.; Albunia, A. R. and Guerra, G.: Polymorphism of Syndiotactic Polystyrene: Gamma Phase Crystallization Induced by Bulky Non-Guest Solvents. *Polymer* (2005), vol. 46(23): pp. 9549–9554

[Riz11a] Rizi, R. R.; Cereda, M.; Emami, K.; Kadlecek, S.; Xin, Y.; Mongkolwisetwara, P.; Profka, H.; Barulic, A.; Pickup, S.; Mansson, S.; Wollmer, P.; Ishii, M. and Deutschman, C. S.: Quantitative Imaging of Alveolar Recruitment with Hyperpolarized Gas MRI During Mechanical Ventilation. *Journal of Applied Physiology* (2011), vol. 110(2): pp. 499–511

[Riz11b] Rizzo, Paola and Albunia, Alexandra R.: Syndiotactic Polystyrene Films: Orientation and Structural Changes Upon Biaxial Drawing. *Macromolecular Chemistry and Physics* (2011), vol. 212(13): pp. 1419–1426

[Ron05] Rong, Y.; Chen, H. Z.; Wu, G. and Wang, M.: Preparation and Characterization of Titanium Dioxide Nanoparticle/Polystyrene Composites Via Radical Polymerization. *Materials Chemistry and Physics* (2005), vol. 91(2-3): pp. 370–374

[Roo07] Rooney, William D.; Johnson, Glyn; Li, Xin; Cohen, Eric R.; Kim, Seong-Gi; Ugurbil, Kamil and Springer, Charles S.: Magnetic Field and Tissue Dependencies of Human Brain Longitudinal 1h2o Relaxation in Vivo. *Magnetic Resonance in Medicine* (2007), vol. 57(2): pp. 308–318

[Ros03] Rosi, N. L.; Eckert, J.; Eddaoudi, M.; Vodak, D. T.; Kim, J.; O'Keeffe, M. and Yaghi, O. M.: Hydrogen Storage in Microporous Metal-Organic Frameworks. *Science* (2003), vol. 300(5622): pp. 1127–1129

[Ros10] Ross, B. D.; Bhattacharya, P.; Wagner, S.; Tran, T. and Sailasuta, N.: Hyperpolarized Mr Imaging: Neurologic Applications of Hyperpolarized Metabolism. *American Journal of Neuroradiology* (2010), vol. 31(1): pp. 24–33

[Row10] Rowland, I. J.; Peterson, E. T.; Gordon, J. W. and Fain, S. B.: Hyperpolarized (13)Carbon Mr. *Current Pharmaceutical Biotechnology* (2010), vol. 11(6): pp. 709–719

[Rus05] Ruset, Iulian C.: Hyperpolarized ^{129}Xe Production and Applications. PhD thesis, University of New Hampshire (2005)

[Rus06] Ruset, I. C.; Ketel, S. and Hersman, F. W.: Optical Pumping System Design for Large Production of Hyperpolarized Xe-129. *Physical Review Letters* (2006), vol. 96(5)

[Rut99] Ruth, U.; Hof, T.; Schmidt, J.; Fick, D. and Jansch, H. J.: Production of Nitrogen-Free, Hyperpolarized Xe-129 Gas. *Applied Physics B-Lasers and Optics* (1999), vol. 68(1): pp. 93–97

[Saa95] Saam, B.; Happer, W. and Middleton, H.: Nuclear-Relaxation of He-3 in the Presence of O-2. *Physical Review A* (1995), vol. 52(1): pp. 862–865

[Sau96] Saunders, M.; JimenezVazquez, H. A. and Khong, A.: NMR of He-3 Dissolved in Organic Solids. *Journal of Physical Chemistry* (1996), vol. 100(39): pp. 15968–15971

[Sch65] Schearer, L. D. and Walters, G. K.: Nuclear Spin-Lattice Relaxation in Presence of Magnetic-Field Gradients. *Physical Review* (1965), vol. 139(5A): p. 1398

[Sch05] Schork, F. J.; Luo, Y. W.; Smulders, W.; Russum, J. P.; Butte, A. and Fontenot, K.: Miniemulsion Polymerization. *Polymer Particles* (2005), vol. 175: pp. 129–255

[Sch06a] Schmiedeskamp, J.; Elmers, H. J.; Heil, W.; Otten, E. W.; Sobolev, Y.; Kilian, W.; Rinneberg, H.; Sander-Thommes, T.; Seifert, F. and Zimmer, J.: Relaxation of Spin Polarized He-3 by Magnetized Ferromagnetic Contaminants Part Iii. *European Physical Journal D* (2006), vol. 38(3): pp. 445–454

[Sch06b] Schmiedeskamp, J.; Heil, W.; Otten, E. W.; Kremer, R. K.; Simon, A. and Zimmer, J.: Paramagnetic Relaxation of Spin Polarized He-3 at Bare Glass Surfaces Part I. *European Physical Journal D* (2006), vol. 38(3): pp. 427–438

[Sch09] Schroder, L.; Meldrum, T.; Smith, M.; Schilling, F.; Denger, P.; Zapf, S.; Wemmer, D. and Pines, A.: Xenon Biosensors for Multi-Purpose Molecular Imaging. *World Congress on Medical Physics and Biomedical Engineering, Vol 25, Pt 13* (2009), vol. 25(13): pp. 176–179

[SH99] Springuel-Huet, M. A.; Bonardet, J. L.; Gedeon, A. and Fraissard, J.: Xe-129 NMR Overview of Xenon Physisorbed in Porous Solids. *Magnetic Resonance in Chemistry* (1999), vol. 37: pp. S1–S13

[Sha12] Shaghaghi, M.; Yousefi, A. and Pishvaei, M.: Synthesis of Artificial Opals with Core-Shell Morphology Via Emulsion Polymerization Technique. *E-Polymers* (2012)

[Siv04] Sivakumar, M.; Suzuki, T.; Yamamoto, Y.; Mahesh, K. P. O.; Yoshimizu, H. and Tsujita, Y.: Structure and Properties of the Mesophase of Syndiotactic Polystyrene Membrane Vii. Isothermal Sorption Behavior of Xenon. *Journal of Membrane Science* (2004), vol. 238(1-2): pp. 75–81

[Smi48] Smith, W. V. and Ewart, R. H.: Kinetics of Emulsion Polymerization. *Journal of Chemical Physics* (1948), vol. 16(6): pp. 592–599

[Sol05] Solans, C.; Izquierdo, P.; Nolla, J.; Azemar, N. and Garcia-Celma, M. J.: Nano-Emulsions. *Current Opinion in Colloid and Interface Science* (2005), vol. 10(3-4): pp. 102–110

[Soz00] Sozzani, P.; Comotti, A.; Simonutti, R.; Meersmann, T.; Logan, J. W. and Pines, A.: A Porous Crystalline Molecular Solid Explored by

Hyperpolarized Xenon. *Angewandte Chemie-International Edition* (2000), vol. 39(15): pp. 2695–2698

[Soz06] Sozzani, P.; Simonutti, R.; Bracco, S.; Comotti, A. and Mauri, M.: Continuous Flow Hyperpolarized Xe-129 NMR for Studying Porous Polymers and Blends. *Chemistry of Materials* (2006), vol. 18(19): pp. 4651–4657

[Soz07] Sozzani, P.; Comotti, A.; Bracco, S.; Ferretti, L.; Mauri, M. and Simonutti, R.: A Single-Crystal Imprints Macroscopic Orientation on Xenon Atoms. *Chemical Communications* (2007), (4): pp. 350–352

[Ste65] Stejskal, E. O. and Tanner, J. E.: Spin Diffusion Measurements: Spin Echoes in the Presence of a Time-Dependent Field Gradient. *Journal of Chemical Physics* (1965), vol. 42(1): p. 288

[Suz86] Suzuki, T.; Masuda, S.; Matsui, Y. and Nakanishi, Y.: Phase-Diagram of the Rb-O System and Disproportionation of Rubidium Suboxide. *Journal of Nuclear Materials* (1986), vol. 137(3): pp. 250–255

[Tar10a] Tarallo, Oreste; Petraccone, Vittorio; R. Albunia, Alexandra; Daniel, Christophe and Guerra, Gaetano: Monoclinic and Triclinic Delta-Clathrates of Syndiotactic Polystyrene. *Macromolecules* (2010), vol. 43(20): pp. 8549–8558

[Tar10b] Taratula, O. and Dmochowski, I. J.: Functionalized ^{129}Xe Contrast Agents for Magnetic Resonance Imaging. *Current Opinion in Chemical Biology* (2010), vol. 14(1): pp. 97–104

[Thi07] Thickett, S. C. and Gilbert, R. G.: Emulsion Polymerization: State of the Art in Kinetics and Mechanisms. *Polymer* (2007), vol. 48(24): pp. 6965–6991

[Tor63] Torrey, H. C.: Chemical Shift and Relaxation of Xe-129 in Xenon Gas. *Physical Review* (1963), vol. 130(6): p. 2306

[Tor09] Torres, F. Javier; Civalleri, Bartolomeo; Meyer, Alessio; Musto, Pellegrino; Albunia, Alexandra R.; Rizzo, Paola and Guerra, Gaetano: Normal Vibrational Analysis of the Syndiotactic Polystyrene S(2/1)2 Helix. *The Journal of Physical Chemistry B* (2009), vol. 113(15): pp. 5059–5071

[Uti11] Utiu, L.; Filipoi, C.; Demco, D. E.; Zhu, X. M.; Vinokur, R.; Conradi, O.; Graichen, A.; Blümich, B. and Moeller, M.: Free Volume of Poly(Perfluorosulfonic Acid)/SiO_2 Composite Proton Exchange Membranes by ^{129}Xe NMR. *Chemical Physics Letters* (2011), vol. 506(1-3): pp. 71–75

[Wak04] Wakai, A.; Nakamura, K.; Kershaw, J. and Kanno, I.: In Vivo Mr Spectroscopy of Hyperpolarized Xe-129 in Rat Brain. *Quantitation in Biomedical Imaging with PET and MRI* (2004), (1265): pp. 139–143

[Wak08] Wakayama, T.; Kitamoto, M.; Ueyama, T.; Imai, H.; Narazaki, M.; Kimura, A. and Fujiwara, H.: Hyperpolarized Xe-129 MRI of the Mouse Lung at a Low Xenon Concentration Using a Continuous Flow-Type Hyperpolarizing System. *Journal of Magnetic Resonance Imaging* (2008), vol. 27(4): pp. 777–784

[Wal97] Walker, T. G. and Happer, W.: Spin-Exchange Optical Pumping of Noble-Gas Nuclei. *Reviews of Modern Physics* (1997), vol. 69(2): pp. 629–642

[Wal98] Walter, D. K.; Happer, W. and Walker, T. G.: Estimates of the Relative Magnitudes of the Isotropic and Anisotropic Magnetic-Dipole Hyperfine Interactions in Alkali-Metal-Noble-Gas Systems. *Physical Review A* (1998), vol. 58(5): pp. 3642–3653

[War09] Warren, W. S.; Jenista, E.; Branca, R. T. and Chen, X.: Increasing Hyperpolarized Spin Lifetimes through True Singlet Eigenstates. *Science* (2009), vol. 323(5922): pp. 1711–1714

[Wei09] Weiss, C. K.; Aschenbrenner, E. M. and Landfester, K.: Enzymatic Esterification in Aqueous Miniemulsions. *Chemistry-a European Journal* (2009), vol. 15(10): pp. 2434–2444

[Wei11] Weiss, Clemens and Landfester, Katharina: *Miniemulsion Polymerization as a Means to Encapsulate Organic and Inorganic Materials*, vol. 233 of *Advances in Polymer Science*, Springer Berlin / Heidelberg (2011), pp. 185–236

[Zae07] Zaenker, P.-P.: NMR Spectroscopy and Imaging of Hyperpolarized Gases: Fundamental Aspects and Applications. PhD thesis, Johannes Gutenberg University Mainz (2007)

[Zha08] Zhang, W. P.; Liu, Y.; Liu, Z. C.; Xu, S. T.; Wang, Y. D.; Xie, Z. K.; Han, X. W. and Bao, X. H.: Direct Observation of the Mesopores in Zsm-5 Zeolites with Hierarchical Porous Structures by Laser-Hyperpolarized Xe-129 NMR. *Journal of Physical Chemistry C* (2008), vol. 112(39): pp. 15375–15381

[Zhe11] Zheng, Wangzhi; Cleveland, Z. I.; Moumlller, H. E. and Driehuys, B.: Gradient-Induced Longitudinal Relaxation of Hyperpolarized Noble Gases in the Fringe Fields of Superconducting Magnets Used for Magnetic Resonance. *Journal of Magnetic Resonance* (2011), vol. 208(2): pp. 284–290290

[Zho11] Zhou, X.; Sun, Y. P.; Mazzanti, M.; Henninger, N.; Mansour, J.; Fisher, M. and Albert, M.: MRI of Stroke Using Hyperpolarized ^{129}Xe. *NMR in Biomedicine* (2011), vol. 24(2): pp. 170–175

List of Figures

List of Tables

List of Abbreviations

SEOP spin-exchange optical pumping
MEOP metastability exchange optical pumping
NMR nuclear magnetic resonance
DNP dynamic nuclear polarization
PHIP parahydrogen induced polarization
OP optical pumping
PEEK polyether ether ketone
PUR polyurethane
PE polypropylene
SDS sodium dodecyl sulfate
PCCS photon cross correlation spectroscopy
SNR signal-to-noise ratio
ADC apparent diffusion coefficent
FOV field of view
EPR electronic paramagnetic resonance
CSA chemical shift anisotropy
SR spin rotation
RF radio frequency
TMS tetramethylsilane
MRI magnetic resonance imaging
SEC size-exclusion chromatography
PCCS photon cross correlation spectroscopy

Acknowledgements

Curriculum Vitae

Publications

Online Monitoring of Styrene Polymerization in Miniemulsion by Hyperpolarized ^{129}Xenon NMR Spectroscopy
M. Duewel, N. Vogel, C. K. Weiss, K. Landfester, H.-W. Spiess, K. Münnemann
Macromolecules **2012**, *45* (4), 1839-1846

Oriented Nanoporous Phases of Syndiotactic Polystyrene Films Probed by ^{129}Xe NMR Spectroscopy
M. Duewel, A. R. Albunia, R. Graf, H.-W. Spiess, K. Münnemann
in preparation